UNIVERSITÀ DEGLI STUDI DI TRIESTE

XXXII CICLO DEL DOTTORATO DI RICERCA IN NANOTECNOLOGIE

"Design and characterization of nanomaterials for monitoring their biological reactivity"

Settore scientifico-disciplinare: CHIM/03

Dottoranda
Ilaria Zanoni

Coordinatore
Prof.ssa Lucia Pasquato

Supervisore Di Tesi
Prof.ssa Francesca Larese Filon

Co-Supervisore Di Tesi
Dott.ssa Anna Luisa Costa

ANNO ACCADEMICO 2018/2019

Table of Contents

Dedicated to my Grandma

Abstract

The goal of this Ph.D. thesis, was that to support nanomaterials risk assessment, focusing on the characterization and control of physicochemical properties and behaviors, causing potentially hazardous mechanisms against human and environment. Throughout six different nanoparticles here organized into five case studies, the experimental design was set up for measuring nanomaterials intrinsic (composition, dimension and morphology), system-dependent (aggregation and dissolution in media) and fate related properties. Both reference and commercial nanomaterials were selected as representative of a wide class of components maximizing the overall impact of the research. In a "read-across" perspective, such nanoparticles were selected as representative of three different grouping classes: soluble (Ag, CuO and ZnO), passive (SiO_2) and active (CeO_2 and TiO_2).

The case studies were faced following a step by step characterization at increasing complexity. Firstly, we collected information on the intrinsic properties (size, shape, superficial functionalization), that outline the nanoparticles nature, then we dispersed the nanoparticles in relevant (eco)tox media, measuring the system-dependent properties derived from the nanoparticles / medium interaction and finally, moving toward the human exposure routes, we evaluated the *in-vitro ex-vivo* translocation through dermal or oral mucosa membranes with Franz cell tests.

In particular, the third chapter was focused on *in-vitro ex-vivo* tests. Herein, we outlined the ability of Ir complexes to mark SiO_2 nanoparticles, without changing the properties of both phases. In this way, we followed the nanoparticles fate in different matrix and through human skin, showing a negligible trans-dermal penetration. Still using Franz cell test, CuO nanoparticles were demonstrated to penetrate only abraded human skin, being safe for intact one. While in oral mucosa exposure study, the use in *in-vitro* test of baby porcine oral mucosa showed a higher penetration of Ag nanoparticles in young individuals than in adults, highlighting the possibility of trans-oral passage also in children once exposed as well.

Whilst, in the fourth chapter, the case studies were focused on ZnO, CeO_2 and TiO_2 nanoparticles and presented a deep physiochemical characterization of intrinsic and extrinsic properties in environmental media, as sea and fresh water. This provided information related to the distribution along the water column and the fate of these nanoparticles in acellular conditions.

As far as fate in human models are concerned, we believe that data collected will contribute to dosimetry adjustment of dermal and oral mucosa exposure-dose-response studies, in order to derive more relevant reference doses (DNEL, ADI, …). In addition, the knowledge of nanomaterials fate across dermal barriers will provide information on human exposure potential and mechanism. Moreover, fate in environmental model, even less investigated through the thesis, provided physicochemical data that can be used to improve eco-tox dose-response models and derive more accurate reference values (PNEC) for scientific and regulatory purposes.

Key words: nanosafety, human exposure, skin, oral mucosa, ecotox model.

List of abbreviations

Acceptable daily intake (ADI)

Add-on value (AO%)

Adverse Outcome Pathways (AOPs)

Agency for Toxic Substances and Disease Registry (ATSDR)

American Conference of Governmental Industrial Hygienists (ACGIH)

Benchmark dose (BMD)

Cerium dioxide nanoparticles (CeO_2 NPs)

Chemical safety assessment (CSA)

Compound annual growth rate (CAGR)

Copper oxide nanoparticles (CuO NPs)

Derived no-effect level (DNEL)

Dynamic light scattering (DLS)

Electrophoretic light scattering (ELS)

Energy Dispersive X-ray Analysis (EDX)

Engineered nanomaterials (ENMs)

Environmental Protection Agency (EPA)

European Chemicals Agency (ECHA)

Field emission-scanning electron microscopy (FE-SEM)

Fourier-transform infrared - Attenuated total reflection spectroscopy (FTIR-ATR)

Half maximal inhibitory concentration (IC_{50})

Hydrodynamic diameter (d_{DLS})

Inductively coupled plasma - mass spectroscopy (ICP-MS)

Inductively coupled plasma - optical emission spectrometry (ICP-OES)

Integrated Approaches to Testing and Assessment (IATA)

Isoelectric point (IEP)

Joint Research Centre (JRC)

Kinetic energy discrimination (KED)

Life-cycle assessment (LCA)

Ligand centred (LC)

Limit of detection (LOD)

Lower Observed Adverse Effect Level (LOAEL)

Mechanochemical processing (MCP)

Median effective concentrations (EC_{50})

Metal-to-ligand charge transfer (MLCT)

Minimum inhibitory concentration (MIC)

Mutual Acceptance of Data in the Assessment of Chemicals (MAD)

Nano-enabled products (NEPs)

Nanomaterials (NMs)

Nanoparticles (NPs)

Nano Safety Cluster (NSC)

No Observed Adverse Effect Level (NOAEL)

Occupational exposure limits (OELs)

Organisation for Economic Co-operation and Development (OECD)

Phosphate-buffered saline (PBS)

Polydispersity index (PdI)

Polyvinylpirrolidone (PVP)

Predicted no-effect concentrations (PNEC)

Quantitative Structure-Activity Relationship (QSAR)

Reference dose (RfD)

Registration, Evaluation, Authorization and Restriction of Chemicals (REACH)

Reactive oxygen species (ROS)

Reference materials (RMs)

Relative standard deviation (RSD %)

Risk characterization ratios (RCRs)

Room temperature (RT)

Silica dioxide nanoparticles (SiO_2 NPs)

Silver nanoparticles (Ag NPs)

Single Particle – Inductively Coupled Plasma – Mass Spectrometry (SP-ICP-MS)

Scanning transmission electron microscopy (STEM)

Standard deviation (SD)

Thermo-gravimetric (TG)

Titanium dioxide nanoparticles (TiO_2 NPs)

Transmission Electron Microscopy (TEM)

Ultra-centrifugal filter (UCF)

Ultrafiltration (UF)

United State dollar (USD)

Zeta potential (ZP - ζ-pot_{ELS})

Zinc oxide nanoparticles (ZnO NPs)

1. Introduction

Since the 20th century, when "nanotechnology" was presented by Nobel prize Richard P. Feynman during his famous lecture "There's Plenty of Room at the Bottom"[1], nanotechnology became a breakthrough research field with promising revolutionary developments in every day applications[2].

Nowadays, nanotechnology and nanomaterials are getting more available and present in different products on the market, due to the advantages obtained from their use and properties. Nanomaterials (NMs) and nano-enabled products (NEPs) cover an active area of research and related techno-economic sectors, with full expansion in many application domains and fields. NMs and NEPs have grown importance in technological advancements due to their tunable physicochemical properties. In nano-dimension world, physiochemical matter characteristics change - such as melting point, wettability, electrical and thermal conductivity, antibacterial power, catalytic activity, light interaction with matter - resulting in enhanced performance over their bulk counterparts and provides new properties to materials, improving their use in new fields[3]. Therefore, NMs and NEPs find their use in various applications such as nanomedicine, for drug delivery, imaging, cancer diagnosis and therapy[4], chemical sensors and biosensors[5], food[6], aerospace[7], environmental remediation[8], for energy and catalysis[9,10], and in every day used as clothings[11].

Due to these interesting new properties, over 1'800 know products already on the market contained engineered NMs and this number is expected to grow. The European NMs market generated turnover of more than United State dollar (USD) 2.5 billion in 2015 and is expected to reach USD 9.1 billion by 2022, with a compound annual growth rate (CAGR) of 20.0% during 2016-2022. In the market metal and non-metal oxide-based nanoparticles (NPs) are the most widely applied NMs in the industrial production with a CAGR of 20.7% from 2016 to 2022, where titanium dioxide, silver, and silicon dioxide NMs cover alone above 25% of the market[12,13]. Exact global annual production quantities are unknown, but it is estimated at up to 10'000 tones just only for titanium dioxide based NMs[14,15].

In principle, NMs are described as materials with length of 1–100 nm in at least one dimension, where a nanometer (nm) is an International System of Units (Système international d'unités, SI) unit that represents 10^{-9} meter in length. Nanoscale materials can include nanoparticles (NPs) (3-dimension nano), nanotubes (2-dimension nano) and nanofilms (1-dimension nano). The European Community already provided in the Recommendation

2011/696/EU the definition of “nanomaterial” as *a natural, incidental or manufactured material containing particles, in an unbound state or as an aggregate or as an agglomerate and where, for 50 % or more of the particles in the number size distribution, one or more external dimensions is in the size range 1 nm - 100 nm*[16]. However, the regulatory definition is still being debated[17].

Today the definition itself was inspected, there are several documents of EU legislation and technical guidance supporting implementation of legislation, with specific references to NMs[18–20]. Since EU defined the metric dimension, it is necessary to understand, evaluate and monitor the functioning of these new nanotechnology and NMs when in contact with possible biological target during their life-cycle[21–23]. New NMs allow on the one hand new products and solutions, but also raise concerns due to their new specific properties that change in the nano-dimension as well interactions and effects on biological matter[22].

NMs are not intrinsically hazardous per se but specific considerations have to take into account in their risk assessment associated with human and environment, the two main targets considered[16]. In front of the huge number of NMs / NEPs available on the market, scientific community and EU regulatory frameworks have to consider the global NMs production and thus which NMs can get in touch with human or release in the environment during their life-cycle.

In the regulatory frameworks, the predominant regulation institution is the Registration, Evaluation, Authorization and Restriction of Chemicals (REACH) that control and regulate the production and use of any substance[24,25]. In the specific case also NMs are regulated, as any chemical, by REACH, being covered by the definition of "substance" stated in the regulation[26]. For each substance, including in its nano-dimension, REACH requires a dossier of information supplied by industry on the toxicology, eco-toxicology and physiochemical properties. The European Chemicals Agency (ECHA) has developed REACH guidance documents providing specific recommendations for the characterization and hazard assessment of NMs. Modifications of REACH to specifically addressing NMs are currently under review by the European Commission and are being discussed with member states[27]. Actually, the Organisation for Economic Co-operation and Development (OECD), in agreement with the Mutual Acceptance of Data in the Assessment of Chemicals (MAD), have developed guidance and guidelines for testing nanomaterial safety[28,29].

Therefore, the research focused on the safe use of nanotechnology is getting necessary more and more challenging. In the past years, community research, in Europe joint under Nano

Safety Cluster (NSC)[30], has done many attempt to investigate possible adverse effects and toxicity of NMs and NEPs from both human and environmental points of view[31–34]. Meantime, the European Commission legislation about NMs and NEPs is going to be implemented, but to have an almost complete risk assessment, the NMs / NEPs risk assessment has to be evaluated in a life-cycle prospective (life-cycle assessment – LCA), using a cradle-to-grave approach (Figure 1.1)[26,35]. The interaction between NMs and human or environment has to be investigated in each life-cycle step, identifying exposure scenarios, exposure routes and nano-bio interaction mechanisms, at the final aim to improve confidence on nanotechnology, avoid/control any potential detrimental effects, outline the regulatory framework that ensure a safe use of NMs / NEPs.

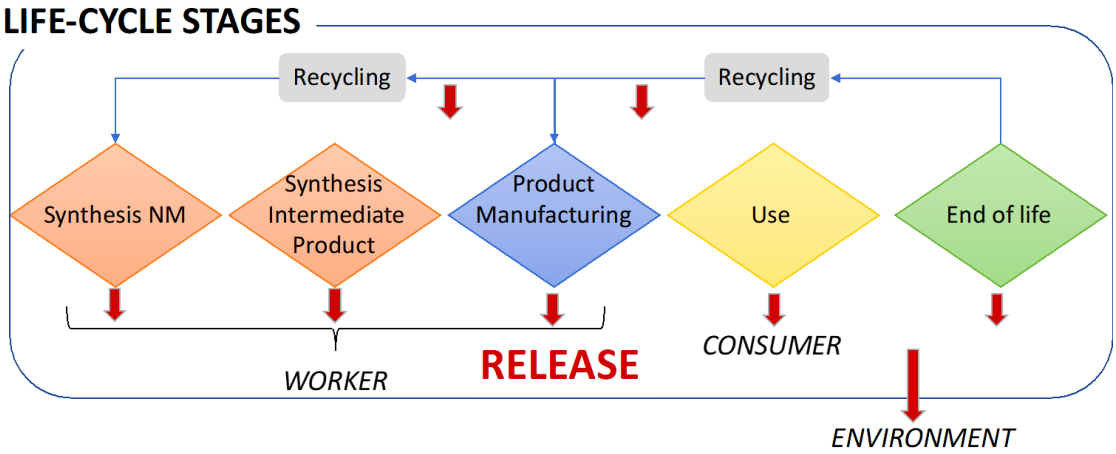

Figure 1.1: "Cradle-to-grave" life-cycle stages of a generic NM. Red rows indicate potential release impacting on worker, consumer and generically environment.

1.1 Human target

At the present, there is on the market a huge number of products that present NMs free or embedded in NEPs (coatings, fillers of bulk matrices), and that are used in common applications. Nanotechnology, as a cross-cutting technology, involves many applications, including specific human health care[36–39], as a consequence, NMs can get in touch with human through different exposure routes. The potential for a NMs to have toxic effects can be related to its physiochemical properties, such as size, shape, surface area, charge and reactivity, and solubility. Therefore, based on their physiochemical properties and final application in which they are used, NMs can be ingested, inhaled (if airborne), and adsorbed or injected through the skin, once in voluntary or accidental contact with the human target (Figure 1.2).

Ingestion can occur for deliberate uptake[40], with unintentional hand to mouth transfer or larger particles that deposit in the mouth, nose, or throat which can be swallowed. **Inhalation** happens basically with NMs at their powdered state and is the exposure route of

greatest concern, especially in occupational setting. Through inhalation, NMs can enter the blood stream and translocate to other organs[22,41,42]. Finally **skin adsorption** is mainly derived by skin healthy and integrity, and NMs chemistry composition and physical properties, such respectively dissolution ability and size dimension, possibly passing through skin and causing translocate to other organs as well[43,44].

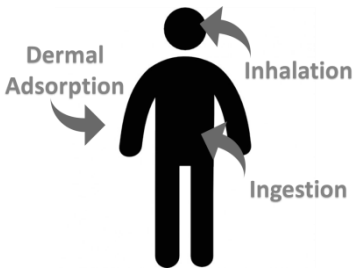

Figure 1.2: Scheme of possible human exposure routes: inhalation (lungs exposure), ingestion (from mouth to gastro intestinal track exposure), and dermal adsorption (absorbed through skin).

Once NMs are inside the human body, they may affect cells, interacting with the cell surface or entering the cell itself. Different mechanisms have been identified and a cascade of events described as part of Adverse Outcome Pathways (AOPs) that lead to final effects[45]. AOPs play a role in the risk assessment development and, as conceptual models, can describe the initial NMs interaction with the biological system through a series of measurable key events that lead to a specific adverse outcome. Some interactions are driven by intrinsic NMs characteristic and someone else by the physiological fluids, where NMs are dispersed. For instance, NMs can be coated by proteins - presents in the physiological fluid - and form a “corona” around their surface, that alter the common structure of proteins inducing phenomena such as phase transformations, restructuring and change in dissolution behaviour at the NMs surface[46]. NMs can interact with proteins, but also membranes, cells, DNA and organelles, establishing a series of NMs / biological interfaces that depend on colloidal forces (superficial charge, size, shape, …) as well as dynamic bio-physicochemical interactions. At the same time nano-bio interactions can cause an increase in the cell oxidative stress, generating an excessive levels of reactive oxygen species (ROS) inside the body and possibly causing adverse effects, from inflammation till the cell damage and death[47]. Media interactions with NMs could also induce NMs superficial modification, such as ion leaching, that interact directly with cell membrane. Finally, NMs could endocytosed entirely inside the cell and act as “Trojan horse”, so carry and release other, toxic, chemicals that are attached to its surface into cells[46]. All these contributes and more can occur,

when NMs potentially penetrate in to body and get in touch with cells possibly having some adverse effects.

To predict the final behavior, through different exposure routes and AOPs, an accurate physiochemical characterization, providing info about NMs size distribution, superficial charge, ability to release ions and oxidative potential in the human simulant medium, is requested[48]. Then this information is used in *in-vitro* and *in-vivo* extrapolation to obtain descriptors useful for regulation of NMs use in a specific exposure scenario.

1.2 Environmental target

Drawing exposure scenarios and routes in environment it is more difficult than for human. The environmental compartments that can be affected by NMs are fresh water (lakes, rivers), marine (sea, oceans) and soils ecosystems. Knowing exactly how, when and where NMs are released, transported and transformed within environmental compartments is challenging, because the applications range is wider and there are many potential pathways for release[49]. NMs may be released into the environment, intentionally or unintentionally[50,51], at any stage in their life-cycle (production, in-use stages, end-life as waste, …)[52], as shown in Figure 1.3.

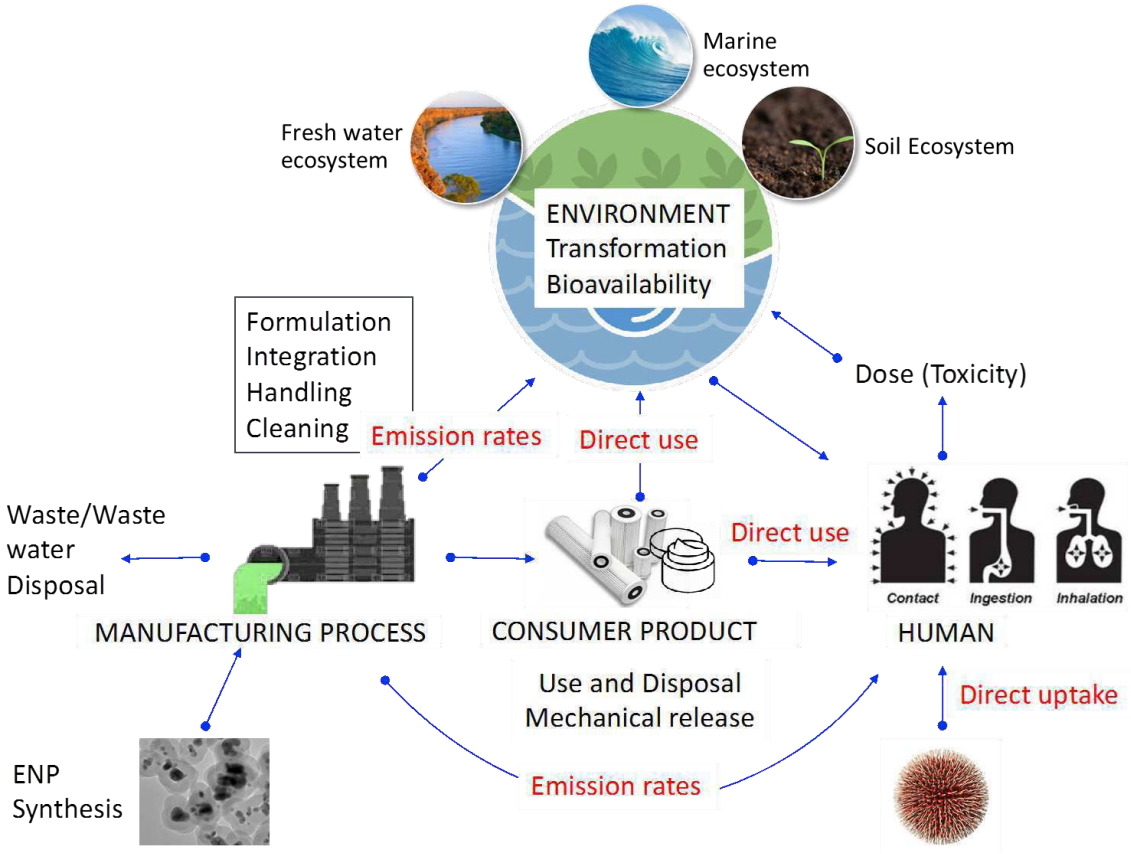

Figure 1.3: Scheme of possible environmental exposure routes.

In particular, when NMs enter in water compartments, even fresh or sea water, they tend to aggregate forming larger particles and settling in the sediment layer changing form (size, shape, dissolution ability) and their concentration along the water column[53,54]. So far, the effects of NMs on aquatic life, in most studies on fresh water and marine species, produce mainly a reduction of growth, reproduction, locomotion, breathing and feeding. In particular, NMs tend to accumulate in species at the bottom of the food chain, such as microalgae. As result, NMs could be transferred and accumulated into the food chain, reaching big hunters and human[55,56]. Nevertheless, NMs can enter also in soil ecosystems via pathways such as the application of sewage sludge, fertilizers and pesticides. As in fresh water and marine exposure, NMs can be absorbed and accumulate in plants and food, and again have implications in the food chain, as for animals as for human[57–60].

1.3 Risk characterization

Exposure-Dose-Response relationships is required to define a risk as a function of hazard and relevant exposure. A deep knowledge on Exposure-Dose-Response relationships is required to define the risk associated to NMs. The dose, amount of material associated to adverse effect, is a result of exposure before and after reaching the biological target and being up-taken (Figure 1.4).

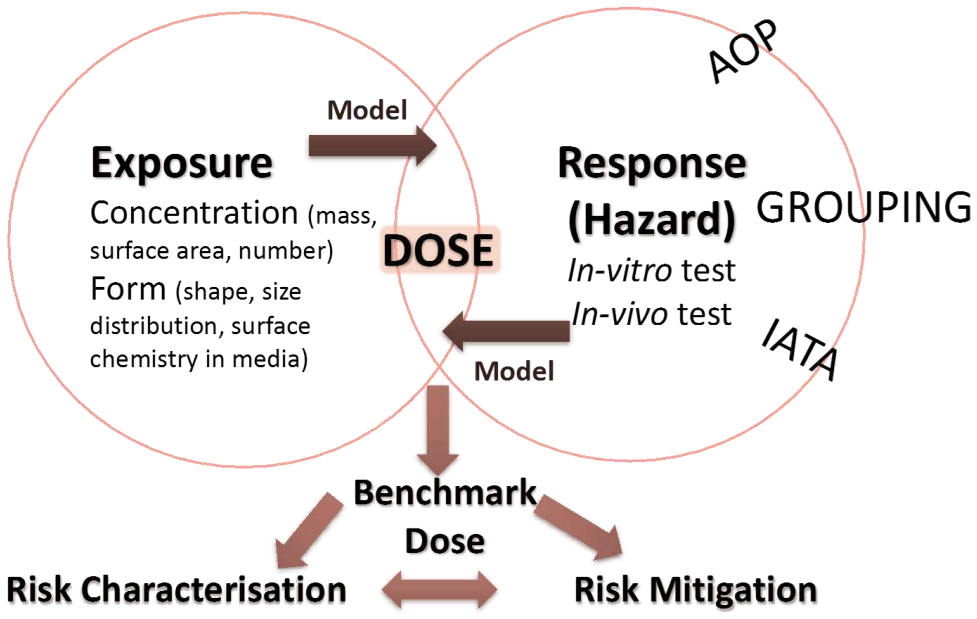

Figure 1.4: Risk characterization inputs and outputs.

Once extrapolated the exposure-dose-response relationship from *in-vitro* to *in-vivo* and to humans or environment scenario, it is possible to derive a benchmark dose (BMD). The BMD

is a dose or concentration that produces a predetermined change in the response rate of an adverse effect. This predetermined change in response is called the benchmark response (BMR). Normally, the default BMR is 5% or 10% change in the response rate of an adverse effect relative to the response of control group depending on whether response data is continuous or quantal (dichotomous).

The BMD can be used to derive for example some health guidance values such as for human: reference dose (RfD), derived no-effect level (DNEL), acceptable daily intake (ADI), occupational exposure limits (OELs), or for environment: predicted no-effect concentrations (PNEC)[61–65]. When suitable values of DNEL, OELs or PNEC, are available, risk characterization ratios (RCRs) can be derived in order to decide if the risks are under control for each environmental compartment and for each human exposure scenario known[66,67]. The RCR compares the exposure level with health guidance values, in order to decide if risks are adequately controlled for each environmental compartment and for each human population known to be or likely to be exposed (REACH Annex I, 6.4):

$$\text{RCR human health} = \frac{\text{Real Dose}}{\text{DNEL}} \qquad \text{RCR environment} = \frac{\text{PEC}}{\text{PNEC}}$$

Often dosimetric adjustments are used to convert the doses experimentally administered to animals or cells into effective doses or lifetime continuous human-equivalent doses[68], in order to improve the dose-response assessment model and derive more sound reference doses. Within the European Parliament and Council Regulation (EC) N° 1907/2006 on the REACH, risk assessment is conducted under the overall framework of the chemical safety assessment (CSA) process, by which a registrant shall identify and describe the conditions under which the manufacturing and use of a substance is considered to be safe during each life-cycle step[24].

The general obligations in REACH is applied for NMs, as for any other substance, and required a risk assessment, which should be performed as part of the CSA process using pertinent information. Hazard evaluation, made by *in-vitro* and *in-vivo* tests, is mandatory to quantify the effects produced on biological targets and investigating toxicity mechanisms, and new hazard assessment strategies (approaches, models) - such as AOPs[45], Integrated Approaches to Testing and Assessment (IATA)[69,70] and GROPUPING[32,71–74] - are becoming more and more recommended, in response to the need to reduce time, cost and animal use for testing[75,76]. Moreover, the exposure characterization, that provides information about NMs release, concentration (express as mass, surface area, number, …) and form (as shape, size

distribution, surface chemistry, …) is a priority of any risk assessment and mitigation strategy. In real exposure conditions, a variety of parameters, such as pH, salinity, the presence of co-exposed molecules, can change the physicochemical properties of NMs and so their potential toxicity[12,77,78]. One of the main research challenges is to assess how NMs form and behavior transforms throughout their life-cycle, in dependence on exposure conditions.

If the risks are not under control, the CSA has to be refined, either by obtaining more data on the properties of the substance, making more precise exposure estimations or changing the conditions of manufacturing or in-use, developing and applying a risk mitigation strategy to contain and reduce the hazard.

In conclusion, for a comprehensive NMs risk assessment, deep NMs characterization is needed to identify the presence or absence of hazardous properties, likelihood of exposure in a specific compartment (*i.e.* workplace, in-use stages, freshwater ecosystem, marine water ecosystem, soils ecosystem, …), and dose-response data (*i.e.* RfD, DNEL, OELs, PNEC..). Major investments have been done so far on the characterization of the NMs toxicological profile, adding data on relevant human health endpoints (*i.e.* acute toxicity, irritation and corrosivity, sensitization, repeated dose toxicity, mutagenicity, carcinogenicity, and reproductive toxicity), as well as data with respect to the NPs fate in the body (*i.e.* toxicokinetics, absorption, distribution, metabolism, and excretion)[79]. However there are no specific DNEL, PNEC and OELs values for all NMs[61–65]. To fill this lack of information, the European Commission seeks advice from independent scientific committees on the assessment of NMs, in order to support proposed actions to adopt new or revised OELs under Directive 2004/37/EC and Directive 98/24/EC[80,81].

In front of the EU Scientific and Advisory Committees and independent risk assessors' knowledge and opinions, current risk assessment methods are applicable, but some aspects are still uncompleted due to the current lack of standardized approaches for determining the hazards and levels of exposure to the human health and the environment. Even if the majority of standard endpoints used in regulatory hazard assessment remain appropriate for NMs in the context of supporting data for toxicological and environmental risk assessment specific considerations are needed due to the nano-dimension of NMs. However, changes on sample preparation and dosimetry have been foreseen for most of the tests[82].

1.4 Importance of physiochemical characterization in safety assessments

In the NMs safety assessment framework and in a progressive reduction of animal tests, the implementation of deep physiochemical characterizations can be exploited in the development of different approaches to reach easier and faster these two aims. A physiochemical characterization can be applied in computational modelling to derive reference values – such as dose-response data (*i.e.* PNEC, DNEL, OELs, ...). In NMs grouping, the physiochemical characterization can be selected as discriminator in the grouping parameters. In fact, the grouping strategy is based on NMs physiochemical properties - intrinsic properties - and possible interactions with biological targets classification. Thus grouping enables a "read-across" approach, that allows data gaps on potential hazards on a specific NM to be filled using information about another NM in the same group and that has been tested[72–74]. The challenge of this approach is to generate enough data about a specific NM - physiochemical properties, toxicology, … - reliably also for the other NMs of the same group[83]. The same consideration has to be done in the identification of biological adverse effects, where the physiological characterization can provide strong tools to improve it. Finally, the physiological characterization is considered the first step in both AOPs formulation and in safe-by-design approach[45,84]. In particular, the final response in physiochemical characterization is associated to three different natures (Figure 1.5).

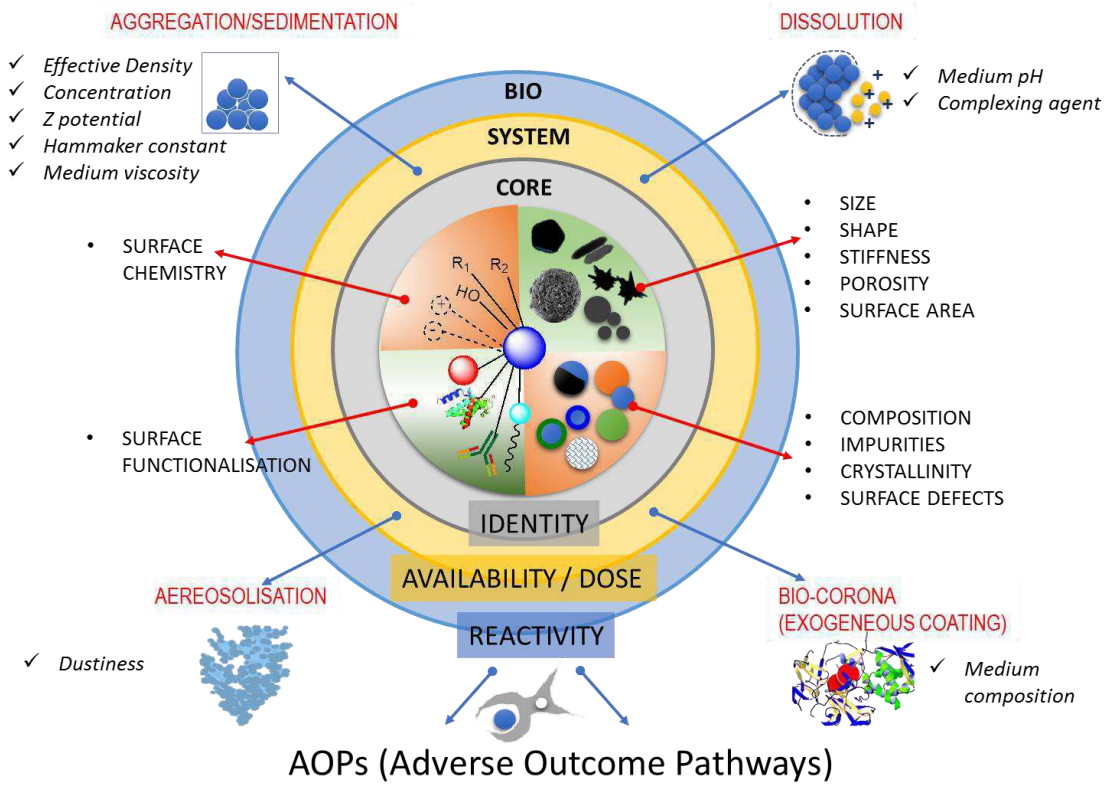

Figure 1.5: Scheme of possible property on a generic NM once in contact with biological target.

Firstly, the NMs intrinsic properties – such as chemistry composition, physical shape, surface functionalization, … - have to be evaluated, taking in to account the NM as it is after the production. Secondly the system-dependent property can provide info about the behaviour of NMs in media (agglomeration, *corona* formation, …). In conclusion, the interaction with biological compartments provides information about NMs reactivity and possible AOPs development. Ideally, all of these properties, as well as many others, would be used to obtain a complete picture of the NM[85]. Therefore, provide a full NMs physicochemical characterization is one of the most difficult and challenging problem. Incomplete characterization of NMs is a major limitation for comparing results between different studies for both quality control on material production and nano-safety studies[86].

References

1. Feynman, R. P. There's plenty of room at the bottom (Transcript of Talk Given on December 29, 1959, at the Annual Meeting of the American Physical Society). *Caltech Eng. Sci.* **23**, 22–36 (1960).

2. Khan, I., Saeed, K. & Khan, I. Nanoparticles: Properties, applications and toxicities. *Arab. J. Chem.* (2017). doi:10.1016/j.arabjc.2017.05.011

3. Jeevanandam, J., Barhoum, A., Chan, Y. S., Dufresne, A. & Danquah, M. K. Review on nanoparticles and nanostructured materials: History, sources, toxicity and regulations. *Beilstein J. Nanotechnol.* **9**, 1050–1074 (2018).

4. Tiquia-Arashiro, S. & Rodrigues, D. Application of Nanoparticles. in *Extremophiles: Applications in Nanotechnology* 163–193 (Springer International Publishing, 2016). doi:10.1007/978-3-319-45215-9_5

5. Unser, S., Bruzas, I., He, J. & Sagle, L. Localized surface plasmon resonance biosensing: Current challenges and approaches. *Sensors (Switzerland)* **15**, 15684–15716 (2015).

6. Weiss, J., Takhistov, P. & McClements, D. J. Functional Materials in Food Nanotechnology. *J. Food Sci.* **71**, R107–R116 (2006).

7. Meyyappan, M. Nanotechnology in Aerospace Applications. 38 (2007).

8. Tratnyek, P. G. & Johnson, R. L. Nanotechnologies for environmental cleanup. *Nano Today* **1**, 44–48 (2006).

9. Rongchao, J. The impacts of nanotechnology on catalysis by precious metal nanoparticles. *Nanotechnology Reviews* **1**, 31 (2012).

10. Serrano, E., Rus, G. & García-Martínez, J. Nanotechnology for sustainable energy. *Renew. Sustain. Energy Rev.* **13**, 2373–2384 (2009).

11. Wong, Y. W. H., Yuen, C. W. M., Leung, M. Y. S., Ku, S. K. A. & Lam, H. L. I. Selected applications of nanotechnology in textiles. *Autex Res. J.* **6**, 1–8 (2006).

12. Giese, B. *et al.* Risks, Release and Concentrations of Engineered Nanomaterial in the Environment. *Sci. Rep.* **8**, 1–18 (2018).

13. Inshakova, E. & Inshakov, O. World market for nanomaterials: Structure and trends. *MATEC Web Conf.* **129**, 1–5 (2017).

14. Piccinno, F., Gottschalk, F., Seeger, S. & Nowack, B. Industrial production quantities and uses of ten engineered nanomaterials in Europe and the world. *J. Nanoparticle Res.* **14**, (2012).

15. Postnote, T. Risk assessment of nanomaterials. *Nanotechnol. Environ.* 29–61 (2009).

16. Commission, T., European, T. & Joint, C. L 275/38. 2010–2012 (2011).

17. Boverhof, D. R. *et al.* Comparative assessment of nanomaterial definitions and safety evaluation considerations. *Regul. Toxicol. Pharmacol.* **73**, 137–150 (2015).

18. Rauscher, H. *et al. European Commission, Joint Research Centre: Towards a review of the EC Recommendation for a definition of the term "nanomaterial" part 3, JRC Scientific and Policy Report EUR 27240 EN*. (2015). doi:10.2788/678452

19. Roebben, G. *et al. Towards a review of the EC Recommendation for a definition of the term " nanomaterial " Part 2 : Assessment of collected information concerning the experience with the definition Edited by*. (2014). doi:10.2787/97286

20. Rauscher, H. *et al. European Commission, Joint Research Centre: Towards a review of the EC Recommendation for a definition of the term " nanomaterial " Part 1 : Compilation of information concerning the experience with the definition, JRC Scientific and Policy Report EUR 265*. *Luxembourg: Publications Office of the European Union* (2014). doi:10.2788/36237

21. Alenius, H., Norppa, H., Pylkkänen, L., Tuomi, T. & Kasper, G. Risk assessment of engineered nanomaterials and nanotechnologies—A review. *Toxicology* **269**, 92–104 (2010).

22. Kuhlbusch, T. A. J., Asbach, C., Fissan, H., Göhler, D. & Stintz, M. Nanoparticle exposure at nanotechnology workplaces: A review. *Part. Fibre Toxicol.* **8**, 1–18 (2011).

23. Peralta-Videa, J. R. *et al.* Nanomaterials and the environment: A review for the biennium 2008–2010. *J. Hazard. Mater.* **186**, 1–15 (2011).

24. Directive-2006/1907/EC. Directive 2006/1907/EC on Registration, Evaluation and Authorization of Chemicals (REACH). *Off. J. Eur. Union* **396**, 1–849 (2006).

25. British Standards Institute. *Nanomaterials and Nanotechnology-based Products – Guide to Regulation and Standards*. (2013).

26. Stone, V. *et al.* ITS-NANO - Prioritising nanosafety research to develop a stakeholder driven intelligent testing strategy. *Part. Fibre Toxicol.* **11**, 9 (2014).

27. ECHA. *Guidance on Information Requirements and Chemical Safety*.

28. Organisation for Economic Co-operation and Development. Recommendation of the Council on the Safety Testing and Assessment of Manufactured Nanomaterials. 1–8 (2017).

29. Directorate, E. *et al.* JOINT MEETING OF THE CHEMICALS COMMITTEE AND THE WORKING PARTY ON CHEMICALS, PESTICIDES AND BIOTECHNOLOGY GUIDANCE MANUAL FOR THE TESTING OF MANUFACTURED NANOMATERIALS: OECD's SPONSORSHIP PROGRAMME; FIRST REVISION. (2010).

30. www.nanosafetycluster.eu. *NanoSafety Cluster*

31. ECHA. Appendix R . 6-1 : Recommendations for nanomaterials applicable to the Guidance on QSARs and Grouping. 29 (2017). doi:10.2823/884050

32. ECHA RIVM JRC. Usage of (eco) toxicological data for bridging data gaps between and grouping of nanoforms of the same substance. (2017).

33. Gajewicz, A. *et al.* Decision tree models to classify nanomaterials according to the DF4nanoGrouping scheme. *Nanotoxicology* **12**, 1–17 (2018).

34. Giusti, A. *et al.* Nanomaterial grouping: Existing approaches and future recommendations. *NANOIMPACT* 100182 (2019). doi:10.1016/j.impact.2019.100182

35. Rebitzer, G. *et al.* Life cycle assessment: Part 1: Framework, goal and scope definition, inventory analysis, and applications. *Environ. Int.* **30**, 701–720 (2004).

36. Sahoo, S. K., Parveen, S. & Panda, J. J. The present and future of nanotechnology in human health care. *Nanomedicine Nanotechnology, Biol. Med.* **3**, 20–31 (2007).

37. Zhang, L. *et al.* Nanoparticles in Medicine: Therapeutic Applications and Developments. **83**, 761–769 (2008).

38. Rao, C. N. R. & Cheetham, A. K. Science and technology of nanomaterials: Current status and future prospects. *J. Mater. Chem.* **11**, 2887–2894 (2001).

39. Weir, A., Westerhoff, P., Fabricius, L., Hristovski, K. & Von Goetz, N. Titanium dioxide

nanoparticles in food and personal care products. *Environ. Sci. Technol.* **46**, 2242–2250 (2012).

40. Bouwmeester, H. *et al.* Review of health safety aspects of nanotechnologies in food production. *Regul. Toxicol. Pharmacol.* **53**, 52–62 (2009).

41. Lincoln, U. of N. Safe Operating Procedure. *Opacity Emiss. from Combust. Sources* **11**, 1–4 (2011).

42. Oberdörster, G. & Kuhlbusch, T. A. J. In vivo effects: Methodologies and biokinetics of inhaled nanomaterials. *NanoImpact* **10**, 38–60 (2018).

43. Larese Filon, F., Mauro, M., Adami, G., Bovenzi, M. & Crosera, M. Nanoparticles skin absorption: New aspects for a safety profile evaluation. *Regul. Toxicol. Pharmacol.* **72**, 310–322 (2015).

44. Crosera, M. *et al.* Nanoparticle dermal absorption and toxicity: A review of the literature. *Int. Arch. Occup. Environ. Health* **82**, 1043–1055 (2009).

45. Hamm, J. *et al.* Alternative approaches for identifying acute systemic toxicity: Moving from research to regulatory testing. *Toxicol. Vitr.* **41**, 245–259 (2017).

46. Monopoli, M. P. *et al.* Physical−Chemical Aspects of Protein Corona: Relevance to in Vitro and in Vivo Biological Impacts of Nanoparticles. *J. Am. Chem. Soc.* **133**, 2525–2534 (2011).

47. Manke, A., Wang, L. & Rojanasakul, Y. Mechanisms of nanoparticle-induced oxidative stress and toxicity. *Biomed Res. Int.* **2013**, (2013).

48. Rasmussen, K. *et al.* Physico-chemical properties of manufactured nanomaterials - Characterisation and relevant methods. An outlook based on the OECD Testing Programme. *Regul. Toxicol. Pharmacol.* **92**, 8–28 (2018).

49. Gottschalk, F. & Nowack, B. The release of engineered nanomaterials to the environment. *J. Environ. Monit.* **13**, 1145–1155 (2011).

50. Shandilya, N., Le Bihan, O., Bressot, C. & Morgeneyer, M. Emission of titanium dioxide nanoparticles from building materials to the environment by wear and weather. *Environ. Sci. Technol.* **49**, 2163–2170 (2015).

51. Patil, S. S., Shedbalkar, U. U., Truskewycz, A., Chopade, B. A. & Ball, A. S. Nanoparticles for environmental clean-up: A review of potential risks and emerging solutions. *Environ. Technol. Innov.* **5**, 10–21 (2016).

52. Keller, A. A., McFerran, S., Lazareva, A. & Suh, S. Global life cycle releases of engineered nanomaterials. *J. Nanoparticle Res.* **15**, 1692 (2013).

53. Verschoor, A. J. *et al.* Systematic selection of a dose metric for metal-based nanoparticles. *NanoImpact* **13**, 70–75 (2019).

54. Arenas-Lago, D., Abdolahpur Monikh, F., Vijver, M. G. & Peijnenburg, W. J. G. M. Dissolution and aggregation kinetics of zero valent copper nanoparticles in (simulated) natural surface waters: Simultaneous effects of pH, NOM and ionic strength. *Chemosphere* **226**, 841–850 (2019).

55. Zhu, X., Wang, J., Zhang, X., Chang, Y. & Chen, Y. Trophic transfer of TiO2 nanoparticles from daphnia to zebrafish in a simplified freshwater food chain. *Chemosphere* **79**, 928–933 (2010).

56. Corsi, I. Toxic effects of engineered nanoparticles in the marine environment: Model organisms and molecular approaches. *Mar. Environ. Res.* **76**, 32–40 (2012).

57. Fantke, P. *et al.* Toward harmonizing ecotoxicity characterization in life cycle impact assessment. *Environ. Toxicol. Chem.* **37**, 2955–2971 (2018).

58. Rico, C. M., Majumdar, S., Duarte-Gardea, M., Peralta-Videa, J. R. & Gardea-Torresdey, J. L.

Interaction of nanoparticles with edible plants and their possible implications in the food chain. *J. Agric. Food Chem.* **59**, 3485–3498 (2011).

59. Servin, A. D. *et al.* Synchrotron verification of TiO2 accumulation in cucumber fruit: A possible pathway of TiO2 nanoparticle transfer from soil into the food chain. *Environ. Sci. Technol.* **47**, 11592–11598 (2013).

60. Theng, B. K. G. & Yuan, G. Nanoparticles in the soil environment. *Elements* **4**, 395–399 (2008).

61. Van Broekhuizen, P., Van Veelen, W., Streekstra, W. H., Schulte, P. & Reijnders, L. Exposure limits for nanoparticles: Report of an international workshop on nano reference values. *Ann. Occup. Hyg.* **56**, 515–524 (2012).

62. Schulte, P. A., Murashov, V., Zumwalde, R., Kuempel, E. D. & Geraci, C. L. Occupational exposure limits for nanomaterials: State of the art. *J. Nanoparticle Res.* **12**, 1971–1987 (2010).

63. Howard, J. Current Intelligence Bulletin 65: Occupational Exposure to Carbon Nanotubes and Nanofibers. *DHHS Publ.* 184 (2013).

64. AHHS; CDC; NIOSH. Occupational Exposure to Titanium Dioxide. *Curr. Intell. Bull.* **160**, 140 (2011).

65. Weldon, B. A. *et al.* Occupational exposure limit for silver nanoparticles: considerations on the derivation of a general health-based value. *Nanotoxicology* **10**, 945–956 (2016).

66. Haber, L. T. *et al.* Benchmark dose (BMD) modeling: current practice, issues, and challenges. *Crit. Rev. Toxicol.* **48**, 387–415 (2018).

67. Guidances, T. Development of a web based REACH Toolkit to safety assessment of Guidance on available methods for risk assessment of nanomaterials Technical Guidances. (2015).

68. U.S. Environmental Protection Agency. Benchmark Dose Technical Guidance. 1–99 (2012).

69. EU SCIENCE HUB The European Commission's science and knowledge service. IATA - Integrated Approaches to Testing and Assessment. *Alternative methods for toxicity testing* (2018).

70. www.oecd.org. Integrated Approaches to Testing and Assessment (IATA). *2019 Organisation for Economic Co-operation and Development*

71. European Chemicals Agency. Guidance on information requirements and chemical safety assessment: QSARs and grouping of chemicals. *Guid. Implement. Reach* **R.6**, 134 (2008).

72. Arts, J. H. E. *et al.* Case studies putting the decision-making framework for the grouping and testing of nanomaterials (DF4nanoGrouping) into practice. *Regul. Toxicol. Pharmacol.* **76**, 234–261 (2016).

73. Arts, J. H. E. *et al.* A decision-making framework for the grouping and testing of nanomaterials (DF4nanoGrouping). *Regul. Toxicol. Pharmacol.* **71**, S1–S27 (2015).

74. Oomen, A. G. *et al.* Grouping and read-across approaches for risk assessment of nanomaterials. *Int. J. Environ. Res. Public Health* **12**, 13415–13434 (2015).

75. Prior, H., Casey, W., Kimber, I., Whelan, M. & Sewell, F. Reflections on the progress towards non-animal methods for acute toxicity testing of chemicals. *Regul. Toxicol. Pharmacol.* **102**, 30–33 (2019).

76. Archibald, K., Coleman, R. & Drake, T. Animal Experimentation: Working Towards a Paradigm Change. *Anim. Exp. Work. Towar. a Paradig. Chang.* (2019). doi:10.1163/9789004391192

77. Valsami-Jones, E. & Lynch, I. How safe are nanomaterials? *Science (80-.).* **350**, 388 LP – 389 (2015).

78. Nel, A. *et al.* Nanomaterial Toxicity Testing in the 21st Century: Use of a Predictive Toxicological Approach and High-Throughput Screening. *Acc. Chem. Res.* **46**, 607–621 (2013).

79. Bergamaschi, E. *et al.* Impact and effectiveness of risk mitigation strategies on the insurability of nanomaterial production: Evidences from industrial case studies. *Wiley Interdiscip. Rev. Nanomedicine Nanobiotechnology* **7**, 839–855 (2015).

80. E.U. Council Directive 98/24/Ec. *Off. J. Eur. Communities* **L 269**, 1–22 (2014).

81. European Commission. Council Directive 2004/37/EC of 29 April 2004 on the protection of workers from the risks related to exposure to carcinogens or mutagens at work (Sixth individual Directive within the meaning of Article 16 (1) of Council Directive 89/391/EEC. *Off. J. Eur. Communities* 23–30 (2004).

82. JOINT MEETING OF THE CHEMICALS COMMITTEE. IMPORTANT ISSUES ON RISK ASSESSMENT OF MANUFACTURED NANOMATERIALS. *OECD Environ. Heal. Saf. Publ. Ser. Saf. Manuf. Nanomater.* (2012).

83. Scott-Fordsmand, J. J. *et al.* A unified framework for nanosafety is needed. *Nano Today* **9**, 546–549 (2014).

84. Hale, A., Kirwan, B. & Kjellén, U. Safe by design : where are we now ? **45**, 305–327 (2007).

85. Johnston, L. J., Mansfield, E. & Smallwood, G. J. Physicochemical Properties of Engineered Nanomaterials. *Metrol. Stand. Nanotechnol.* 99–114 (2017). doi:10.1002/9783527800308.ch5

86. Krug, H. F. Nanosafety research-are we on the right track? *Angew. Chemie - Int. Ed.* **53**, 12304–12319 (2014).

2. Aim of the thesis

Risk assessment is a process that integrates the hazard, exposure, and dose–response data to characterize risk in a population (e.g. workers or biota), in order to provide health information (benchmark, limit doses that ensure a safe exposure) needed for risk management decision-making[1]. The main goal of my Ph.D. thesis is to support risk assessment of NMs focusing on the characterization and control of properties and behaviors, that affect external and internal exposure, driving potentially hazardous mechanisms.

Through five case studies, the experimental design were set up for measuring NMs intrinsic properties (such as composition, dimension, superficial area, ...), system-dependent properties (such as aggregation and dissolution in media) and fate related properties, considering exposure to both human and environmental targets[2]. Each case study was selected based on the research needs and knowledge gaps, and is associated to different classes (groups) of NMs (Figure 2.1) in order to facilitate the "read-across" approach for hazard and risk assessment[3–6]. Therefore, we selected six different NMs, belonging to soluble (MG1), passive (MG3) and active (MG4) groups and applied them in the five case studies.

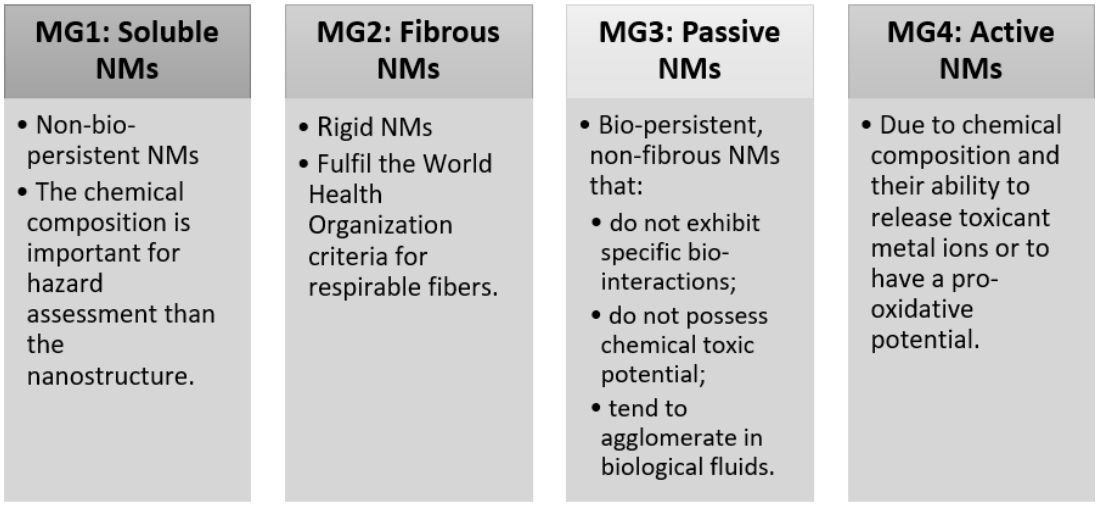

Figure 2.1: NMs grouping based on nano-bio interaction and physiochemical properties described following DF4nanoGrouping (Arts et al., 2015).

For what concern human exposure scenarios, the case studies were focused on metal and metal oxide-based NPs, due to their widespread use in technologically relevant application[7,8]. The objective was to investigate the adverse effects of selected NPs through two possible human exposure routes: transdermal and oral ingestion. At this purpose, skin and oral mucosa were selected as *in-vitro ex-vivo* target membranes of the diffusion Franz cell model[9], in

order to investigate the permeation and penetration through human skin and oral mucosa[10,11]. A scheme of the selected case studies is reported in Figure 2.2. We compared the skin permeation and penetration of silica dioxide (SiO_2 NPs), belonging to passive NMs group (MG3), to that of copper oxide (CuO NPs), belonging to the partially soluble NMs group (MG1) metal. Whilst for the oral mucosa exposure route, we selected a soluble (MG1) metal-based nanoparticles as silver (Ag NPs). We believe that data collected will contribute to dosimetry adjustment of dermal and oral mucosa exposure-dose-response studies, in order to derive more relevant reference doses (DNEL, ADI, …). In addition, the knowledge of NMs fate across dermal barriers will provide information on human exposure potential and mechanism.

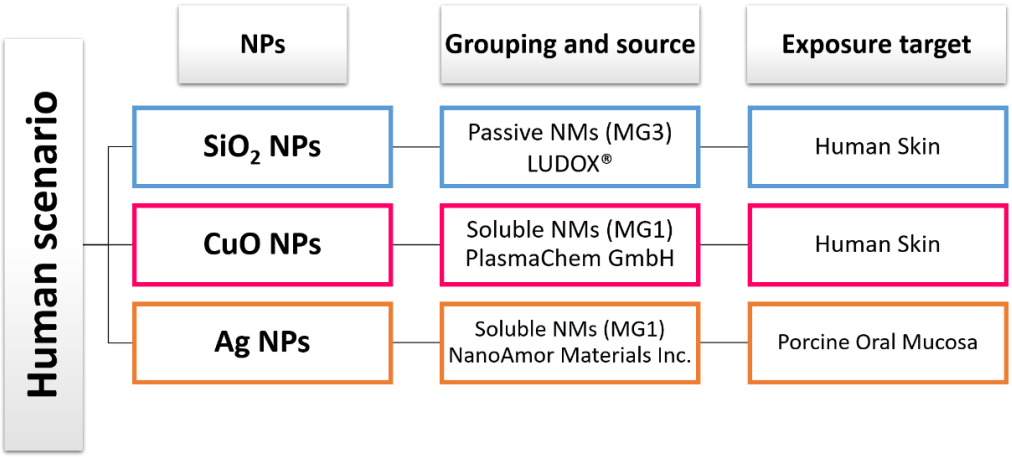

Figure 2.2: Human exposure case studies.

For what concern environmental targets, we evaluated the behavior of three metal oxide NPs, belonging to partially soluble (zinc oxide nanoparticles, ZnO NPs) and reactive (titanium dioxide nanoparticles, TiO_2 NPs and cerium dioxide nanoparticles, CeO_2 NPs) groups in two water compartments: fresh and sea water (Figure 2.3).

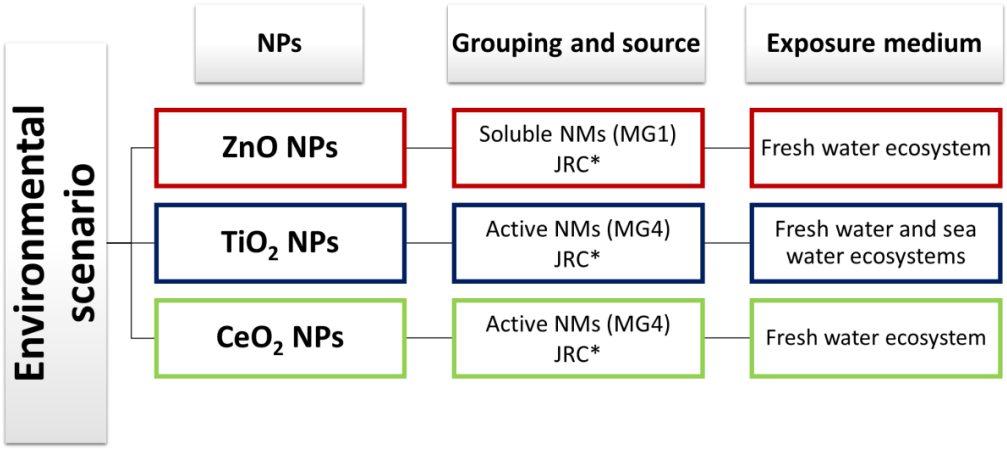

Figure 2.3: Environmental exposure case studies. *Joint Research Centre - Europa EU (JRC)[13]

The aim of the work was to support the study of NPs fate in water ecosystems, by characterizing how intrinsic properties change in environmental relevant media. Three main endpoints were addressed: static dissolution, agglomeration degree and distribution along the water-column, evaluated in acellular *in-vitro* systems. We selected Elendt M7 medium for fresh water and Egg Water medium for marine water, because used as reference media for *in-vivo* tests, respectively with *Daphnia magna* and *Zebrafish (Danio rerio)* species. The final aim of this work was that to provide physicochemical data that can be used to improve eco-tox dose-response model and derive more accurate reference values (PNEC) for scientific and regulatory purposes.

For all addressed case studies the same testing strategy was followed, we collected information on intrinsic properties (such as size, shape, …), that outline nature of NPs, then we dispersed NPs in relevant media, characterizing the so called system-depended properties, resulting from the interaction with medium components (salts, co-exposed molecules, pH), and finally for human scenarios we evaluated the *in-vitro ex-vivo* translocation through dermal or oral mucosa membranes with Franz cell tests. The testing strategy is summarized in Figure 2.4, with color indicating the case studies and the expected information that will be reported in the following chapters.

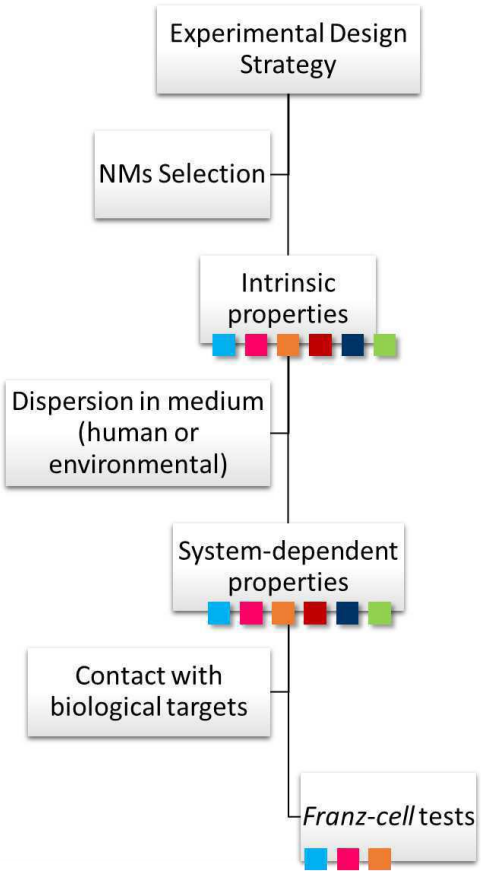

Figure 2.4: Design strategy for the (■) SiO_2 NPs, (■) CuO NPs, (■) Ag NPs, (■) ZnO NPs, (■) TiO_2 NPs and (■) CeO_2 NPs.

The selection of reference materials (RMs) - as ZnO, TiO_2 and CeO_2 NPs - and commercial representative NMs - as SiO_2, CuO and Ag NPs - in support to risk assessment[12] facilitates the “read-across” approach and the transfer of information, evidences, mechanisms to all the NMs within the grouping class.

References

1. Kuempel, E. D., Geraci, C. L. & Schulte, P. A. Risk assessment and risk management of nanomaterials in the workplace: Translating research to practice. *Ann. Occup. Hyg.* **56**, 491–505 (2012).

2. Utembe, W., Potgieter, K., Stefaniak, A. B. & Gulumian, M. Dissolution and biodurability: Important parameters needed for risk assessment of nanomaterials. *Part. Fibre Toxicol.* **12**, 11 (2015).

3. Arts, J. H. E. *et al.* A decision-making framework for the grouping and testing of nanomaterials (DF4nanoGrouping). *Regul. Toxicol. Pharmacol.* **71**, S1–S27 (2015).

4. Scott-Fordsmand, J. J. *et al.* A unified framework for nanosafety is needed. *Nano Today* **9**, 546–549 (2014).

5. Oomen, A. G. *et al.* Grouping and read-across approaches for risk assessment of nanomaterials. *Int. J. Environ. Res. Public Health* **12**, 13415–13434 (2015).

6. Arts, J. H. E. *et al.* Case studies putting the decision-making framework for the grouping and testing of nanomaterials (DF4nanoGrouping) into practice. *Regul. Toxicol. Pharmacol.* **76**, 234–261 (2016).

7. Inshakova, E. & Inshakov, O. World market for nanomaterials: Structure and trends. *MATEC Web Conf.* **129**, 1–5 (2017).

8. Giese, B. *et al.* Risks, Release and Concentrations of Engineered Nanomaterial in the Environment. *Sci. Rep.* **8**, 1–18 (2018).

9. Franz, T. J. Percutaneous Absorption. On the Relevance of in Vitro Data. *J. Invest. Dermatol.* **64**, 190–195 (1975).

10. Adams, D. Penetration of water through human and rabbit oral mucosa in vitro. *Arch. Oral Biol.* **19**, 865-IN11 (1974).

11. Roblegg, E. *et al.* Evaluation of a physiological in vitro system to study the transport of nanoparticles through the buccal mucosa. *Nanotoxicology* **6**, 399–413 (2012).

12. SCENIHR (Scientific Committee on Emerging and Newly Identified Health Risks). Risk Assessment of Products of Nanotechnologies. 71 (2009).

13. European Commission. Joint Research Centre (JRC) - EU Science Hub - Bringing together scientific knowledge for Europe. *https://ec.europa.eu/jrc/en* (2019).

14. European Chemicals Agency. Guidance on information requirements and chemical safety assessment: QSARs and grouping of chemicals. *Guid. Implement. Reach* **R.6**, 134 (2008).

15. Hale, A., Kirwan, B. & Kjellén, U. Safe by design : where are we now ? **45**, 305–327 (2007).

3. Fate in *in-vitro ex-vivo* human model

To fulfill the gap in research knowledge and provide useful information for future hazard evaluation using *in-vitro* extrapolation, my research was focused on two main uptake routes: skin and oral mucosa NPs adsorption. The decision was supported by the know-how of the University of Trieste.

For both exposure routes, we followed the same rationale based on an initial physiochemical characterization of NMs / NPs selected in the case study once dispersed in the simulant fluid and following a quantification in the *in-vitro* selected model.

Percutaneous and buccal absorption studies were both performed using the Franz model (1975)[1] (Figure 3.1), a diffusion cell used and applied to the biological membrane, respectively skin or oral mucosa, depending on the case study. The diffusion cell set-up presents in the top a donor chamber, where NMs / NPs are dispersed in the simulant medium and exposed to the biological membrane. in the center the membrane, skin or oral mucosa, is clamped between the donor and the receptor compartment. The receptor chamber/compartment has a function of receptor fluid of the *in-vitro* model, continuously stirred and thermostated at a constant temperature (32°C for skin and 37°C for oral mucosa) by the jacket surrounding the cell (water jacket).

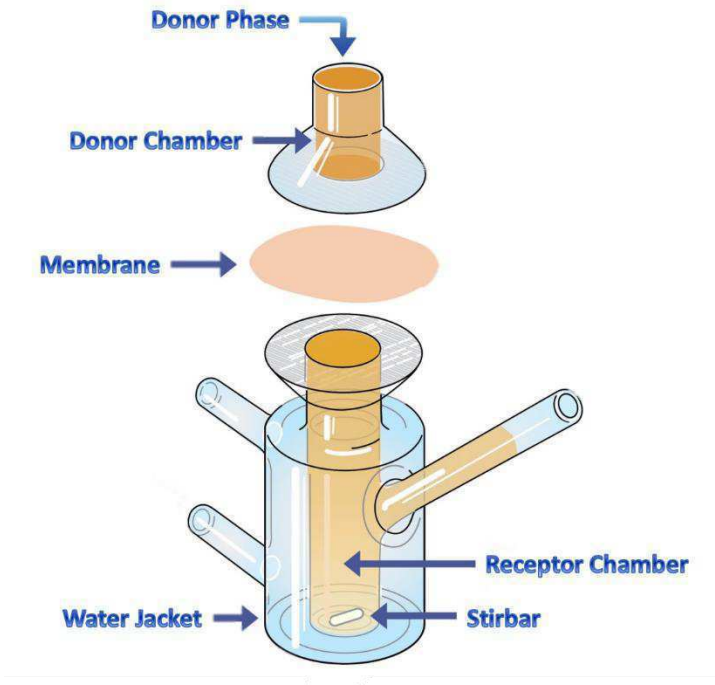

Figure 3.1: Franz cell experimental set-up.

The Franz model can provide two descriptors, penetration and permeation of NMs / NPs once in contact with the skin or the oral mucosa. Penetration occurs when NMs / NPs are detected within the skin / buccal layers, while permeation process is basically due NMs / NPs (or ions released), that are able to cross the membrane and pass in the receptor fluid[2,3]. To detect NMs / NPs penetration / permeation both the membrane and the receptor fluid have to be analyzed after exposure.

3.1 Skin membrane

The skin is one of the larger organ of the body, accounting for more than 10% of body mass[4,5], forming, as a consequence, a great area over which intentional and unintentional exposure to chemicals (in form of particles, cosmetics, clothing, handling products) can occur[6,7]. The skin barrier is composed of two layers: the epidermis and the dermis (Figure 3.2).

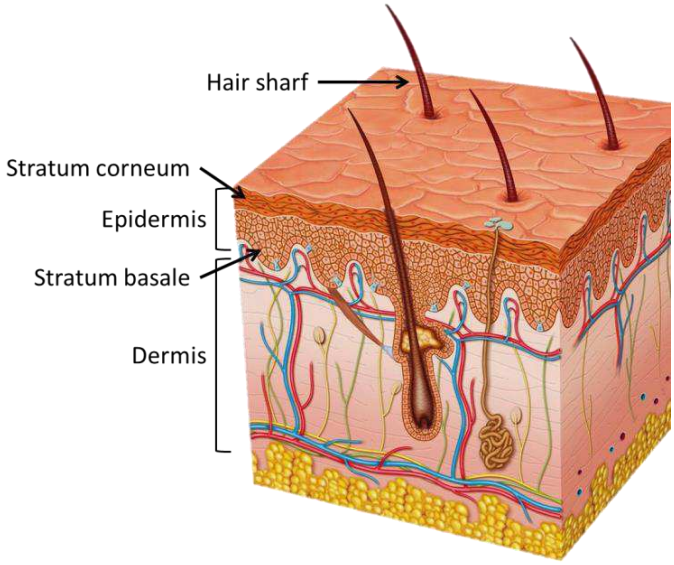

Figure 3.2: Structure schematize of human skin, mainly divided in epidermis and dermis.

The epidermis is made of a stratified squamous keratinized epithelium, which consists of two kinds of primary cells: the keratinocytes and the non-keratinocytes. The former cells are stratified in different layers (stratum basale, stratum spinosum, stratum granulosum, stratum lucidum, and stratum corneum), while the second own protection functions (against UV-light damage) and immunological functions (melanocytes, Merkel cells and Langerhans cells)[8]. The outermost layer is the stratum corneum, which acts as the first barrier to external agents; it modulates chemicals, drugs and particles absorption into the deeper skin layers. Its thickness can vary depending on the body regions (thicker in the palm and sole, thinner in scrotum and body flexures). Therefore, one of the main functions of the skin is to act as a barrier, allowing body protection from external substances. Even so, it is well-known that some compounds are capable to penetrate and permeate this barrier and cause possible local effects, such as

irritation or sensitization phenomena, or also translocate into blood vessels reaching systemic circulation and other organs. Thus, the skin adsorption is mainly derived by two contributes: the skin healthy and integrity, and different properties of NMs such as chemistry, composition and further physicochemical properties, such as dissolution ability and size dimension[2,6] can influence this mechanism.

A lot of chemicals can come in contact with the skin, either in their bulk form or in the nano-size range. For example, there are already many applications of various NPs in dermatology, such as photoprotection, photothermal and photodynamic therapy, hair disorders treatment, and also in gene therapy, vaccination and nanodiagnostics[9]. Currently, mostly skin absorption information is in relation to drugs, cosmetics, toxins, metal salts and powders exposure. Many of these potentially toxic substances are labeled with “skin notation” by the American Conference of Governmental Industrial Hygienists (ACGIH), which warns that cutaneous exposure to these compounds may significantly contribute to total systemic exposure[10]. However, the interaction of NPs with the skin is still a matter of investigation by researchers, since it has been demonstrated that some NPs can penetrate the outer stratum corneum layer of the skin, while others can permeate into the deeper dermal layer, reaching the systemic circulation[11–13]. In fact, one of the first topics that should be clarified is the mechanism of NPs penetration through the outermost rate-limiting barrier of the stratum corneum. Some authors hypothesized that NPs may be hold in the lipid matrix of the skin or in skin annexes and subsequently can be slowly released into the deeper dermal layer[14,15]. Concerning this theory, some characteristics such as NPs size, shape, charge, surface properties have to be further investigated to better understand which of them, and eventually in which degree, can affect skin penetration. In addition, since NPs characteristics may change completely when they interact with physiological media, also changes due to media have to considered, evaluating NPs aggregation and agglomeration, and perhaps change in surface charge[2].

3.2 Oral mucosa membrane

The oral mucosa is the mucous membrane, covering the inside of the human mouth. These soft tissues comprise stratified squamous epithelium, termed "oral epithelium", that covers entirely the human oral cavity (Figure 3.3)[16]. Like epidermis for the skin, the regions stressed by mechanical forces associated with mastication are covered by a keratinizing epithelium (masticatory mucosa). In this area, the keratinized epithelium is tightly attached to the underlying tissues by a collagenous connective tissue, called lamina propria.

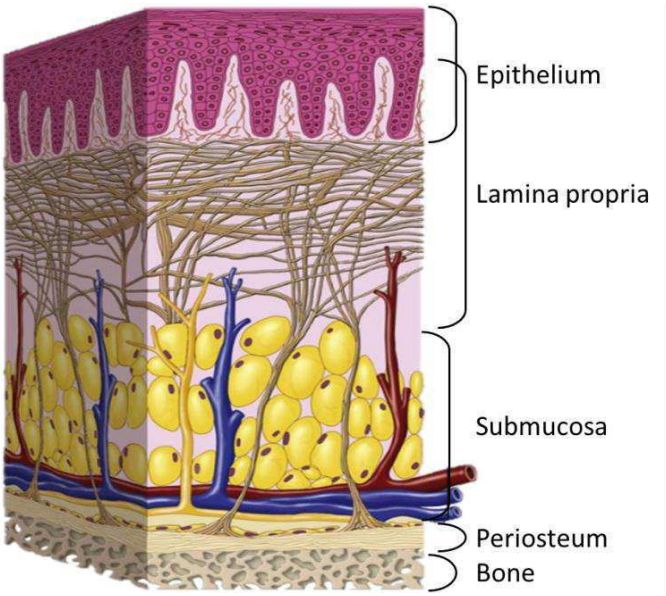

Figure 3.3: Structure of lining oral mucosa.

Otherwise, the mouth floor, buccal regions, and esophagus, which require flexibility to accommodate chewing, speech, or swallowing of a bolus, are covered with a non-keratinizing epithelium (lining mucosa). The connective tissue of lining mucosa is more elastic and flexible than the connective tissue in the masticatory mucosa. As in skin, mucosal cells are able to differentiate and migrate from the stratum basale to the surface. The epithelium is then separated from the submucosa by a muscularis mucosa, consisting of a smooth muscle and elastic fiber layer, which may serve to reduce the excursion of the luminal lining mucosa as a result of the contractions of the external esophageal muscle. The organization of the tissues reflects so their function, transporting ingested food from the oral cavity to the stomach[17].

As in skin, the primary function of oral and esophageal epithelium is the protection of the underlying tissue. Lipid-based permeability barriers in the outer epithelial layers protect the underlying tissues against the ingress of a range of potentially damaging external substances. These include microbial toxins and enzymes and antigens and carcinogens from foods and beverages. However, if few information is available on skin, less is known about NPs absorption by the human oral mucosa.

3.3 Case studies

During my PhD program, I focused my research on three case studies using the *in-vitro ex-vivo* Franz model, mimicking human dermal or oral exposure. Looking at the global production volumes, the main class of nano-size products is composed by metal and metal / non-metal oxide-based NPs[18,19]. Therefore, I selected silicon dioxide nanoparticles (SiO_2 NPs) and copper oxide nanoparticles (CuO NPs) to compare the behaviors of passive oxides with

partially soluble oxides[20] (Figure 3.4) when exposed to derma, whilst for oral exposure, I selected silver nanoparticles (Ag NPs) as target NMs. The choice was due to the low availability of data on this specific scenario. In addition, due to the similarity between human and porcine, I used porcine oral mucosa to evaluate the penetration / permeation of NPs in baby individuals. The experimental design strategy is summarized below for the human related case studies (Figure 3.4).

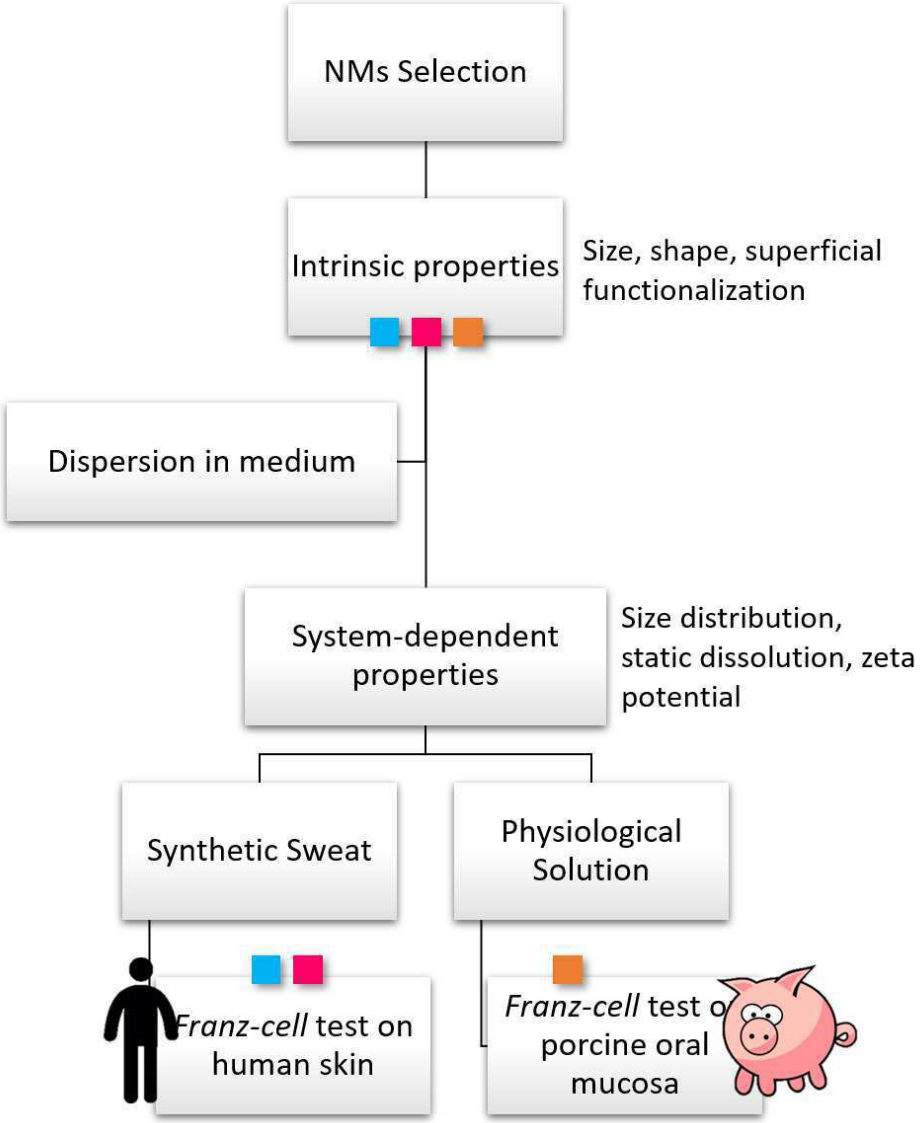

Figure 3.4: Experimental design strategy for the human related case studies SiO_2 NPs (■), CuO NPs (■) and Ag NPs (■).

References

1. Franz, T. J. Percutaneous Absorption. On the Relevance of in Vitro Data. *J. Invest. Dermatol.* **64**, 190–195 (1975).
2. Larese Filon, F., Mauro, M., Adami, G., Bovenzi, M. & Crosera, M. Nanoparticles skin absorption: New aspects for a safety profile evaluation. *Regul. Toxicol. Pharmacol.* **72**, 310–322 (2015).
3. Guth, K., Schäfer-Korting, M., Fabian, E., Landsiedel, R. & van Ravenzwaay, B. Suitability of skin integrity tests for dermal absorption studies in vitro. *Toxicol. Vitr.* **29**, 113–123 (2015).
4. Walters, K. A. & Roberts, M. S. The Structure and Function of Skin, The Pilary Apparatus. in *Dermatological and Transdermal Formulations* (2002).
5. Monteiro-Riviere, N. A. & Baroli, B. *Toxicology of the Skin*. (2010).
6. Crosera, M. *et al.* Nanoparticle dermal absorption and toxicity: A review of the literature. *Int. Arch. Occup. Environ. Health* **82**, 1043–1055 (2009).
7. Poland, C. A. *et al.* Dermal Absorption of Nanomaterials - Part of the "Better control of nano" initiative 2012-2015. in *The Danish Environmental Protection Agency* (2013). doi:10.11648/j.nano.20140204.14
8. Monteiro-riviere, N. A. & Filon, F. L. *Skin*. *Adverse Effects of Engineered Nanomaterials* (Elsevier Inc., 2017). doi:10.1016/B978-0-12-809199-9/00015-X
9. Papakostas, D., Rancan, F., Sterry, W., Blume-Peytavi, U. & Vogt, A. Nanoparticles in dermatology. *Arch. Dermatol. Res.* **303**, 533 (2011).
10. Sartorelli, P. *et al.* How to improve skin notation. Position paper from a workshop. *Regul. Toxicol. Pharmacol.* **49**, 301–307 (2007).
11. Crosera, M. *et al.* Titanium Dioxide Nanoparticle Penetration into the Skin and Effects on HaCaT Cells. *Int. J. Environ. Res. Public Health* **12**, 9282–9297 (2015).
12. Mortensen, L. J. *et al.* Quantification of quantum dot murine skin penetration with UVR barrier impairment. *Nanotoxicology* **7**, 10.3109/17435390.2012.741726 (2013).
13. Baroli, B. *et al.* Penetration of Metallic Nanoparticles in Human Full-Thickness Skin. *J. Invest. Dermatol.* **127**, 1701–1712 (2007).
14. Zhang, L. W., Yu, W. W., Colvin, V. L. & Monteiro-Riviere, N. A. Biological interactions of quantum dot nanoparticles in skin and in human epidermal keratinocytes. *Toxicol. Appl. Pharmacol.* **228**, 200–211 (2008).
15. Rancan, F. & Vogt, A. Getting under the skin: what is the potential of the transfollicular route in drug delivery? *Ther. Deliv.* **5**, 875–877 (2014).
16. Cruchley, A. T. & Bergmeier, L. A. Structure and Functions of the Oral Mucosa. in *Oral Mucosa in Health and Disease: A Concise Handbook* (ed. Bergmeier, L. A.) 1–18 (Springer International Publishing, 2018). doi:10.1007/978-3-319-56065-6_1
17. Nanci, A. *Ten Cate's Oral Histology Development, Structure, and Function*. *Elsevier* (Elsevier Health Sciences, 2017).
18. Inshakova, E. & Inshakov, O. World market for nanomaterials: Structure and trends. *MATEC Web Conf.* **129**, 1–5 (2017).
19. Giese, B. *et al.* Risks, Release and Concentrations of Engineered Nanomaterial in the Environment. *Sci. Rep.* **8**, 1–18 (2018).
20. Giusti, A. *et al.* Nanomaterial grouping: Existing approaches and future recommendations. *NANOIMPACT* 100182 (2019). doi:10.1016/j.impact.2019.100182

3.3.1 Silica nanoparticles for photo-induced self-marker and antibacterial function

Source (published papers):

"Methylation of Ir(III)-tetrazolato complexes: an effective route to modulate the emission outputs and to switch to antimicrobial properties". V. Fiorini, I. Zanoni, S. Zacchini, A. L. Costa, A. Hochkoeppler, V. Zanotti, A. M. Ranieri, M. Massi, A. Stefan and S. Stagni, Dalton Transaction, 2017, 46, 12328.[1]

"Encapsulation of cationic iridium(III) tetrazole complexes into a silica matrix: synthesis, characterization and optical properties". I. Zanoni, V. Fiorini, M. Rosado, B. Ballesteros, M. Androulidaki, M. Blosi, S. Ortelli, S. Stagni, M. Dondi and A. L. Costa, New Journal of Chemistry, 2018, 42, 9635-9644.[2]

"Use of cotton textiles coated by Ir(III) tetrazole complexes within ceramic silica nanophases for photo-induced self-marker and antibacterial function". I. Zanoni, M. Blosi, V. Fiorini, M. Crosera, S. Ortelli, S. Stagni, A. Stefan, S. Psilodimitrakopoulos, E. Stratakis, F. Larese Filon, A. L. Costa (under submission paper)

Introduction

The demand for innovative, functional and smart textiles is one of the major challenges that fabric and clothing industries are requested to face nowadays. In particular, the end user market requires accessible products associated with advanced features that nanomaterials can satisfy, such as photocatalytic performance and self-cleaning properties[3,4,] antimicrobial activity[5,6,] photo and thermochromism[7], and fire retardancy[8,9,10]. One novel approach pursued to realize this kind of innovative materials involves the coating of textile surfaces with nanoparticles (NPs), capable to impart specific functionalities, once anchored to their surface, without compromising their comfort, easy care, and hygiene[11]. At this purpose, one of the main challenge, strictly related to the need of controlling product safety and quality, is the possibility to easily detect the presence of NPs and monitoring their persistence and distribution, in each step pf product life-cycle[12], from manufacturing to use and end of life. At this purpose, we have developed the design strategy schematized in Scheme 3.1.1, combining the following components: silica NPs (embedding matrix), phosphorescent dyes formed by cationic Iridium(III) tetrazole complexes[1,2,13,14] (marking phases), cotton textiles (substrate) to be covered by the resulting luminescent systems. Silica is well known for its chemical, optical and thermal inertia, with a proven compatibility with light emitting transition metals-based complexes[15,16], available at affordable cost[17]. Cyclometalated Ir(III) complexes are widely known for their intense and

color tunable luminescent output, which is found to span the entire spectrum of visible light as a consequence of slight modifications of their chemical structure. These peculiar photoluminescent performances have prompted the use of Ir(III) cyclometalates as emitters in lighting devices, and as suitable luminescent bioprobes[14,18,19,20]. On the other hand, in comparison with Ru(II) and many other classes of metal-based derivatives, the antimicrobial properties of Ir(III) complexes have been explored to a lesser extent. In this regard, promising anti-microbial potential of a set of kinetically stable and substitution inert cationic cyclometalated complexes towards Gram(+) bacteria (e.g. *Staphylococcus aureus* and *Deinococcus radiodurans*)[1,21,22,23] was recently demonstrated, therefore adding further possibilities for applications of this class of luminescent compounds. For the above described properties, the strategy developed and schematized in Scheme 3.1.1 suggests the potential application of luminescent silica based NPs as self-marking, antibacterial coating for textile. However, to finalize their application in textile coatings, the potential risk that SiO_2 NPs and their marking Ir(III) complexes can cause to human skin (the final biological target) must be evaluated. In fact, the non-negligible cellular toxicity and a scarce biocompatibility of poorly water soluble Iridium (III) complexes, limited their use in biomedical field[24,25], even if opened some interesting applications in cancer therapy[28,29,30].

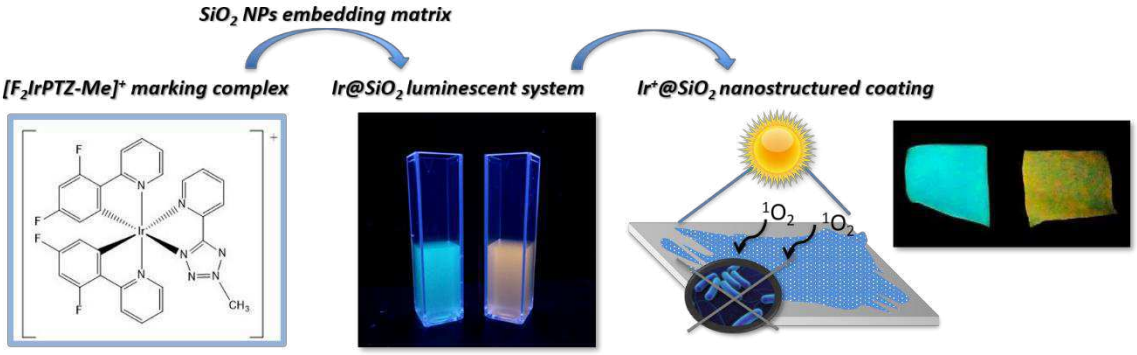

Scheme 3.1.1: Design strategy of the work make by combining silica NPs (embedding matrix), with cationic Ir(III) tetrazole complexes (marking phases), and applied as coating for cotton textiles (substrate).

In this study we have selected two cationic Ir(III)-tetrazole complexes, **$[F_2IrPTZ\text{-}Me]^+$** and **$[IrQTZ\text{-}Me]^+$,** which display different luminescent properties, we have embedded them in a silica NPs matrix and investigated the optical properties antibacterial effects once embedded inside the matrix used as a cotton coating medium. The results reported herein highlight switching on of their antimicrobial activity toward both Gram(+) (*Deinococcus radiodurans*) and Gram(-) (*Escherichia coli*), upon embedding in silica matrix (**Ir@SiO_2 systems**), and on cotton textiles.

Given the possible potential risk that NPs and Ir(III) markers can cause, we evaluated the possible penetration of Ir@SiO_2 NPs through human skin, using Franz cell model, in support to risk assessment and management of this potential application.

Experimental section

General Considerations. All the reagents and solvents were obtained commercially (e.g. Merck, Alfa Aesar, Strem Chemicals) and used as received without any further purification. The commercial colloidal suspension of silica (Silica LUDOX® HS-40) was supplied by Grace Davison and destabilized using a commercial exchange resin Dowex 50x8 protons (Merck), with MESH value of 20-50 and total exchange capacity of 1.7 meq mL^{-1}. The purification of the Ir(III) complexes was performed via column chromatography with the use of Al_2O_3 as the stationary phase. Appendix 1-mass spectra were recorded using a Waters ZQ-4000 instrument (ESI-MS, acetonitrile as the solvent). Nuclear magnetic resonance spectra (consisting of ^1H and ^{13}C) were always recorded using a Varian Mercury Plus 400 (^1H, 399.9; ^{13}C, 101.0 MHz). ^1H and ^{13}C chemical shifts were referenced to residual solvent resonances. As textile substrate we used a 260 g m^{-2}, 98% cotton fabric and 2% EA elastomer containing about 85% polyurethane.

Ligand synthesis. Warning! Tetrazole derivatives are used as components for explosive mixtures[31]. In this lab, the reactions described here were only run on a few grams scale and no problems were encountered. However, great care should be exercised when handling or heating compounds of this type. Following the general method reported by Koguro and co-workers[32], tetrazole ligands [H-**PTZ**] and [H-**QTZ**] has been obtained in quantitative yield.

General Procedure for the Preparation of the Cationic Ir(III) complexes. The preparation of cationic Ir(III)-complexes was accomplished by following the previously reported procedure by Fiorini et al. (2017)[1]. 1 eq of the desired neutral Ir(III) tetrazolate complex was added to dichloromethane and the mixture was allowed to cool down by immersion into an ethanol / liquid nitrogen cold bath. Then, methyl trifluoromethanesulfonate (1.2 equiv., solution in dichloromethane 0.179 M) was added. The reaction was stirred under nitrogen for 30 minutes while in thermal contact with a cold bath, and then allowed to warm up to room temperature (RT) and stirred for 3 hours. Anion exchange was carried out by adding an excess of NH_4PF_6 in water to the solution and stirring for 20 minutes. The product was then extracted using dichloromethane (3×10 mL) and the organic components were combined and dried over anhydrous $MgSO_4$. Subsequent purification by column chromatography on alumina (gradient: CH_2Cl_2 / acetone 8:2, second fraction) yielded 0.059 g of **$[F_2IrPTZ\text{-}Me]^+[PF_6]^-$** and 0.067 g of **$[IrQTZ\text{-}Me]^+[PF_6]^-$**.

General procedure for the colloidal physical encapsulation. The Ir(III)-tetrazole based nanosols were produced by following the previously reported procedure by Zanoni et al. (2018)[2]. We mixed $[F_2IrPTZ\text{-}Me]^+$ or $[IrQTZ\text{-}Me]^+$ with Silica LUDOX® HS-40 destabilized using Dowex 50x8, a commercial cationic exchange resin (Ir(III)tetrazole complex : SiO_2 nanosol ratio = 1:1000, w silica (%) = 3). To facilitate the mixing and the intimate interaction between the two phases, the systems were ball-milled for about 24 hours, in the presence of zirconia balls (diameter, Ø 5mm) as grinding bodies. Destabilization of Silica LUDOX® HS-40 was carried out in a 250 mL flask by adding the resin to the nano-suspension under vigorous stirring and monitoring the change in pH from 10 to 4. Once the desired pH was reached (pH = 4), the silica / resin contact was interrupted and the resin was extracted using a separation grid by vacuum pump filtration[2,4].

General procedure for the dip-pad-dry-cure process for coating cotton fabrics. Fabric samples, size 7x7 cm^2, were washed in an ultrasonic bath for 30 min (15 min with soap and water, and 15 min with water). The fabric coupons were dipped into the two different Ir@SiO_2 systems at 3% wt concentration and left to soak for 5 min, then passed through a two-roller laboratory padder, oven dried at 100°C and finally cured for 10 min at 130°C. Three impregnation steps were carried out to achieve the final dry add-on value (AO%) and, after each step, the fabric coupons were dried in an oven for 5 min at 100°C. The exact AO% values obtained are reported in Table 3.1.4. The dry-add on (AO%) is the amount, in percentage, of the finishing agent added to the fabric with respect to its initial weight. This was determined by weighing each sample before (w_i) and after (w_f) the dip-pad-dry-cure process, using a Sartorius balance (± 10^{-4} g)[4].

$$AO\% = \frac{(w_f - w_i)}{w_i} \text{ x } 100$$

Colloidal Characterization. Size and ZP (Zeta Potential - ζ-pot_{ELS}) measurements of the nano-solutions were carried out with a DLS / ELS (dynamic light scattering and electrophoretic light scattering Zetasizer Nano instrument ZSP, ZEN5600, Malvern Instruments, UK). The study of the colloidal behaviour and the interaction between silica and Ir(III) complexes (ZP vs pH) was carried out using a Zetasizer Nano instrument coupled with an automatic titrating system. The titration was performed with 1M KOH and 1M HCl solutions on the Ir(III)@SiO_2 systems at a concentration of 0.01%wt. The interaction between Ir(III) complexes and silica nanosol matrix was evaluated with TEM (transmission electron microscopy, FEI, Tecnai F20 S/TEM) equipped with an Energy Dispersive X-ray Analysis (EDX) probe.

Morphological characterization of cotton fabric samples. The morphology characterization of pristine and Ir@SiO_2-coated cotton fabrics was performed by electron microscopy analysis using a Field Emission Scanning Electron Microscope, FE-SEM (FEI Magellan 400L SEM High Resolution SEM). The uncoated and coated cotton fabric coupons (about 3mm x 3 mm) were fixed with conductive adhesive tape and gold metallized or silver pasted.

Photophysical characterization. Absorption spectra were recorded at RT using a Perkin Elmer Lambda 35 UV/vis spectrometer. Uncorrected steady-state emission and excitation spectra were recorded on an Edinburgh FLSP920 spectrometer equipped with a 450 W xenon arc lamp, double excitation and single emission monochromators, and a Peltier-cooled Hamamatsu R928P photomultiplier tube (185−850 nm). Emission and excitation spectra were acquired with a cut-off filter (395 nm) and corrected for source intensity (lamp and grating) and emission spectral response (detector and grating) by a calibration curve supplied with the instrument. Experimental uncertainties are estimated to be ± 8% for lifetime determinations, ± 20% for quantum yields, and ± 2 nm and ± 5 nm for absorption and emission peaks, respectively. More details on the photophysical investigations and characterization were reported in the Appendix 1 document[33,34]. The dispersion homogeneity of the complexes within the silica matrix, once deposited as coating, and textiles tomography were acquired by a 2p-Fluorescence Microscope as described in detail by Psilodimitrakopoulos et al. (2018)[35]. Briefly, the setup was based on a *fs* excitation laser source, centered at 1030 nm, with ~1 W output power and 76 MHz repetition rate (Pharos-SP, Light Conversion, Lithuania), and a 20x/0.8NA objective (Carl Zeiss, Germany) and emission sample was acquired with a bandpass filter (620 ± 52 nm, Semrock, USA) for Ir@SiO_2 systems. Qualitative analysis on images acquired by 2p-Fluorescence Microscope was done using ImageJ 1.52p software (National Institute of Health, USA).

Washing fastness test. The release of Ir(III) complex and silica NPs from treated cotton samples was performed under static and dynamic conditions to simulate washing cycles of the fabric while in use and to study adhesion to the substrate and quantify the weight loss[5]. The dynamic test was carried out by dipping 5x5cm^2 treated cotton samples (in 25 mL MilliQ) in an ultrasonic bath for 10 min for three cycles at RT, after every step the washing water was stored and analyzed at ICP-OES, then the sample was dried in the oven at 80° C for 10 minutes and washed again. The static test was performed by immersing the samples (size 7x7cm^2) in a MilliQ water bath (50 mL) at RT for to ten days and sampling washing water after one, four hours and one, three, four, seven and ten days. For the dynamic test we collected data from coated textiles, from silica-coated textiles and from samples coated with the two Ir@SiO_2 complexes.

Release under static conditions involved only the blue Ir@SiO_2 coated substrate as reference. The collected washing waters were analyzed by inductively coupled plasma optical emission spectrometry using an ICP-OES 5100 – vertical dual view apparatus (Agilent Technologies, Santa Clara, CA, USA) to determine SiO_2 and Ir@SiO_2 complex content. The analysis was performed using radial viewing mode, at a viewing height of 8 mm, and calibration curves were obtained with 0.1, 0.5, 5.0, 10.0 and 100.0 mg L^{-1} standards for all analyzed elements. Nitric Acid (65% - Titolchimica) was added to both standards and samples in 1:10 in volume ratio. Finally, all calibration curves were evaluated, finding an R^2 correlation coefficient >0.99. The concentration of SiO_2 in washing water was evaluated directly by ICP Si determination, while the release of Ir(III) complex was analysed taking the Ir amount as reference.

Bacterial strains and media. The Gram-negative Escherichia coli TOP10 strain (Invitrogen) was cultivated in Luria–Bertani (LB) medium (1% tryptone, 0.5% yeast extract, 1% NaCl). Solid plates were prepared by adding 1.5% agar. Deinococcus radiodurans, a red-pigmented Gram-positive bacterium, was grown in TGY medium (0.5% tryptone, 0.1% glucose, 0.3% yeast extract), to which 1.5% of agar was added if necessary.

Antibacterial evaluation. Antibacterial performances of Ir@SiO_2 coated textiles against *E. coli* e *D. radiodurans* were evaluated using the antibacterial activity assessment of textile materials – Parallel Steak Method (AATCC 147 modified) procedure[36]. A dilution (0.1 mL) of a liquid overnight culture (corresponding to approximately 1 × 108 CFU mL^{-1}) was smeared on LB and TGY agar plates in order to produce bacterial lawns. In the modified version of AATCC 147 we use a lawn of bacteria instead of the parallel streaks detailed in the standard method. Non-sterile sample of blue and red Ir@SiO_2 coated fabric are cut to 25 x 50 mm. These fabric samples are then placed directly on top of the inoculate agar and incubated at 30 ± 2°C for 24 hours. In our investigations, we compared three different lighting scenarios: darkness, exposed to lab light and exposed for 45 seconds to UV light (λ_{max} = 365 nm) and then to lab light for the 24 h of exposure. The incubated plates were examined for interruption of growth beneath the specimen, and for a clear zone of inhibition beyond its edge. Where no bacterial colonies growth is observed under the specimen with the presence of an inhibition zone, we considered to have an acceptable antibacterial activity. This test cannot be considered to be quantitative, but it can be used for comparison against non-antibacterial samples, and samples of known antibacterial activity. We have used resistant *Deinococcus radiodurans* (D. radiodurans) and *Escherichia coli* (E. coli), as our standard test organisms.

Preparation of skin membranes. Human abdominal full thickness skin was obtained as surgical waste. Prior to freezing, subcutaneous fat was removed and hair shaved. All the pieces of full thickness skin were stored in freezer at −25 °C for a period up to, but not exceeding, 4 months[37]. Skin integrity was assessed using the Trans Epidermal Water Loss (TEWL) method as described by Guth et al. (2015) and used in other our previous studies (Crosera et al. 2018)[38,39]. Cells with a value >10 g m^{-2} h^{-1} were considered as damaged and rejected. The study was approved by the Trieste Hospital Ethical Committee n° 236/2007.

In-vitro diffusion system. Percutaneous absorption studies were performed using static diffusion cells following the Franz Method (1975)[37]. The receptor compartment has a mean volume of 14.0 mL and was maintained at 32°C by means of circulation of thermostated water in the jacket surrounding the cell. This temperature value has been chosen in order to reproduce the hand's physiological temperature at normal conditions. The concentration of the salt in the receptor fluid is approximately the same as can be found in blood. The solution in each cell was continuously stirred using a Teflon-coated magnetic stirrer. Each piece of skin was clamped between the donor and the receptor compartment; the mean exposed skin area was 3.3 cm^2 and the average skin thickness was 1 mm.

The experiments were performed as follows. At time 0, the exposure chambers of four Franz diffusion cells were filled with 18 mg cm^{-2} of blue or red Ir@SiO_2 NPs solution dispersed in water (conc. 3% w/w) and diluted 1:2 with synthetic sweat at pH 4.5 to reproduce in vivo conditions (4 mL solution). Two blank cells were treated as the other cells with the exception that no Ir@SiO_2 dispersion was introduced into the exposure chamber. After 24 hours the receiving phases were collected to perform the concentration analysis and the skin samples removed, divided into epidermis and dermis by dipping them in hot water (60°C) for one minute (heat shock), and acid digested by microwave (MultiwavePRO, Anton Paar). An inductively coupled plasma mass spectrometry (ICP-MS) was used to measure Ir (mass selected: 193 u.m.a.) concentration in the receiving phase and in the solutions from the digestion of the skin membranes. The instrument used for the analysis was a NexION 350 X (Perkin Elmer, USA). The samples were analysed by measuring against standard solutions (0.01, 0.1, 1 and 10 µg L^{-1}) for instrumental calibration. The coefficient of variation (CV) for the analysis of Ir metal was always less than 5%. Data analysis was performed with Excel for Windows, release 2007 and Stata Software, version 11.0 (StataCorp LP, College Station, TX, USA). Skin absorption data were reported as mean ± standard deviation (SD). The difference among independent data was assessed by means of the Mann-Whitney test. A p value <0.05 was considered significant.

Results and discussion

Synthesis and characterization of luminescent Ir complex

In order to accomplish the functionalization of negatively charged SiO_2NPs, two cationic Ir(III) tetrazole complexes (Scheme 3.1.2) were selected as phosphorescent emitters chosen from a library that also includes the corresponding neutral and anionic cyclometalated Ir(III)-tetrazolates.

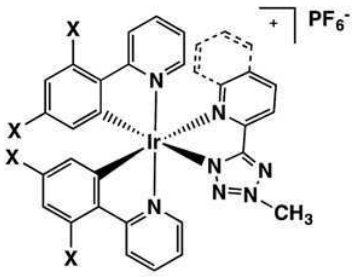

X = H, L = QTZ [IrQTZ-Me]$^+$
X= F, L = PTZ [F_2IrPTZ-Me]$^+$

Scheme 3.1.2: Molecular structure of cationic Ir(III) tetrazole complexes [F_2IrPTZ-Me]$^+$ and [IrQTZ-Me]$^+$.

The choice of considering these specific compounds, namely **[F_2IrPTZ-Me]$^+$** (C^N = F_2ppy; N^N = **PTZ-Me** - 2-(2-methyl-2*H*-tetrazol-5-yl)pyridine) and **[IrQTZ-Me]$^+$** (C^N = ppy; N^N = **QTZ-Me** -2-(2-methyl-2*H*-tetrazol-5-yl)quinoline), is motivated by their displaying markedly different emission colours. Indeed, whereas the luminescent output of **[F_2IrPTZ-Me]$^+$** consists of a vibronically structured profile centred in the blue region (λ_{max} = 490 nm) of the visible spectrum, the fluorine-free complex **[IrQTZ-Me]$^+$** exhibits a broad and unstructured radiative emission peaking at λ_{max}= 638 nm[1]. In 10^{-5}M CH_2Cl_2 solutions, all the cationic Ir(III) complexes displayed similar absorption profiles, with intense ligand centred (^{1}LC) transitions up to 260 nm and metal-to-ligand charge transfer (^{1}MLCT) bands tailing off above 380 nm (Figure 3.1.1a)[1,2,16]. Upon excitation of the ^{1}MLCT features (λ = 370 nm), **[F_2IrPTZ-Me]$^+$** displayed a sky-blue emission colour that corresponds to a structured emission profile with λ_{max} = 454, 486 and 526 nm (Figure 1b and Table 1), suggesting an interplay of ^{3}LC/^{3}MLCT-type emissive excited states[1,12,16]. On the contrary, the red emitter **[IrQTZ-Me]$^+$** produced a broad and unstructured emission profile with λ_{max}= 638 nm, typical of ^{3}MLCT-based phosphorescence (Figure 3.1.1b), as evidenced also by the noticeable rigidochromic shift observed in frozen solvent matrix at 77K (λ_{max} = 568 nm, Table 3.1.1)[2,12,16].

The complexes were prepared by following the procedure reported by Fiorini et al.[1], which consists of an electrophilic addition at the tetrazole ring of the corresponding neutral Ir(III) precursor. ^{1}H-NMR and ^{13}C-NMR characterizations are reported in Appendix 1 (Figure S1.1-S1.6).

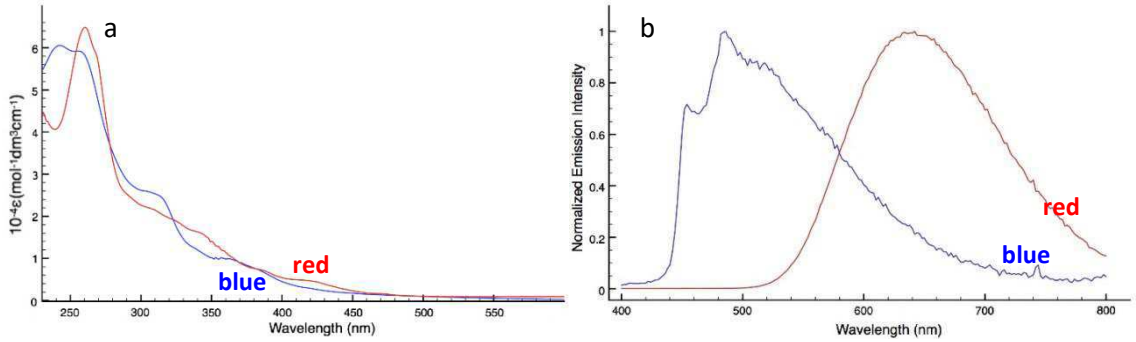

Figure 3.1.1: (a) Absorption Profiles of blue emitting **[F$_2$IrPTZ-Me]$^+$** (blue line) and red emitting **[IrQTZ-Me]$^+$** (red line), 10^{-5}M, CH_2Cl_2; (b) Normalized Emission Profiles of **[F$_2$IrPTZ-Me]$^+$** (blue line) and **[IrQTZ-Me]$^+$** (red line), CH_2Cl_2.

Table 3.1.1: Relevant absorption and emission data of cationic Ir(III) complexes discussed in this work.

CH_2Cl_2 as the solvent	**Absorption** λ_{abs}(nm);($10^{-4}\varepsilon$)($M^{-1}cm^{-1}$)	**Emission 298 K[a,b]**					**Emission 77K[c]**	
		λ_{em} (nm)	τ_{air} (µs)	τ_{Ar} (µs)	ϕ_{air} (%)	ϕ_{Ar} (%)	λ_{em} (nm)	τ (µs)
[IrQTZ-Me]$^+$	253 (4.25), 310 (1.41), 374 (0.78)	638	0.220	0.550	2.8	4.5	568	1.56
[F$_2$IrPTZ-Me]$^+$	257 (6.24), 318 (2.70), 351 (1.20)	454, 486, 526	0.040	0.140	1.7	4.7	448, 480	6.62

[a]:"Air" means air equilibrated solutions, "Ar" means deoxygenated solutions under argon atmosphere; [b]:[Ru(bpy)$_3$]Cl$_2$/H$_2$O was used as reference for quantum yield determinations (Φ_r = 0.028); [c]: in frozen CH_2Cl_2

Intrinsic properties of Ir@SiO$_2$ nanosols systems

Ir@SiO_2 nanosols (namely**: blue** Ir@SiO_2 for **[F$_2$IrPTZ-Me]$^+$** and **red** Ir@SiO_2 for **[IrQTZ-Me]$^+$**) were obtained by mixing the appropriate Ir(III) cationic complex with a silica suspension[17], which was previously destabilised through a cation-exchange resin treatment in which the replacement of Na^+ with H_3O^+ promotes the intra-particles cross-linking[18]. In this regard, an explanation is provided by Dumont and Watillon[19], that pointed out how the Na^+ substitution by H_3O^+ ions affect silica bonding, with the replacement of dissociated silanol-silanol bonds by cross-linked siloxane bonds: −Si−OH••••O^-−Si− ➔ −Si−O−Si + OH^-. In addition, the

electrostatic stabilization of resin treated silica nanoparticles decreases; in fact, Zeta Potential (ZP - ζ-pot$_{ELS}$) passes from -42 to -29 mV as expected by the pH decrease from 9.0 to 4.5 (Table 3.1.2). The colloidal properties of **Ir@SiO$_2$ nanosols** systems were studied in respect of their hydrodynamic diameter and surface charge properties (Table 3.1.2). As evidenced by the ZP vs pH measurements (Figure 3.1.2), the presence of the phosphorescent Ir(III) tetrazole-markers did not affect the surface charge properties of SiO_2NPs. For all the silica colloidal solutions, the obtained plots revealed only one isoelectric point (IEP) found at pH < 1.5, while the highest stability (ZP ≥ −30 mV) have been found between 3 < pH < 10 values. Furthermore, the hydrodynamic diameter of colloidal SiO_2NPs was not significantly affected by the physical mixing with the Ir(III)-markers, as confirmed by hydrodynamic diameter (d_{DLS}) values obtained from DLS analyses (Table 3.1.2).

Table 3.1.2: Colloidal properties of silica based nanosols.

Sample	***pH***	***d_{DLS} (nm)***	***ζ-pot$_{ELS}$ (mV)***
SiO_2_Ludox	9.0	20 ± 1	-42.2 ± 1.1
SiO_2*	4.5	23 ± 1	-29.0 ± 0.2
blue Ir@SiO_2	4.5	22 ± 2	-33.3 ± 1.8
red Ir@SiO_2	4.5	24 ± 1	-30.8 ± 1.5

**Commercial SiO_2 destabilized through treatment on cationic-exchange resin.*

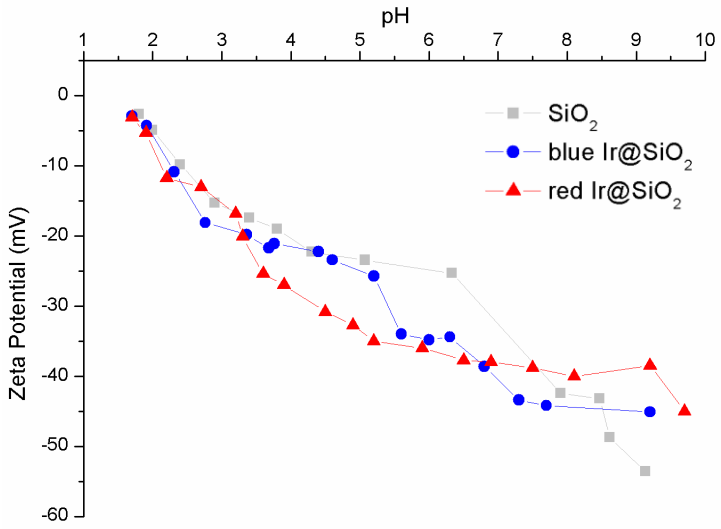

Figure 3.1.2: Zeta Potential (mV) vs pH plot of silica nanosol (grey line), blue **Ir@SiO$_2$** (blue line) and red **Ir@SiO$_2$** (red line), 100 mg L^{-1} of solid fraction.

The morphology of SiO_2 NPs and the distribution of the Ir(III) complexes were examined by the means of TEM-EDX (Figure 3.1.3 and 3.1.4). The NPs size distribution is homogeneously

centered on 14 nm, being these values in accordance with the measured d_{DLS} (Table 3.1.2). TEM images highlight a negligible increase of the SiO_2 NPs mean diameter (ØSiO_2 13.7±3.1 nm, Ø **blue Ir@SiO_2** 13.8±3.1 nm, Ø **red Ir@SiO_2** 14.0±3.4 nm) and a slight improvement of particles cross-linking in the presence of complexes, forming necklace-like structures (Figure 3.1.3, B-C). TEM images acquired at higher magnification revealed the presence of a halo in the surroundings of SiO_2NPs, imputable to the presence of Ir(III) complexes, as shown in Figure 3.1.4 and confirmed by EDX analysis.

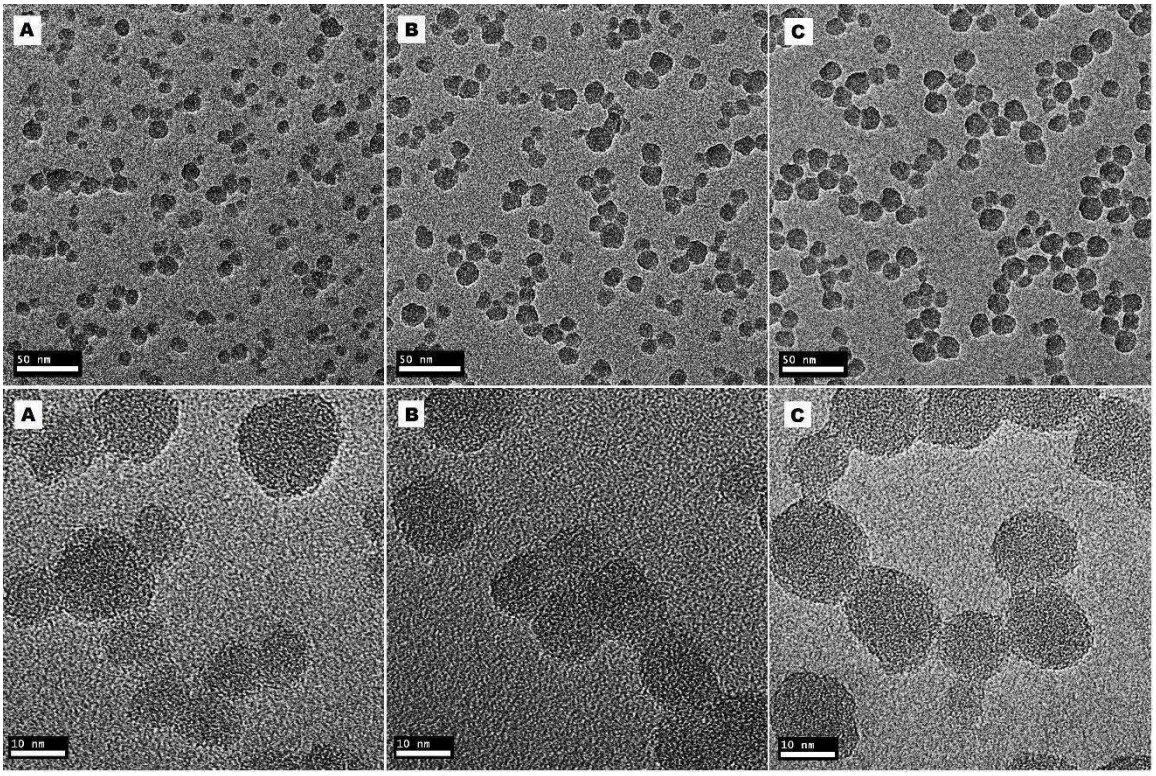

Figure 3.1.3: TEM images on copper grid acquired at different magnifications of A) SiO_2NPs, B) **blue Ir@SiO_2**, C) **red Ir@SiO_2**.

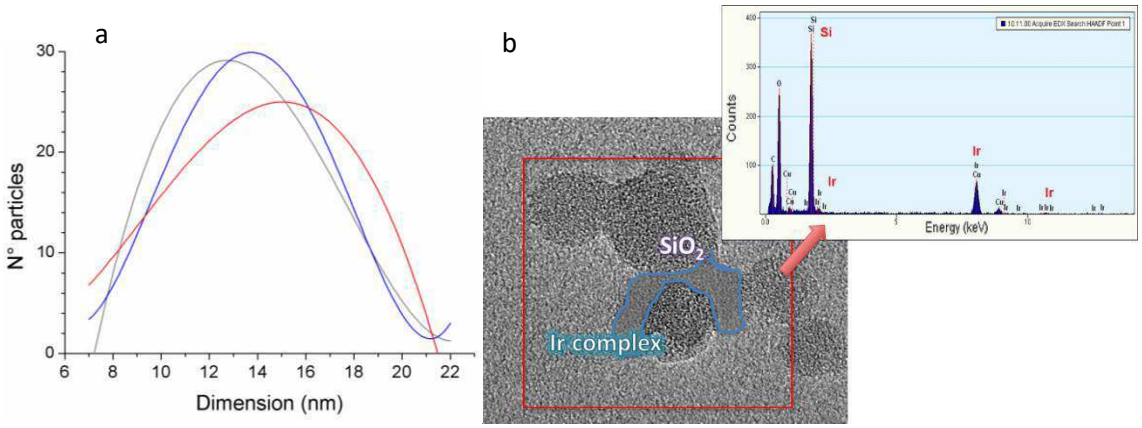

Figure 3.1.4: a) NPs distribution made by 250 particles-population: SiO_2NPs (grey line), **blue Ir@SiO_2** (blue line), **red Ir@SiO_2** (red line); b) TEM image of **blue Ir@SiO_2**, with relative EDX analysis.

As previously reported in literature[10], colloidal silica has no optical influence over the photoluminescent output of transition metal complexes, resulting transparent in both the absorption (230-400 nm) and emission range (400-800 nm). This behavior was confirmed by the absorption profile of SiO_2NPs (Figure 3.1.5), where no maxima were found in the region of interest.

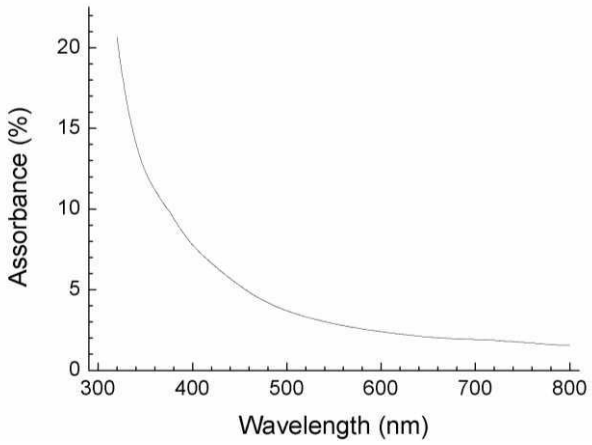

Figure 3.1.5: Absorbance (%) vs Wavelength (nm) plot of SiO_2NPs, 3%wt, Milli-Q H_2O, r.t.

The emission profiles of **[F_2IrPTZ-Me]$^+$** and its silica embedded structure **blue Ir@SiO_2** (Table 3.1.3 and Figure 3.1.6a) resulted almost superimposable to each other and did not provide any indication of the new chemical interaction established between **[F_2IrPTZ-Me]$^+$** and the silica matrix. On the other hand, the rigidochromic blue shift encountered in the emission profile of **red Ir@SiO_2** in respect of **[IrQTZ-Me]$^+$** (Table 3.1.3 and Figure 3.1.6b) is in agreement with the prevailing ^{3}MLCT composition of its excited state, being more sensitive to modifications of the surrounding chemical environment[1].

Table 3.1.3: Relevant photophysical properties of Ir(III)-complexes@SiO_2 nanosols systems.

H_2O as solvent	***Absorption*** λ_{abs}(nm)	***Emission 298 K***				
		λ_{em} (nm)	τ_{air} (µs)	τ_{Ar} (µs)	φ_{air} (%)	$\Delta\lambda$ (nm)
Red Ir@SiO_2	252, 312	610	0.100	n.d.*	n.d.*	28
Blue Ir@SiO_2	263, 286, 310	454, 484, 520	0.010	n.d.*	n.d.*	0

**n.d. = not determined.*

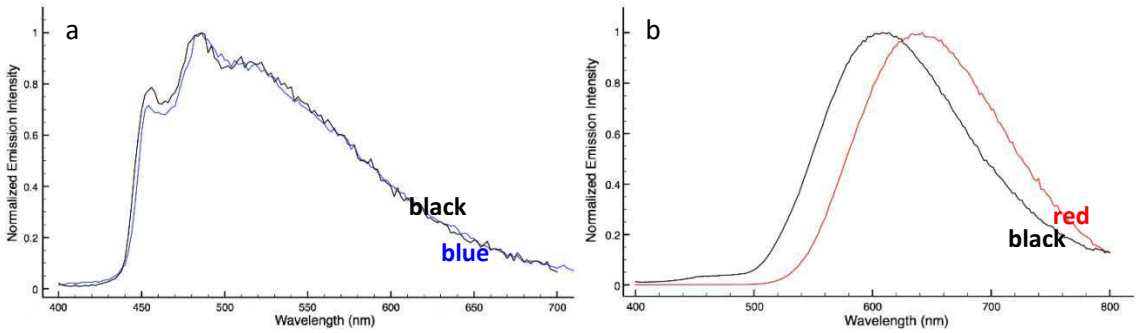

Figure 3.1.6: Comparison between normalised emission profiles **[F_2IrPTZ-Me]$^+$** (blue line) and **[IrQTZ-Me]$^+$** (red line) complexes and their **Ir@SiO_2 systems** (black lines).

The **Ir@SiO_2 systems** were performed and optimized with the aim of obtaining self-marker products that emit in the blue and red regions of visible light (**blue-** and **red-Ir@SiO_2,** due to the presence of **[F_2IrPTZ-Me]$^+$** and **[IrQTZ-Me]$^+$**, respectively). The physical mix was developed with easiness of design and processing in mind, while reducing the concentration of luminescent phase and in turn the manufacturing cost of the final material.

Ir@SiO_2 nano-coated textiles characterization

After optimization of dispersed **Ir@SiO_2** sols[2], we investigated their application in the field of markable nano-functionalized textiles. To this end, the luminescent **Ir@SiO_2** sol were anchored onto cotton textiles using the *dip-pad-dry-cure technique*, with thermal treatment in an oven used to strengthen the coating bond to the substrate. Since the presence of terminal hydroxides on SiO_2NPs allows interaction with large number of -OH groups on the surface of each fiber, the cellulose chain of cotton fibers is particularly well suited for this work's purposes[4]. As with most commercial cotton fibers[40], the commercial textiles samples used in this work contain an optical brightener, the presence of which is responsible for the emission centered at ca. 430 nm (Figure 3.1.7).

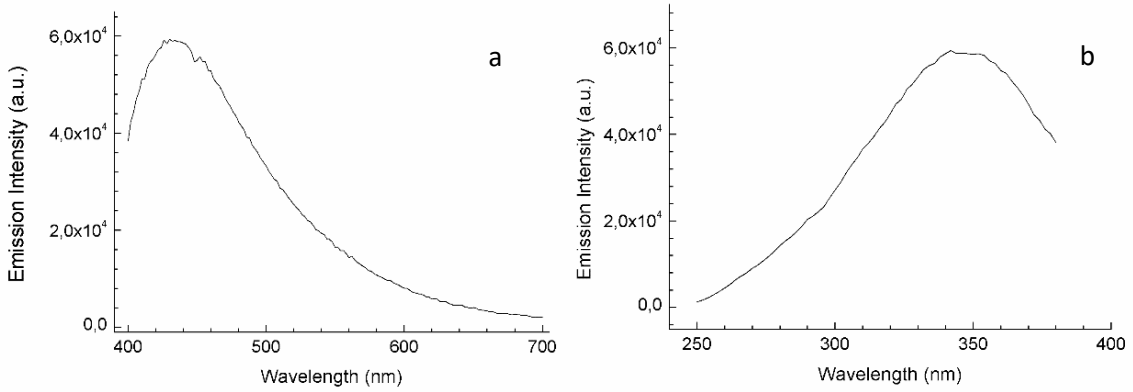

Figure 3.1.7: (a) Emission and (b) excitation profiles of untreated cotton textile.

Exploiting two-photon (2p) excited fluorescent emission of such dyed cotton, we are able to reproduce the textile 3D structure, using a 2p-fluorescence microscope and analyzing the first 350 µm of the surface, as shown in Figure 3.1.8.

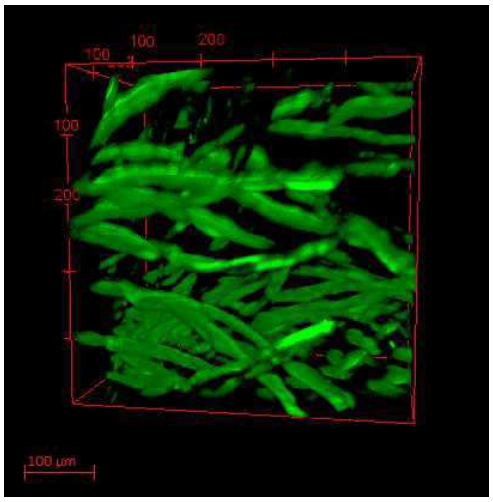

Figure 3.1.8: Tomography image of cotton textile (350 µm depth) made by 2p-Fluorescence Microscope.

Moreover, the emission from the optical brightener partially overlaps with the emission of **Ir@SiO$_2$** systems in the blue region of visible light. In order to ensure the optimal adhesion on cotton together with a noticeable emission typical of the **Ir@SiO$_2$** systems, we performed three impregnation steps on the treated textiles. The percent increment values, hereinafter referred to as the % add-on, showed a linear correlation between number of layers, nanosol concentration and solid content weight of the textiles (Table 3.1.4). In fact, the obtained add-on values after three impregnation layers are about threefold the nanosol concentration values (3% wt) without any effect induced by the iridium complex on the adhesion (Table 3.1.4), thus confirming a strong interaction between the nanostructured coating and the substrate[4].

Table 3.1.4: Add-on per cent values evaluated for three layers coated textiles.

	SiO$_2$*	**blue Ir@SiO$_2$**	**red Ir@SiO$_2$**
% add-on	7.9 ± 0.5	8.0 ± 0.7	8.9 ± 1.0

**Commercial SiO$_2$ destabilized by means of treatment with cationic-exchange resin.*

To investigate the coating distribution on the substrate, FE-SEM surface images were acquired both from untreated and **Ir@SiO$_2$**-coated samples. After two washing cycles with MilliQ water, the cotton fibers of the untreated sample (see Figure 3.1.9, A-B) still appear well organized and clean, except for small amounts of calcium carbonate $CaCO_3$, whose detection, is

consistent with a residual MilliQ water contaminant. At higher magnification it is possible to distinguish a characteristic superficial micro porosity of the cotton fiber, useful for the successive impregnation step (Figure 3.1.9B). On the other hand, as shown in Figure 3.1.9 (C-F), the two **Ir@SiO$_2$** nanosol systems applied on cotton textiles cover all the fabric area, filling the inter-fiber space and promoting a so-called *ceramized coating*. The primary nanosized spherical particles constituting the coating can be observed at higher magnification (Figure 3.1.9, D-F).

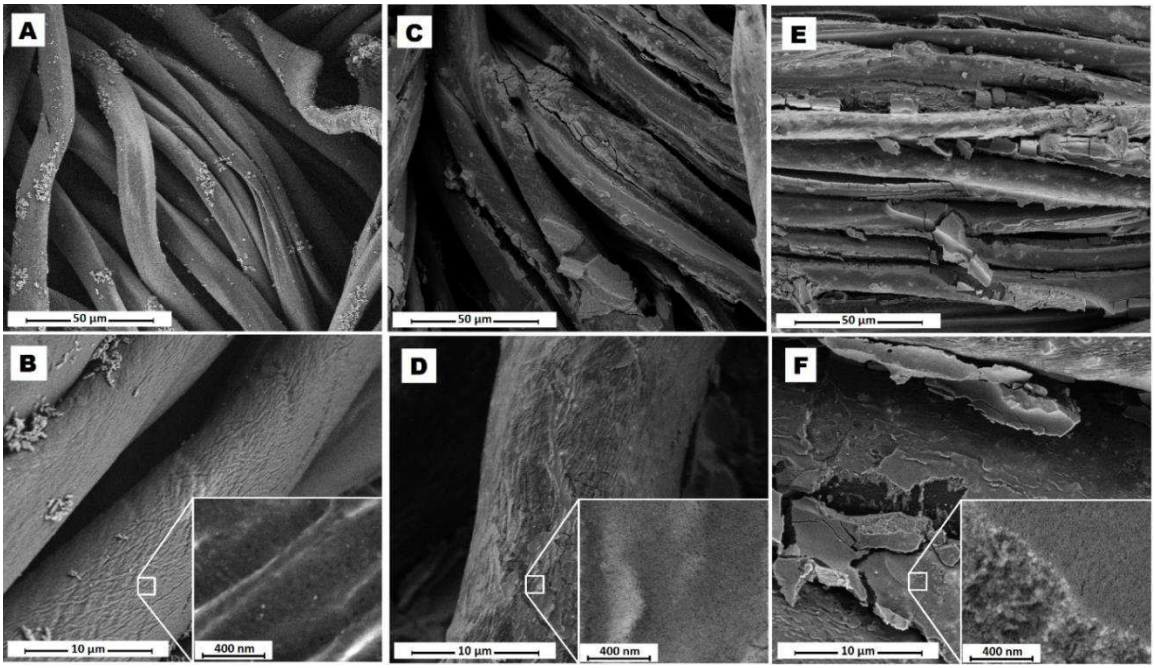

Figure 3.1.9: FE-SEM images of untreated cotton textile (A – B), blue Ir@SiO_2-coated textiles (C – D), red Ir@SiO_2-coated textiles (E – F) at different magnification.

Concerning the luminescent properties of the substrates after three treatment cycles, the data point out that all the prepared samples were qualitatively traceable under UV lamp (λ_{em}= 365 nm), showing an unchanged emission of Ir(III) complexes, with good dispersion of the complex into the silica matrix (Figure 3.1.10). Besides luminescence **Ir@SiO$_2$** coating imparts new functional properties to the treated textiles, such as hydrophilicity and abrasion resistance provided by the silica matrix. Luminescent emission from this kind of substrate represents an especially difficult goal to achieve, due to a liquid-to-solid state transfer of the chromophore molecules and to the presence of optical brighteners whose optical emission compete with and partly overlap the complexes' emission. However, by means of three-layer impregnation we were able to clearly distinguish the emission contribution of the complexes from that of the optical brightener. In this way, samples can be observed directly under the UV lamp, whereupon untreated and treated samples appear clearly different (Figure 3.1.10), maintaining the expected luminescent output. In particular, the corresponding emission spectra of the treated

samples result in broad spectral curves from the overlapping of Ir complex and brighter dye spectral profiles (Figure 3.1.11). Since the **blue Ir@SiO$_2$** system emits in the same visible range of the optical brightener, the resulting spectrum can roughly be considered as the sum of the two contributions without shifts in their emission maxima. In contrast, this drawback is not observed for the system based on **[IrQTZ-Me]$^+$**, *i.e.* **red Ir@SiO$_2$**. Indeed, the emission profile of **red Ir@SiO$_2$** was shifted from 610 nm for the nanosol state to 590 nm as a coating, due to the typical ^{3}MLCT-based emission evidenced also by the noticeable rigidochromic blue shift encountered at 77K (Figure S1.7 Appendix 1). As well, in passing from a nanosol dispersed system to a nanosol coating, the complex structure increases its stability due to silica embedding and solid state transfer, causing rigidochromic blue shift[18,20,41,42,43].

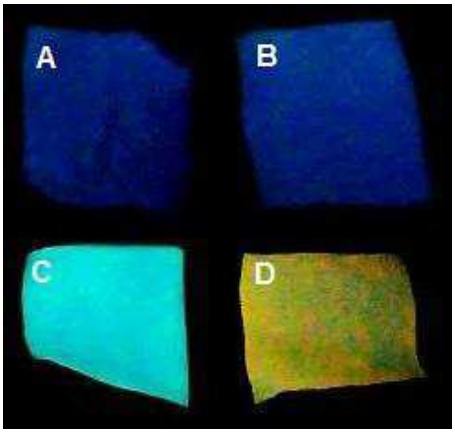

Figure 3.1.10: Real image of fabric samples under UV lamp (λ_{em}= 365 nm): uncoated (A), silica coated (B), **blue Ir@SiO$_2$** coated (C) and **red Ir@SiO$_2$** coated (D) cotton textiles.

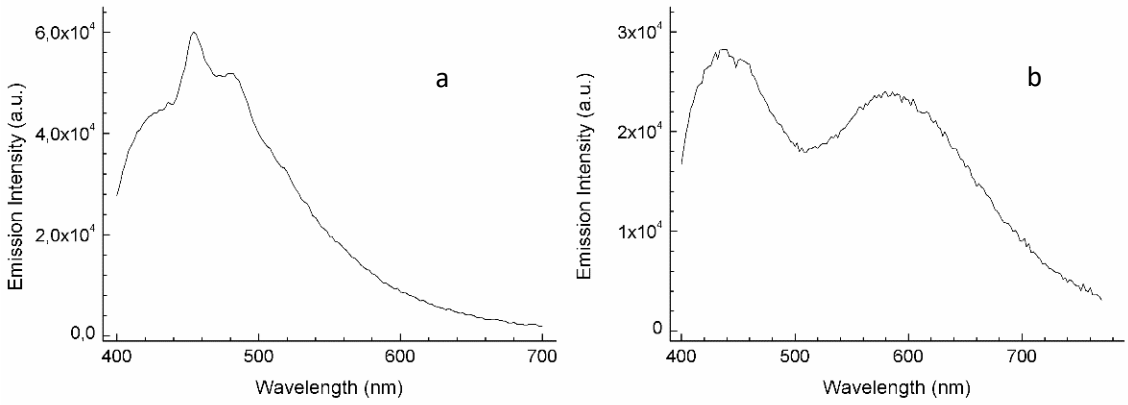

Figure 3.1.11: Emission profile of cotton textile coated by **blue Ir@SiO$_2$** system (a) and by **red Ir@SiO$_2$** system (b).

Taking advantage of the emission resulting from Ir(III) complexes, 2p-fluorescence microscopy was used to detect both distribution and homogeneity of **Ir@SiO$_2$** systems on

textiles. As shown in Figure 3.1.12, it is possible to reconstruct each single fiber of the fabric - detecting only the complexes emission - by cutting off the optical brightener contribution with a 620 ± 52 nm bandpass filter. The results evidenced that the complexes coupled and vehiculated by the silica matrix covered all the fibers in a homogeneous way. Using qualitative analysis by ImageJ software, we compared samples with and without the luminescent complexes. As expected **Ir@SiO$_2$** displayed much brighter emissions than both plain cotton and silica- coated cotton. In fact, by evaluating the color intensity of the images collected by fluorescence microscopy, in the presence of the **Ir@SiO$_2$** complexes we detected an increase of intensity by more than 1*10^6 counts.

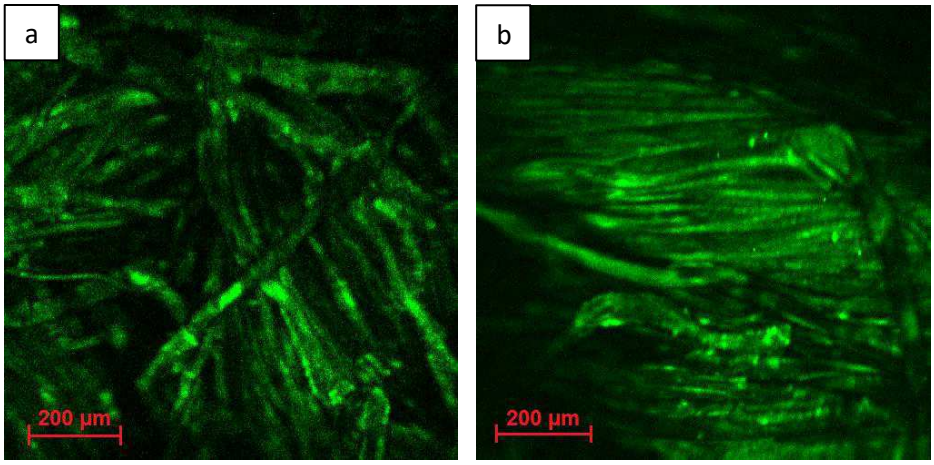

Figure 3.1.12: 2p-Fluorescen image of textiles coated by **blue Ir@SiO$_2$** system (a) and **red Ir@SiO$_2$** system (b).

Washing fastness

Coating adhesion and washing fastness were evaluated by exposing the textiles to washing tests in dynamic and static conditions[5], with the intent to reproduce the fabrics behavior during washing and in use stages. The washing fastness tests followed a constant methodology for ICP-OES analysis. The obtained values are negligible both in static and dynamic condition, reaching at most some units per cent for all the systems, without any detectable release of Ir(III) complexes (Figure 3.1.13 and in Table S1.1-S1.2 Appendix 1)[44]. In particular dynamic tests results showed no significant variation in the behavior of silica or **Ir@SiO$_2$** coatings as to washing fastness, giving similar values of total silica weight loss (ca. 2%). After 4 days in static conditions, silica release flattened out, stabilizing at ca. 1.5% weight loss. These results indicate strong adhesion of the coating and good embedding of the Ir(III) complexes into the SiO_2 matrix, which also promote a strong interaction with the fibers.

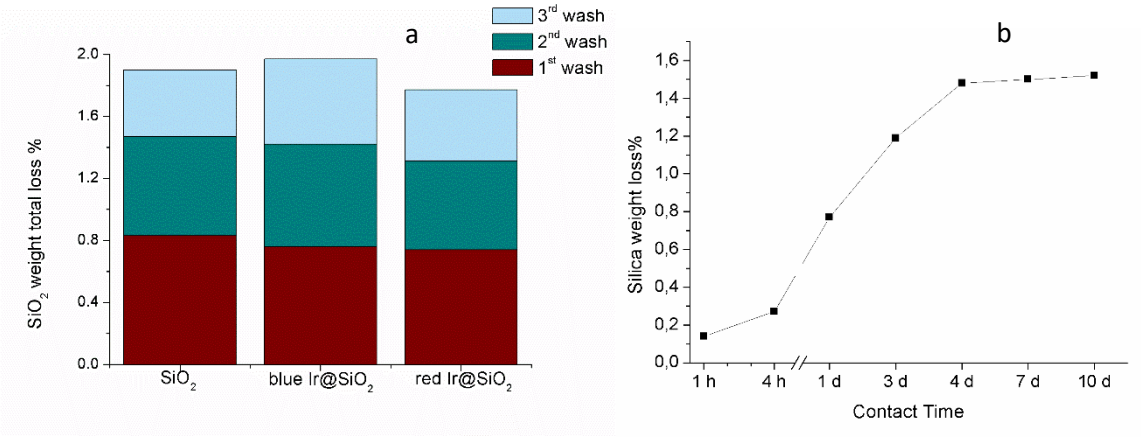

Figure 3.1.13: Percentage of SiO_2 lost during release tests both in dynamic condition (a) and in static condition (b) for textiles coated by three-layer of **blue Ir@SiO_2 system** (referred as silica weight loss% in function of time).

Antibacterial properties

The antibacterial properties of Ir(III)-based luminescent textiles was compared to those displayed by $[F_2IrPTZ\text{-}Me]^+$ and $[IrQTZ\text{-}Me]^+$ alone against Gram(-) *Escherichia coli* and Gram(+) *Deinococcus radiodurans*. As previously reported, both of the cationic Ir(III) tetrazole derivatives promoted excellent antimicrobial activity toward Gram positive *Deinococcus radiodurans* presenting a minimum inhibitory concentration (MIC) of 1 μg mL^{-1} for $[F_2IrPTZ\text{-}Me]^+$, 4 μg mL^{-1} for $[IrQTZ\text{-}Me]^+$, while no antibacterial activity was observed for *E. coli* cultures[1]. According to the procedure reported in the antibacterial activity assessment of textile materials – Parallel Steak Method (AATCC 147, modified), the antibacterial activity was tested of coated textiles in direct contact with agar cultures[36]. This test was chosen as a qualitative method to compare any differences in their antibacterial strength between Ir(III) complexes alone and Ir(III) complexes embedded inside the silica coatings. After an incubation phase of 24h at 30°C, three different exposure conditions were analyzed: dark, natural light and UV + natural light. Bacterial inhibition is usually associated with an alteration of the parallel streaks marked out on the agar plates corresponding to bacterial colonies. Unlike results reported by Fiorini et al. (2017)[1], once, both $[F_2IrPTZ\text{-}Me]^+$ and $[IrQTZ\text{-}Me]^+$ complexes encapsulated within ceramic silica coating and exposed to visible light displayed antimicrobial activity against *E. coli* cultures. Indeed, *E. coli* growth was inhibited by both blue and red **Ir@SiO_2** to a comparable extent (blue **Ir@SiO_2** shown in Figure 3.1.14, while for red **Ir@SiO_2** agar plates are shown in Figure S1.8 Appendix 1). *E. coli* growth inhibition was observed on the coated textiles once exposed to natural light and UV + natural light, while no alteration of the streaks is observed for samples left in darkness. This results might suggest a photo-induced antibacterial activity of the Ir(III) triplet emitters (^3T) once

stabilized by silica, an effect that can be correlated with the production of singlet oxygen ($^1O_2$) that - together with other ROS - might be potentially toxic for bacteria[45,46]. This qualitative response paves the way to further hypothesis about the driving mechanism causing the antibacterial activity displayed by **Ir@SiO₂** systems, in which the strong interaction between silica matrix and complex probably plays a key role.

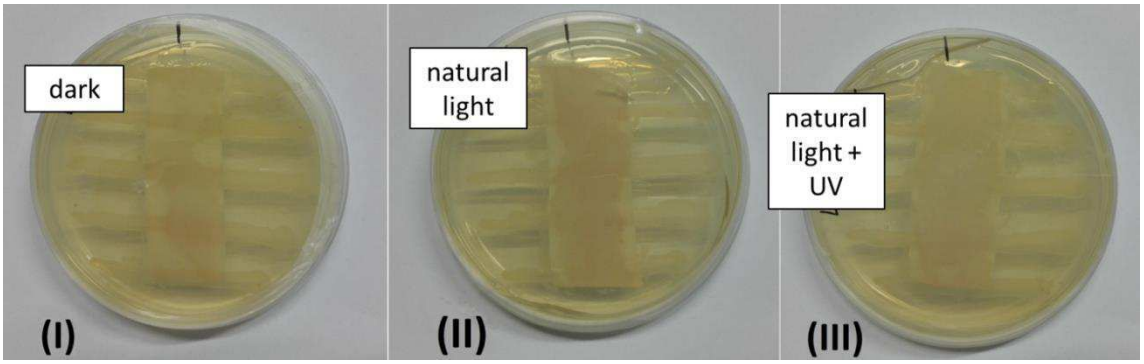

Figure 3.1.14: Image of AATCC 147 tests on blue Ir@SiO_2 coated textiles in the dark (I) and under natural light (II) and natural light + UV (III) conditions.

Wearable-release – in-vitro test

With the aim of investigating the coated textiles behaviour during their usage, we evaluated **Ir@SiO₂** NPs release in static condition under exposure to synthetic sweat[47], mimicking the conditions of sweaty fabric in contact with the human skin, and evaluating any possible release of the final material when wearied. We performed 24-hour release tests in static condition at 32°C, the typical external temperature of human skin[48]. After ICP-OES evaluation, we observed a very low release of SiO_2 and an Ir signal either below or close to the instrumentation limit of detection (LOD) (Table 3.1.5), a negligible value compared with the total amount of coating.

Table 3.1.5: Release values in synthetic sweat of **Ir@SiO₂** coated fabric after 24 hours in static condition at 32°C.

	Ir (mg L^{-1})	**Si (mg L^{-1})**	**Weight loss of SiO_2 %**
Ir@SiO_2 NPs	0.01 ± 0.01	7.92 ± 0.16	0.95 ± 0.01

Taking advantage of the Franz cell *ex-vivo* model, trans-dermal diffusion of **Ir@SiO₂** NPs was evaluated. This choice was made in order to enhance skin exposure by putting it in direct contact with the Ir(III) nanosols instead of sweaty fabric, which showed such a low release of NPs. After 24h of exposure to **Ir@SiO₂** NPs, no trans-dermal diffusion was observed to occur as

confirmed by ICP-MS analysis, which showed no detectable amounts of Ir inside the receiving phases (LOD for Ir^{193} = 0.010 µg L^{-1}). By means of separation of the skin into its epidermic and dermal components, epidermal ad dermal NPs penetration could be evaluated. Analyses detected little penetration of Ir into the dermis, while the amount detected within the epidermis was found to be higher because epidermis acts as the main barrier[49,50]. Typically, the amount of toxic agents detected in the epidermis displays a high variance due to specific donor skin characteristics, such as number of hair bulbs and thickness (Figure 3.1.15).

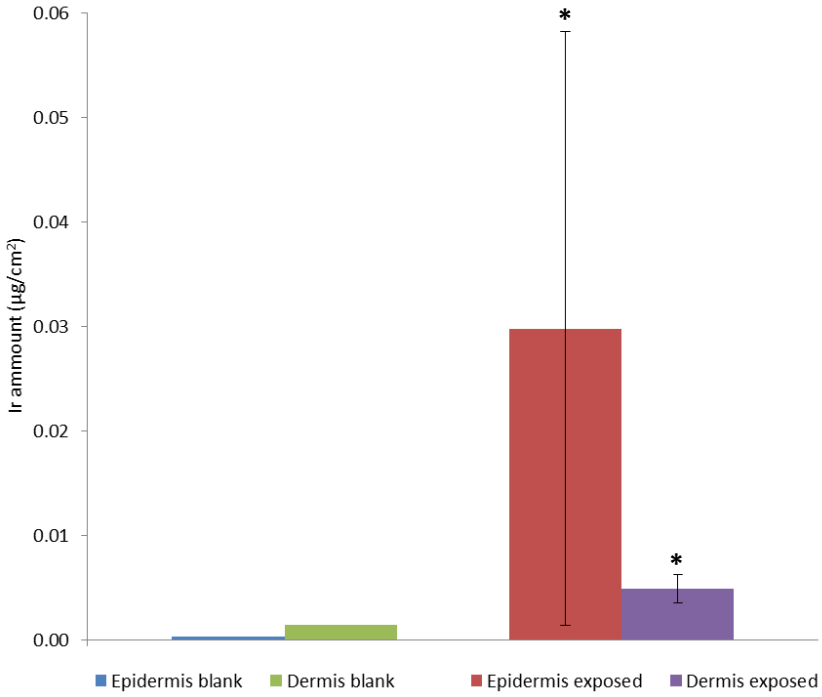

Figure 3.1.15: Ir distribution within human skin in blank and treated samples as determined by ICP-MS. (*: values are significant different from the blank with $p < 0.05$)

The **Ir@SiO₂** NPs distribution on the epidermal surface was then mapped with 2p-fluorescence microscopy, to better investigate skin surface distribution. Moreover, with the use of a 620 ± 52 nm bandpass filter this technique enhances Ir(III)-based emission by cutting the emission from the first skin layer, thus collecting only the signal due to NPs. Observing skin samples before and after NPs exposure (Figure 3.1.16), we noticed the presence of light dots in the treated sample. A closer z-stack images analyses obtained by acquiring the first 50 µm layers in thickness (Figure 3.1.17), revealed luminescent dots that can be associated to the external part of hair channels, having dimensions about 20 µm in diameter. Images seem to confirm the behaviour reported in literature for silica NPs with diameter lower than 45 nm[49]. Particularly, **Ir@SiO₂** NPs hypothetically released by the textile are stopped in the first skin layers, moving to

the hair bulbs and crowding around them, without any strong damage of the inner skin layers and tissues underneath.

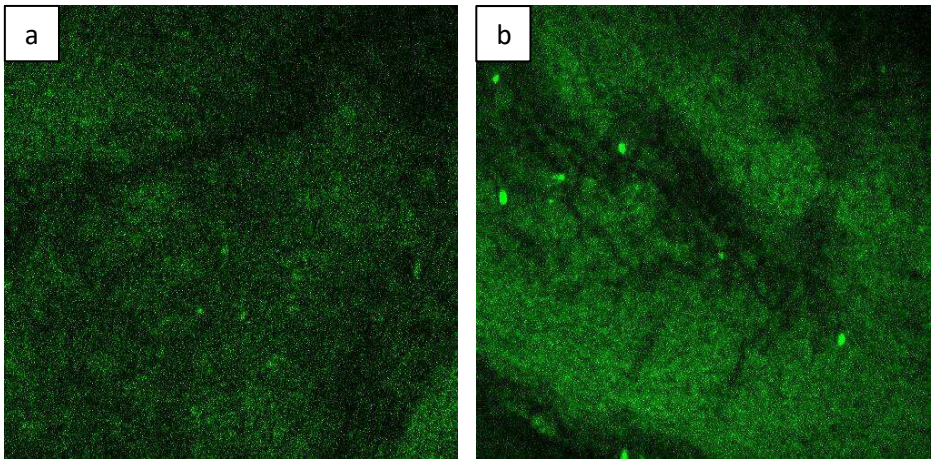

Figure 3.1.16: Superficial images made using a 2p-Fluorescence Microscope of skin sample (a) before **Ir@SiO$_2$** NPs exposure and (b) after 24 hours of exposure. Image size is 500µm×500 µm.

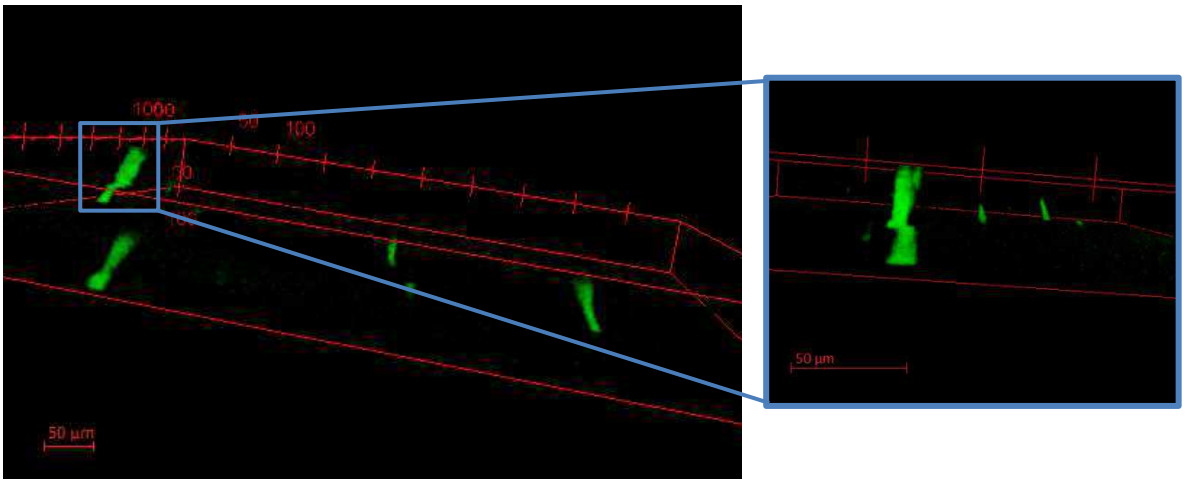

Figure 3.1.17: Tomography images made using a 2p-Fluorescence Microscope of skin sample (1 mm*1 mm*50 µm) after 24 hours of exposure to **Ir@SiO$_2$** NPs.

However, in order to reach an optimal risk assessment and management, it's necessary to identify the real exposure conditions of the fabrics coated with **Ir@SiO$_2$** systems.

For both $[F_2IrPTZ\text{-}Me]^+$ and $[IrQTZ\text{-}Me]^+$ cationic complexes we consider 21 µM (15 µg mL^{-1}) and 23 µM (15 µg mL^{-1}), respectively, to be the maximum possible exposure. This estimate is based on the consideration that in the case of direct contact with Ir complexes aided by skin/fabric friction in the presence of sweat, the entire amount of complex embedded in the 3%wt **Ir@SiO$_2$** systems (3 g L^{-1} of Ir@SiO_2) can be freed and made available for cell uptake. The

w/w ratio between Ir(III) complex and SiO_2 nanosol being 1:1000, dispersion in synthetic sweat (dilution of 1:2) gives a 15 µg mL^{-1} maximum concentration of complex.

Although the half maximal inhibitory concentration (IC_{50}) values are not available for $[F_2IrPTZ\text{-}Me]^+$ and $[IrQTZ\text{-}Me]^+$ for keratocyte cell line, i.e. the cell line used as a model for human skin, we can consider IC_{50} of other Ir(III) complexes belonging to the same organometallic class reported in the literature, having IC_{50} values in the range of 2-10 µM[51,52,53].

As demonstrated above in the washing fastness section, quite low a release of **Ir@SiO₂** from textiles was detected. So, the only risk could be associated to the **Ir@SiO₂** nanosol, and - as proved by the Franz cell test - we did not observe any trans-dermal migration for both **Ir@SiO₂** systems, which stop in the first layers of the human skin. In fact, based on the permeation values assessed by ICP-OES, epidermis and dermis are able to stop over 99% of Ir due to crowding around hair bulbs. Therefore even assuming the maximum possible release under friction-aided conditions, with all of the Ir(III) tetrazolate complexes free and available, the final short-term exposure should be much lower than the average IC_{50} values (2-10 µM) reported in the literature. In conclusion, our final biological target, i.e. the keratocyte cell line, presents a very low exposure risk to Ir(III) tetrazolate complexes, whose concentration in the skin should be negligible. However, more long-term exposure and cytotoxicity tests will be needed for achieving the safe industrial production and use of **Ir@SiO₂** coated textiles.

Conclusions

In the present work, we produced two new types of **Ir@SiO₂** NPs based textile coatings, displaying very promising self-marking and antibacterial properties. The strong interaction between Ir complexes and silica nanoparticles gives these systems the ability to be easily detected under UV light, both when used as coating for textiles and after release in the environment. The obtained textiles present a homogeneous distribution of the luminescent coating, whose mechanical and chemical resistance can be evaluated, simply tracking the luminescence of deposited and released NPs. In addition, preliminary antibacterial testing shows interesting antimicrobial properties against both Gram(+) (*Deinococcus radiodurans*) and Gram(-) (*Escherichia coli*), probably due to the known production of light-induced reactive oxygen species. Finally, the stable optical properties shown by Ir@SiO_2 NPs, make them ideal candidates to track the presence of NPs in different biological matrices, providing useful information for the assessment of the potential risk arising from dermal exposure to NPs.

Acknowledgements

This project has benefited from the EU-H2020 research program under grant agreement no. 654360 and has benefited from the access provided by the Fundacio Institut Catala` de Nanocie`ncia y Nanotecnologia – ICN2 – Barcelona (Spain) and the Foundation for Research and Technology Hellas – FORTH – Heraklion (Greece) within the framework of the NFFA-Europe TransnationalAccess Activity.

References

1. Fiorini, V. *et al.* Methylation of Ir(III)-tetrazolato complexes: an effective route to modulate the emission outputs and to switch to antimicrobial properties. *Dalt. Trans.* **46**, 12328 (2017).

2. Zanoni, I. *et al.* Encapsulation of cationic iridium(III) tetrazole complexes into a silica matrix: synthesis, characterization and optical properties. *New J. Chem.* (2018). doi:10.1039/C8NJ01514G

3. Radetic, M. Functionalization of textile materials with TiO2 nanoparticles. *J. Photochem. Photobiol. C Photochem. Rev.* **16**, 62–76 (2013).

4. Ortelli, S., Costa, A. L. & Dondi, M. TiO2 nanosols applied directly on textiles using different purification treatments. *Materials (Basel).* **8**, 7988–7996 (2015).

5. Klein, C. L. *et al. NM-Series of Representative Manufactured Nanomaterials, NM-300 Silver Characterisation, Stability, Homogeneity*. (2011). doi:10.2788/23079

6. Perelshtein, I. *et al.* CuO-cotton nanocomposite: Formation, morphology, and antibacterial activity. *Surf. Coatings Technol.* **204**, 54–57 (2009).

7. Pinto, T. V. *et al.* Screen-Printed Photochromic Textiles through New Inks Based on SiO2@naphthopyran Nanoparticles. *ACS Appl. Mater. Interfaces* **8**, 28935–28945 (2016).

8. Alongi, J., Carosio, F. & Malucelli, G. Current emerging techniques to impart flame retardancy to fabrics: An overview. *Polym. Degrad. Stab.* **106**, 138–149 (2014).

9. Ortelli, S. *et al.* Coatings made of proteins adsorbed on TiO2 nanoparticles: a new flame retardant approach for cotton fabrics. *Cellulose* (2018). doi:10.1007/s10570-018-1745-z

10. Ortelli, S., Malucelli, G., Blosi, M., Zanoni, I. & Costa, A. L. NanoTiO2@DNA complex: a novel eco, durable, fire retardant design strategy for cotton textiles. *J. Colloid Interface Sci.* **546**, 174–183 (2019).

11. Rivero, P. J., Urrutia, A., Goicoechea, J. & Arregui, F. J. Nanomaterials for Functional Textiles and Fibers. *Nanoscale Res. Lett.* **10**, 1–22 (2015).

12. McGillicuddy, E. *et al.* Silver nanoparticles in the environment: Sources, detection and ecotoxicology. *Sci. Total Environ.* **575**, 231–246 (2017).

13. LI, J., ZHAO, Y., GE, M., FU, S. & LIN, T. Superhydrophobic and luminescent cotton fabrics prepared by dip-coating of APTMS modified SrAl2O4:Eu2+,Dy3+particles in the presence of SU8 and fluorinated alkyl silane. *J. Rare Earths* **34**, 653–660 (2016).

14. Titos-Padilla, S. *et al.* Photophysical properties of [Ir(tpy)2]3+-doped silica nanoparticles and synthesis of a colour-tunable material based on an Ir(core)–Eu(shell) derivative. *J. Mater. Chem. C* **1**, 3808 (2013).

15. Ow, H. *et al.* Bright and stable core-shell fluorescent silica nanoparticles. *Nano Lett.* **5**, 113–117 (2005).

16. Santra, S., Zhang, P., Wang, K., Tapec, R. & Tan, W. Conjugation of biomolecules with luminophore-doped silica nanoparticles for photostable biomarkers. *Anal. Chem.* **73**, 4988–4993 (2001).

17. W. R. Grace & Co.-Conn. LUDOX® Colloidal Silica in Coatings. *Grace Davison Eng. Mater.* (2007).

18. Fiorini, V. *et al.* Fully Ir(III) tetrazolate soft salts: the road to white-emitting ion pairs. *Dalt. Trans.* **45**, 3256–3259 (2016).

19. Monti, F. *et al.* Iridium(III) complexes with phenyl-tetrazoles as cyclometalating ligands. *Inorg. Chem.* **53**, 7709–7721 (2014).

20. Caporale, C. *et al.* Investigating Intracellular Localisation and Cytotoxicity Trends for Neutral and Cationic Iridium Tetrazolato Complexes in Live Cells. *Chem. - A Eur. J.* **23**, 15666–15679 (2017).

21. Kumar, S. V. *et al.* Antimicrobial Properties of Tris(homoleptic) Ruthenium(II) 2-Pyridyl-1,2,3-triazole 'click' Complexes against Pathogenic Bacteria, Including Methicillin-Resistant Staphylococcus aureus (MRSA). *Inorg. Chem.* **55**, 9767–9777 (2016).

22. Li, F., Collins, J. G. & Keene, F. R. Ruthenium complexes as antimicrobial agents. *Chem. Soc. Rev.* **44**, 2529–2542 (2015).

23. Lu, L. *et al.* Identification of an iridium(III) complex with anti-bacterial and anti-cancer activity. *Sci. Rep.* **5**, 14544 (2015).

24. Zheng, X. *et al.* Tracking Cancer Metastasis In Vivo by Using an Iridium-Based Hypoxia-Activated Optical Oxygen Nanosensor. *Angew. Chemie Int. Ed.* **54**, 8094–8099 (2015).

25. Zheng, X. *et al.* Hypoxia-specific ultrasensitive detection of tumours and cancer cells in vivo. *Nat. Commun.* **6**, 5834 (2015).

26. Yellol, J. *et al.* Highly potent extranuclear-targeted luminescent iridium(iii) antitumor agents containing benzimidazole-based ligands with a handle for functionalization. *Chem. Commun.* **52**, 14165–14168 (2016).

27. Zhang, L. *et al.* AIE Multinuclear Ir(III) Complexes for Biocompatible Organic Nanoparticles with Highly Enhanced Photodynamic Performance. *Adv. Sci.* **6**, 1802050 (2019).

28. Zhang, W.-Y. *et al.* Evaluation of anticancer effect in vitro and in vivo of iridium(III) complexes on gastric carcinoma SGC-7901 cells. *Eur. J. Med. Chem.* **178**, 401–416 (2019).

29. Ma, D.-L., Wu, C., Wu, K.-J. & Leung, C.-H. Iridium(III) Complexes Targeting Apoptotic Cell Death in Cancer Cells. *Molecules* **24**, (2019).

30. Ma, D.-L. *et al.* Recent advances in iridium(iii) complex-assisted nanomaterials for biological applications. *J. Mater. Chem. B* **6**, 537–544 (2018).

31. Butler, R. N. *Tetrazoles. In "Comprehensive Heterocyclic Chemistry II"; Storr, R. C., Ed.; Pergamon Press: Oxford, U.K., Vol. 4, 621-678, and references cited therein.* (1996).

32. Koguro, K., Oga, T., Mitsui, S. & Orita, R. Novel Synthesis of 5-Substituted Tetrazoles from Nitriles. *Synthesis (Stuttg).* **1998**, 910–914 (1998).

33. Crosby, G. A. & Demas, J. N. Measurement of photoluminescence quantum yields. Review. *J. Phys. Chem.* **75**, 991–1024 (1971).

34. Nakamaru, K. Synthesis, Luminescence Quantum Yields, and Lifetimes of Trischelated Ruthenium(II) Mixed-ligand Complexes Including 3,3'-Dimethyl-2,2'-bipyridyl. *Bull. Chem. Soc. Jpn.* **55**, 2697–2705 (1982).

35. Psilodimitrakopoulos, S. *et al.* Ultrahigh-resolution nonlinear optical imaging of the armchair orientation in 2D transition metal dichalcogenides. *Light Sci. Appl.* **7**, 18005–18009 (2018).

36. Toray Textiles Europe Ltd. Crown Farm Way. *Antibacterial Activity Assessment of Textile Materials – Parallel Steak Method (AATCC 147 modified) procedure*. (2006).

37. Franz, T. J. Percutaneous Absorption. On the Relevance of in Vitro Data. *J. Invest. Dermatol.* **64**, 190–195 (1975).

38. Guth, K., Schäfer-Korting, M., Fabian, E., Landsiedel, R. & van Ravenzwaay, B. Suitability of skin integrity tests for dermal absorption studies in vitro. *Toxicol. Vitr.* **29**, 113–123 (2015).

39. Crosera, M. *et al.* In vitro permeation of palladium powders through intact and damaged human skin. *Toxicol. Lett.* **287**, 108–112 (2018).

40. Tiki, A., Amin, A. & Kanwal, A. Chemistry of optical brighteners and uses in textile industries. *Pakistan Text. J.* **59**, 42–43 (2010).

41. Stagni, S. *et al.* Essential Role of the Ancillary Ligand in the Color Tuning of Iridium Tetrazolate Complexes. *Inorg. Chem.* **47**, 10509–10521 (2008).

42. Flamigni, L., Barbieri, A., Sabatini, C., Ventura, B. & Barigelletti, F. *Topics in Current Chemistry, Biochemistry*. *Bioelectrochemistry and Bioenergetics* **281**, (2007).

43. Werrett, M. V *et al.* Synthesis, Structural, and Photophysical Investigation of Diimine Triscarbonyl Re(I) Tetrazolato Complexes. *Inorg. Chem.* **50**, 1229–1241 (2011).

44. Kartini, I., Ilmi, I., Kunarti, E. S. & Kamariah. Wash fastness improvement of malachite green-dyed cotton fabrics coated with nanosol composites of silica - Titania. *Bull. Mater. Sci.* **37**, 1419–1426 (2014).

45. Takizawa, S., Aboshi, R. & Murata, S. Photooxidation of 1,5-dihydroxynaphthalene with iridium complexes as singlet oxygen sensitizers. *Photochem. Photobiol. Sci.* **10**, 895 (2011).

46. Gao, R. *et al.* Bis-cyclometalated Ir(III) complexes as efficient singlet oxygen sensitizers. *J. Am. Chem. Soc.* **124**, 14828–14829 (2002).

47. Von Goetz, N. *et al.* Migration of Ag- and TiO2-(nano)particles from textiles into artificial sweat under physical stress: Experiments and exposure modeling. *Environ. Sci. Technol.* **47**, 9979–9987 (2013).

48. Monteiro-Riviere, N. A. & Baroli, B. *Toxicology of the Skin*. (2010).

49. Larese Filon, F., Mauro, M., Adami, G., Bovenzi, M. & Crosera, M. Nanoparticles skin absorption: New aspects for a safety profile evaluation. *Regul. Toxicol. Pharmacol.* **72**, 310–322 (2015).

50. Crosera, M. *et al.* Nanoparticle dermal absorption and toxicity: A review of the literature. *Int. Arch. Occup. Environ. Health* **82**, 1043–1055 (2009).

51. Lau, J. S. *et al.* Luminescent Cyclometalated Iridium (III) Polypyridine Indole Properties , Cytotoxicity , and Cellular Uptake. **48**, 708–718 (2009).

52. Lee, P. K., Law, W. H. T., Liu, H. W. & Lo, K. K. W. Luminescent cyclometalated iridium(III) polypyridine Di-2-picolylamine complexes: Synthesis, photophysics, electrochemistry, cation binding, cellular internalization, and cytotoxic activity. *Inorg. Chem.* **50**, 8570–8579 (2011).

53. Lee, P.-K., Liu, H.-W., Yiu, S.-M., Louie, M.-W. & and Kam-Wing Lo, K. Luminescent cyclometallated iridium(III) bis(quinolylbenzaldehyde) diimine complexes—synthesis, photophysics, electrochemistry, protein cross-linking properties, cytotoxicity and cellular uptake. *Dalt. Trans.* **40**, 2180–2189 (2011).

3.3.2 CuO nanoparticles penetration through intact and damaged human skin

Source (publiched paper): "CuO nanoparticles penetration through intact and damaged human skin". I. Zanoni, M. Crosera, S. Ortelli, M. Blosi, G. Adami, F. Larese Filon, A. L. Costa, New Journal of Chemistry, Advance Article[1].

Introduction

Since the manufacture and use of NPs are increasing in the market, humans are more likely to be exposed within occupational, consumer or environmental scenarios. The skin is the largest organ of the body, accounting for more than 10% of body mass[2], forming, as a consequence, a great area over which intentional and unintentional exposure to chemicals (in form of particles, cosmetics, clothing, handling products) can occur[3,4]. NPs skin absorption is an issue which the scientific community has been addressing, for the concerns over the hazard that transdermal flux of NPs can generate[5]. However, so far there are still many knowledge gaps in order to fully understand origin, properties and fate of NPs that cause adverse effects to biological targets[6].

The impact of metal oxide NPs on human health and environment has been deeply investigated because they possess potential safety concerns to humans, animals as well as aquatic biota[7,8,9,10,11]. The increased interest for copper oxide nanoparticles (CuO NPs) is due to their unique, electrical, catalytic, optical and magnetic properties that make them the ideal candidate for the development of supercapacitors, near-infrared filters, magnetic storage media, sensors, catalysts, semiconductors, etc...[12]. In addition, their great antimicrobial action, against a wide range of pathogens and also drug resistant bacteria, have led to the development of various applications in the biomedical field (wound dressings, modified textiles, skin cream)[13]. Several in vitro studies have provided evidence that CuO NPs are particularly powerful in comparison to other metal oxides in terms of triggering cytotoxicity and genotoxicity[7,14,15,16,17,18]. CuO NPs toxicity on fish is well documented[19,20], even few data are available on other animals and no data are available on exposed workers. Gosens et al. in 2016 assessed organ burden and pulmonary toxicity in rats exposed by inhalation route to CuO NPs, finding the development of acute lung inflammation and cellular damage for 5 days with a resolution of alterations after 3

weeks[21]. The study permitted to obtain data useful for risk assessment. Costa et al. in 2018 confirmed that inhalation of CuO NPs in rats' (3.3 mg cm^{-1} to 13.2 mg cm^{-1}) cause upregulation of the oncoprotein ECT2 and the chemokine CCL2 and other proinflammatory markers as well as proliferation in bronchoalveolar epithelium after a short-term inhalation exposure[22]. Anreddy et al. (2018) studied toxicity of CuO in rats after administration of 5 and 50 mg kg^{-1} per body weight day^{-1} for 14 days, finding a significant dose dependent alterations in antioxidant enzyme activities[23]. The resulting data showed a significant decrease in Glutathione level, Catalase and superoxide dismutase activity, and the increase of the lipid peroxidation product (MDA) levels, confirming the capability of NPs to induce oxidative stress, inflammation, and consequent damage to proteins, membranes, and DNA[24,25]. Cathe et al. (2017) studied keratinocyte HaCaTcells exposed to CuO NPs finding an increase of ROS production when exposed to 5 and 25 µg mL^{-1} of NPs in a dose related matter[26]. For this reason, the importance to test the toxic action of CuO NPs toward humans is particularly clear, with a special focus to skin penetration route of entry. However, very few studies are focused on the effects of ENMs and in particular of CuO on human skin biological target[27,28] and the outcomes of these toxicity studies are insufficient to draw conclusions about the specific mechanisms of trans-dermally exposure to CuO NPs[29,30]. At this purpose a systematic characterisation of physicochemical properties and the estimation of the released toxicant Cu^{2+} ions is fundamental[31], together with the investigation of penetration and permeation pathways. Therefore, in this study we characterised CuO NPs dispersions in synthetic sweat, in order to capture the surface modification occurring in relevant exposure medium and investigated the *in-vitro* penetration and permeation of CuO NPs into human skin, by using Franz cell *in-vitro* model[32].

Experimental part

Materials. Commercial CuO nano-powder (declared average particle diameter: 12 ± 4 nm) was provided by PlasmaChem GmbH (Germany) and used as reference materials during European Project 'SUN' (EC-GA No.604305). Nitric acid 70% (redistilled, 99.99% trace metal basis) and all inorganic salts were of analytical grade and purchased from Sigma-Aldrich (St. Louis, MI, USA). Human skin derived from surgical waste from Clinical University Department of Medical and Surgical Medical Sciences of Trieste.

Preparation of nanoparticles suspension. A CuO stock suspension at a concentration of 10 g L^{-1} of Cu (1 wt%) was prepared by dispersing CuO powder in phosphate-buffered saline (PBS) medium (total phosphate concentration: 0.05 M, pH = 7.4) and ball milling the resulting suspension with Ø 3 mm zirconia spheres, over 95 h.

Intrinsic properties. Morphological characterization of CuO NPs was performed by field emission-scanning electron microscopy (FE-SEM) instrument (Carl Zeiss Sigma NTS Gmbh, Oberkochen, DE), coupled with scanning transmission electron microscopy (STEM) detector. One drop of the CuO stock suspension diluted in MilliQ water (100 µg mL^{-1}) was deposited on a film-coated copper grid and then dried in air. Image analysis was performed on more than 50 particles to estimate the average diameter of particles. Colloidal characterization (pH, d_{DLS} and ζ-pot_{ELS}) was performed on samples diluted in synthetic sweat (100 µg mL^{-1}), making 3 consecutive analyses on 3 different batch dispersions. Samples were exposed to synthetic sweat at 32°C (mean skin temperature), collecting data after 1h and 24h. The hydrodynamic diameter was determined by dynamic light scattering (DLS) and Zeta potential (ZP - ζ-pot_{ELS}) by electrophoretic light scattering (ELS), both performed using a Zetasizer nano ZSP (model ZEN5600, Malvern Instruments, UK). The Smoluchowski equation was applied to convert the electrophoretic mobility to zeta potential.

Preparation of media. As relevant media, we used a solution of synthetic sweat at 0.5%wt NaCl, 0.1%wt Lactic Acid and 0.1%wt Urea, corrected to pH 4.5 with Ammonium Hydroxide 1N.

System-dependent properties. The quantification of copper ions dissolved in synthetic sweat was performed by centrifuging 15 mL of 100 µg mL^{-1} suspension at 5000 rpm and a spin time of 30 min, using an ultra-centrifugal filter (UCF) unit (Amicon Ultra-15, 10 kDa, Millipore). The filtered solution (10 mL) was analyzed by inductively coupled plasma optical emission spectrometry using an ICP-OES 5100 – vertical dual view apparatus (Agilent Technologies, Santa Clara, CA, USA). The total copper (CuO NPs + Cu^{2+}) was quantified and used to normalized the rate Cu^{2+}/Cu_{total} in each diluted suspension, which was previously treated adding 10% vol/vol of ultrapure HNO_3 to ensure complete digestion. Cu^{2+} ion release was calculated as the ratio between the dissolved copper ions from ultrafiltration and the total copper presents in copper oxide suspension[31]. In order to perform tests on Cu^{2+} ions, we applied to the *in-vitro* model the ultrafiltrated solutions coming from three different aliquots of CuO dispersed in synthetic sweat (100 µg mL^{-1}) after 1 h of exposure time. The ultrafiltered solutions put in contact with the model had a total ionic concentration of 30 µg mL^{-1}.

Preparation of skin membranes. Human abdominal full thickness skin was obtained as surgical waste. Prior to freezing, subcutaneous fat was removed and hair shaved. All the pieces of full thickness skin were stored in freezer at −25 °C for a period up to, but not exceeding, 4 months. It has been shown that this method of storage does not damage the skin since no

difference in permeability was observed between fresh and frozen segments of the same skin in a separate series of experiments[32]. Skin integrity was tested before and after each experiment using electrical conductibility by means of a conductometer (Metrohm, 660, Metrohm AG Oberdorfstr. 68 CH-9100 Herisau) operating at 300 Hz connected to two stainless steel electrodes[33]. The conductibility data, obtained in μS, were converted in KΩ cm^{-2}. Cells with a resistance lower than 3.95 ± 0.27 KΩ cm^{-2}, were considered to be damaged[34]. Damaged sample skin was obtain following the Bronaugh and Steward protocol[35]. The use of surgical waste skin was approved by the Ethical Committee of Ospedali Riuniti di Trieste (Resolution of the Ethics Committee of Ospedali Riuniti di Trieste No. 298, 3 August 2007). The Ethical Committee of Ospedali Riuniti di Trieste approved the study no. 298/2007 and each donor signed an informed consent.

In-vitro diffusion system. Percutaneous absorption studies were performed using static diffusion cells following the Franz Method (1975). The receptor compartment has a mean volume of 4.5 mL and was maintained at 32°C by means of circulation of thermostated water in the jacket surrounding the cell. This temperature value has been chosen in order to reproduce the hand's physiological temperature at normal conditions. The concentration of the salt in the receptor fluid is approximately the same that can be found in the blood. The solution in each cell was continuously stirred using a Teflon coated magnetic stirrer. Each piece of skin was clamped between the donor and the receptor compartment; the mean exposed skin area was 0.95 cm^2 and the average membranes thickness was 1 mm. The experiments were performed as follows.

At time 0, the exposure chambers of three Franz diffusion cells were filled with 0.11 mg cm^{-2} of CuO NPs solution dispersed in PBS (conc. 10 g L^{-1}) and diluted 1:100 with synthetic sweat at pH 4.5 to reproduce in vivo condition (1 mL solution). At selected intervals (4, 8, 12,16, 20, 24 h) 1.5 mL of the dermal bathing solution was removed and analysed at ICP-MS. Each receptor sample was immediately replaced with an equal volume of fresh physiological solution.

Skin permeation experiments on abraded skin were conducted following the same procedure. The skin was prepared following the protocol reported by Bronaugh and Steward (1985): skin was abraded by drawing the point of a 19-gauge hypodermic needle across the surface (6 marks in one direction and 6 perpendiculars). For each experiment, one cell was added as blank. The blank cells have been treated as the other cells with the exception that only synthetic sweat, without NPs, was used in the donor compartment. In order to evaluate the contribute of free ions to the penetration/permeation process we applied the same rationale

used for NPs exposure to the ultrafiltered solutions extracted after 1h of exposure in synthetic sweat (ionic concentration 30 μg mL^{-1}). Each experiment has been repeated two times, in order to use the skin of four different donors, for a total of 6 cells with intact skin, 6 cells with damaged skin, and 4 blank cells.

Analytical Measurements. ICP-MS Nexion 350X with an ESI autosampler, (Perkin Elmer, USA instrument) was used to determinate total Cu concentration in the receiver phases. A five-points standard curve, obtained by dilution of Cu standard solution for ICP-MS analyses (by Sigma Aldrich, Milan, Italy), was used for ICP-MS measurements (0.01 - 10, μg L^{-1}, ion mass 65 u.m.a.). The analysis was carried out in kinetic energy discrimination (KED) mode using ultra-high purity helium (flow rate of 4.8 mL min^{-1}) to minimize polyatomic interferences. The limit of detection of Cu was 0.05 μg L^{-1} for ICP-MS and the precision of the measurements as repeatability (RSD %) for the analysis was <5%. Total Cu concentration in donor phases and in the solutions resulting from the mineralization of the skin samples were performed by ICP-OES using an Optima 8000 Spectrometer (PerkinElmer, U.S.A.), equipped with an S10 Autosampler. Analysis were conducted using a calibration curve obtained by dilution (range: 0 - 10 μg mL^{-1}) of Cu standard solution for ICP-OES analyses (by Sigma Aldrich, Milan, Italy). The limit of detection (LOD) at the operative wavelength of 324.754 nm was 0.01 μg mL^{-1}. The precision of the measurements expressed as relative standard deviation (RSD %) for the analysis was always less than 5%.

Statistical Analysis. Cu concentration data (μg cm^{-3}) in the receptor solution were converted to the Cu amount that penetrated per skin surface unit (μg cm^{-2}). Data analysis was performed with Excel for Windows, release 2007 and Stata Software, version 11.0 (StataCorp LP, College Station, TX, USA). Skin absorption data were reported as mean ± standard deviation (SD). The difference among independent data was assessed by means of the Mann-Whitney test. A p value < 0.05 was considered significant.

Results and Discussion

Intrinsic and system-dependent properties

The morphological characterization of CuO NPs is reported in Figure 3.2.1. The images collected by FE-SEM (Fig. 3.2.1a) and STEM (Fig. 3.2.1b) well show the marked aggregation degree of the particles probably deriving from the high temperature treatment undergone during the synthesis process (≈350°C). The magnified STEM image (Fig. 3.2.1c) reveals the primary NPs, spherical shaped, with an average diameter of 12 ± 8 nm, consistent with the

supplier specification. The highly aggregated behaviour of CuO NPs dispersed in MilliQ has been confirmed in the previous study by Ortelli et al. (2017)[31], reporting a large hydrodynamic diameter (d_{DLS}): 1093 ± 50 nm, coupled with a low negative zeta potential (ζ-pot_{ELS}): −9.1 ± 0.4 mV, which did not provide the necessary electrostatic stabilisation to ensure the colloidal stability.

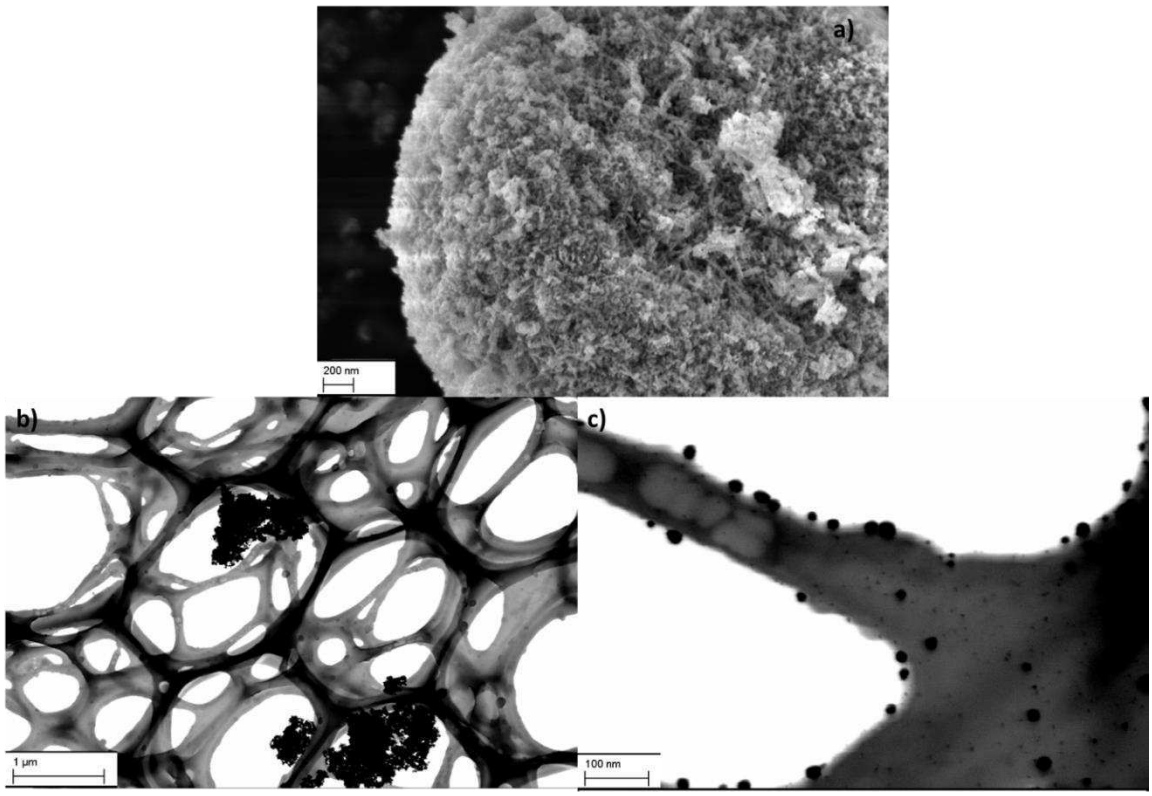

Figure 3.2.1: a) FE-SEM, b) and c) STEM images of CuO NPs dispersed in Milli-Q water (concentration 100 µg mL^{-1}).

The agglomeration behaviour of CuO NPs in MilliQ has been compared with the assessed values of d_{DLS} and ζ-pot_{ELS}, after dispersion in synthetic sweat, to better mimicking the real transdermal exposure conditions. The results, together with data on static dissolution, measured after 1 and 24h of exposure are shown in Table 3.2.1.

Table 3.2.1: d_{DLS} and ζ-pot_{ELS} and static dissolution (Cu ionic fraction) of CuO NPs dispersed in synthetic sweat (100 µg mL^{-1}).

	pH	**d_{DLS} (nm)**	**ζ-pot_{ELS} (mV)**	***Cu (ionic) µg mL^{-1}***	***Cu_{ionic}/Cu_{total} weight ratio %****
After 1h	5.8	5171 ± 1980	-6.6 ± 1.0	21.7 ± 1.5	16.2 ± 4.9
After 24h	5.6	4744 ± 3617	-5.9 ± 1.3	27.2 ± 1.0	20.3 ± 6.1

**: data are normalized and calculated as the ratio between the dissolved copper ions and the analysed total copper presents in copper oxide suspension.*

The high standard deviation of the hydrodynamic diameter size as calculated by making 3 consecutive measurements on 3 different batch dispersions (Appendix 2 Table S2.1) confirmed the low colloidal stability of synthetic sweat suspensions and the prevailing presence of multi-dispersed aggregates. If compared to water, the colloidal stability of synthetic sweat suspensions is even worse, as expected by the increased amount of dissolved salts and by the resulting compression of electric double layer[36]. ζ-pot values, in fact, decrease, approaching the IEP (pH value corresponding to ζ-pot = 0), so justifying the high instability that promotes the aggregation phenomena. Otherwise, the time of exposure does not seem to affect the colloidal stability and just after one hour of exposure the samples reach stable values of d_{DLS} and $\zeta\text{-pot}_{ELS}$.

In order to track the fate of CuO NPs in contact with human dermal target we measured the concentration of copper (as NPs or ions) throughout three different compartments, as schematized in Figure 3.2.2 (synthetic sweat; human skin: epidermis and dermis; receptor fluid). To understand how CuO NPs translocate through the human skin, we evaluated the total amount of copper present in the three compartments. Before discussing the results, it should be taken into account that it was possible to discriminate between the concentration of NPs and of ionic fraction (ions most likely released from the surface) only in the synthetic sweat, applying an UF treatment. This gave us an idea of the static dissolution in exposure conditions and provides an indication of the amount of copper that can easily cross the skin barrier or can be released if NPs themselves penetrate it.

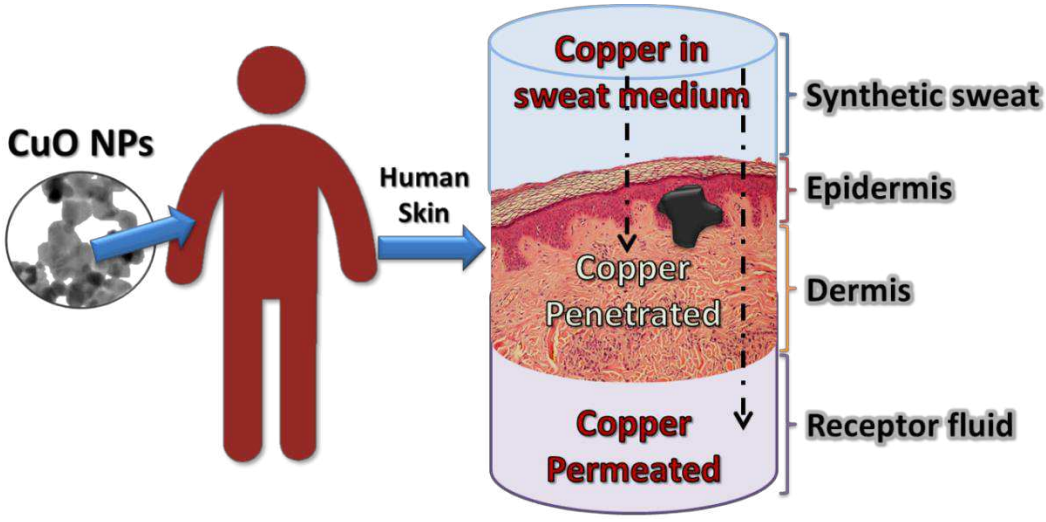

Figure 3.2.2: Scheme of human dermal exposure to CuO NPs: different compartments and translocation routes. CuO NPs in synthetic sweat is the donor phase, the skin (divided into epidermis and dermis) is where penetration processes occur and the physiologic solution is the receptor fluid where copper permeates.

In-vitro test

The Cu^{2+} ion static dissolution was measured in the synthetic sweat (Appendix 2 table S2.2) and compared with that of water[31]. The increasing dissolution from less than 1% (in water) to 20% (in synthetic sweat), is attributed to the decreased pH (from 6,5 to acidic pH 4,5 of sweat)[37].The copper skin penetration after 24h of exposure to human skin (100 µg mL^{-1} of CuO NPs in synthetic sweat), confirmed the expected low permeation of copper in the intact skin, with the highest value found in the epidermis, layer that works as main barrier against environmental pollutants. Even if few examples are reported in literature, metal oxide NPs, as CuO NPs, tend to aggregate especially in hollow such as hair bulbs, reducing penetration, that is so mainly due to ions released by NPs[5]. This behaviour is confirmed by Cohen et al. (2013), who investigated CuO NPs penetration into human skin by a different *in-vitro* set-up proving by TEM that mostly of CuO NPs are stopped by epidermis, without penetration into the inner skin layers[27]. Therefore, the most valuable hypothesis is that CuO NPs in their highly aggregated form, as confirmed by DLS analysis, are stopped in the first skin layer, most probably moving in hair bulbs[5] and reaching a concentration of around 1 µg cm^{-2} (1.05 ± 0.5 µg cm^{-2}). On the other side, the damaged skin doesn't present the same barrier activity and showed higher values of copper (NPs and ions), with a concentration of 2.73 ± 1.9 µg cm^{-2} in the epidermis and 7.09 ± 5.8 µg cm^{-2} in dermis (Fig. 3.2.3 and Appendix 2 Table S2.3).

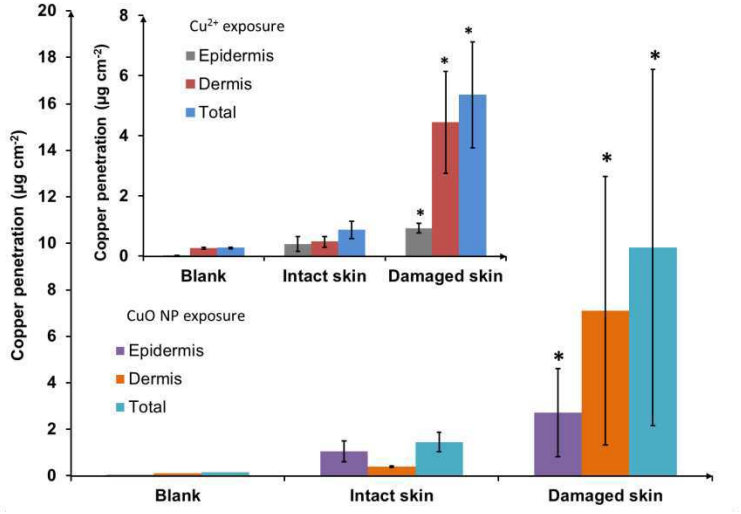

Figure 3.2.3: Copper skin penetration at 24 h to 100 µg mL^{-1} of CuO NPs in synthetic sweat, data are reported as mean and SD in the bar chart. In the small box: blank, intact and damaged skin (total p=0.046, epidermis p=0.04, dermis p=0.046) exposed to the ultrafiltered solutions (results expressed as means and SD). *: values are significant different from the blank.

To better investigate the ionic contribute to penetration, we got in touch ultrafiltered solutions to human skin in the Franz cell with a ionic concentration of 30 µg mL^{-1}. The results shown in the inset of Figure 3.2.3 evidenced that Cu^{2+} ions are able to reach the inner skin layers only if the epidermis is damaged, otherwise the copper penetration is negligible. In fact, for abraded skin, the copper amount in epidermis is of 0.92 ± 0.16 µg cm^{-2} while in dermis touches the value of 4.44 ± 1.69 µg cm^{-2}. Therefore, these data confirm that the epidermis acts as main barrier against both Cu^{2+} ions and CuO NPs dispersion. If we compare the corresponding mass concentration of Cu found in the epidermis for intact and damaged skin with literature exposure limit dose that causes some detrimental effects on keratinocytes cells (5 µg mL^{-1} of CuO NPs), we can conclude that both concentrations can cause possibly toxic effect for the skin.

As copper penetration as NPs or ions in the skin resulted relevant, we tested the percutaneous permeation of CuO nano-suspension that reached the receptor fluid (Fig. 3.2.4). Starting from both CuO NPs and Cu^{2+} solution we found that the permeation through intact skin was negligible and comparable with the blank sample (p = 0.08 for CuO NPs and p = 0.5 for Cu^{2+}). Otherwise, we observed a progressive increase of copper concentration in damaged skin. Copper was able to reach the physiological solution with a penetration value at 24 hours of 0.55 ± 0.44 µg cm^{-2} (p=0,046), an estimated flux of 0.04 ± 0.04 µg cm^{-2} h^{-1} and a lag time of 8.8 ± 1.9 hours. A very similar behavior was assessed for the Cu^{2+} ionic exposure (Fig. 3.2.4) with damaged skin.

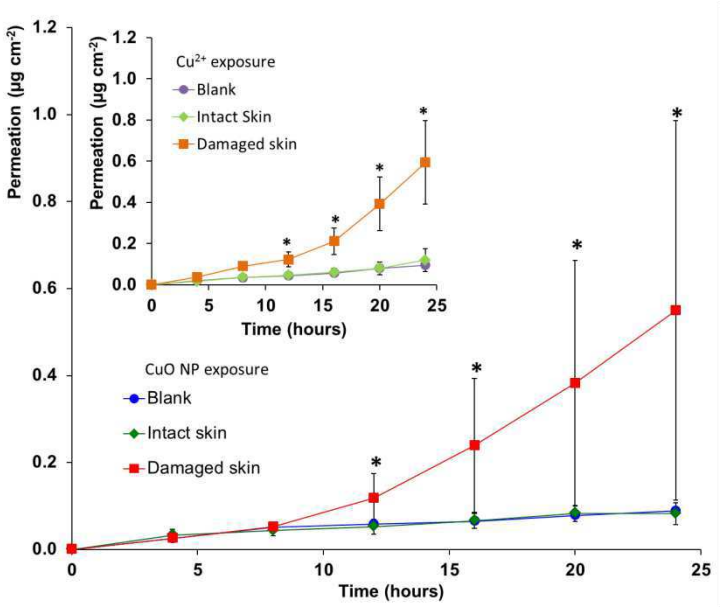

Figure 3.2.4: Copper penetration (means and SD) in receptor fluid for blank, intact and damaged skin. In the small box: blank, intact and damaged skin exposed to the ultrafiltered solutions (results expressed as means and SD). *: values are significant different from the blank.

In fact, starting from the Cu^{2+} solution as donor phase, the amount of ions able to reach the receptor fluid is very close to the value detected for the CuO NPs. For ions we calculated a penetration value at 24 hours of 0.59 ± 0.20 µg cm^{-2} (p=0,046), an estimated flux of 0.05 ± 0.02 µg cm^{-2} h^{-1} and a lag time of 11.6 ± 0.3 hours. The small differences in penetration after 24 hours between CuO and Cu^{2+} ions exposure is consistent with the hypothesis of a Trojan horse mechanism. Even if NPs and ions cannot be distinguished by the analytical evaluation, we can assume, based on our results and on literature data, that NPs and ions are not able to pass throughout the intact skin[27,38,39,40]. On the other hand in damaged skin, we can hypothesize that the amount of copper detected in the receptor fluid should be most likely associated to ions permeation and penetration vehiculated by CuO NPs within 24 hours of exposure[29].

To evaluate a possible systemic risk, we considered the NOAEL (No Observed Adverse Effect Level) and LOAEL (Lower Observed Adverse Effect Level) obtained for Cu ions after oral exposure of humans: Araya et al. (2002) reported a value of 0.011 mg kg^{-1} day and 0.018 mg kg^{-1} day (nausea) for a single exposure, respectively[41]. Considering an exposure of both hands and forearm of 100 cm^2 without cleaning procedures, the amount of Cu that, based on our data, can permeate the damaged skin would be 55 ± 44 µg, so well below the NOAEL calculated for a 70 kg man (0.77 mg). Nevertheless, we should take into account that data on NOAEL and LOAEL for CuO NPs are not available in literature, so the only extrapolation we can do, in order to estimate if we are below or above the exposure limits, is in terms of copper that reach the receptor fluids in its ionic form.

Conclusion

Franz model technique was used to investigate the total amount of copper permeating through human skin during a 24 hours period and the amount present inside the skin once divided in epidermis and dermis layer. Experiments were run with intact skin as well as abraded human skin following the Bronaugh and Steward protocol to estimate the effect of skin lesions on the permeation rate and the routes used by NPs or ions to gain penetration.

At our knowledge, this study represents one of the first-time results on human skin penetration of CuO NPs. Intact epidermis acts as good barrier against both Cu^{2+} ions and CuO NPs dispersion, presenting negligible copper passage through the skin. On the other hand, a higher value of penetration was observed in damaged skin where the amount of copper increased in time in the physiological fluid for exposure to both Cu^{2+} ions and CuO NPs. These results are comparable to previous studies on the cutaneous absorption of other metal oxide NPs[43,44,45], whilst the CuO NPs ion release detected was higher than the other tested NPs.

More broadly our study demonstrated that Cu can penetrate and permeate the skin in significant amount and toxicological data available in literature suggested a possible local effect, mainly when workers presented an impaired skin barrier. Our results suggested the need to protect workers' skin using personal protective equipment (double nitrile gloves) to avoid the direct contact with CuO NPs. A special caution needs to be applied for workers with an impaired skin barrier, although gloves can be considered protective.

References

1. Zanoni, I. *et al.* CuO nanoparticle penetration through intact and damaged human skin. *New J. Chem.* (2019). doi:10.1039/c9nj03373d

2. Walters, K. A. & Roberts, M. S. The Structure and Function of Skin, The Pilary Apparatus. in *Dermatological and Transdermal Formulations* (2002).

3. Crosera, M. *et al.* Nanoparticle dermal absorption and toxicity: A review of the literature. *Int. Arch. Occup. Environ. Health* **82**, 1043–1055 (2009).

4. Poland, C. A. *et al.* Dermal Absorption of Nanomaterials - Part of the "Better control of nano" initiative 2012-2015. in *The Danish Environmental Protection Agency* (2013). doi:10.11648/j.nano.20140204.14

5. Larese Filon, F., Mauro, M., Adami, G., Bovenzi, M. & Crosera, M. Nanoparticles skin absorption: New aspects for a safety profile evaluation. *Regul. Toxicol. Pharmacol.* **72**, 310–322 (2015).

6. Kumar, A. *et al.* Engineered Nanomaterials: Knowledge Gaps in Fate, Exposure, Toxicity, and Future Directions. *J. Nanomater.* **2014**, 16 pages (2014).

7. Karlsson, H. L., Cronholm, P., Gustafsson, J. & Moeller, L. Copper oxide nanoparticles are highly toxic: A comparison between metal oxide nanoparticles and carbon nanotubes. *Chem. Res. Toxicol.* **21**, 1726–1732 (2008).

8. Seabra, A., Durán, N., Seabra, A. B. & Durán, N. Nanotoxicology of Metal Oxide Nanoparticles. *Metals (Basel).* **5**, 934–975 (2015).

9. Figueiredo Borgognoni, C., Kim, J. H., Zucolotto, V., Fuchs, H. & Riehemann, K. Human macrophage responses to metal-oxide nanoparticles: a review. *Artif. Cells, Nanomedicine, Biotechnol.* 1–10 (2018). doi:10.1080/21691401.2018.1468767

10. Girigoswami, K. Toxicity of Metal Oxide Nanoparticles. in *Cellular and Molecular Toxicology of Nanoparticles* (eds. Saquib, Q., Faisal, M., Al-Khedhairy, A. A. & Alatar, A. A.) 99–122 (Springer International Publishing, 2018). doi:10.1007/978-3-319-72041-8_7

11. Líbalová, H. *et al.* Toxicity of surface-modified copper oxide nanoparticles in a mouse macrophage cell line: Interplay of particles, surface coating and particle dissolution. *Chemosphere* **196**, 482–493 (2018).

12. Gawande, M. B. *et al.* Cu and Cu-Based Nanoparticles: Synthesis and Applications in Catalysis. *Chem. Rev.* **116**, 3722–3811 (2016).

13. Grigore, M. *et al.* Methods of Synthesis, Properties and Biomedical Applications of CuO Nanoparticles. *Pharmaceuticals* **9**, 75 (2016).

14. Di Bucchianico, S. *et al.* Multiple cytotoxic and genotoxic effects induced in vitro by differently shaped copper oxide nanomaterials. *Mutagenesis* **28**, 287–299 (2013).

15. Perreault, F., Oukarroum, A., Melegari, S. P., Matias, W. G. & Popovic, R. Polymer coating of copper oxide nanoparticles increases nanoparticles uptake and toxicity in the green alga Chlamydomonas reinhardtii. *Chemosphere* **87**, 1388–1394 (2012).

16. Brinch, A., Hansen, S., Hartmann, N. & Baun, A. EU Regulation of Nanobiocides: Challenges in Implementing the Biocidal Product Regulation (BPR). *Nanomaterials* **6**, 33 (2016).

17. Di Bucchianico, S. *et al.* Multiple cytotoxic and genotoxic effects induced in vitro by differently shaped copper oxide nanomaterials. *Mutagenesis* **28**, 287–299 (2013).

18. Perreault, F. *et al.* Genotoxic effects of copper oxide nanoparticles in Neuro 2A cell cultures. *Sci.*

Total Environ. **441**, 117–124 (2012).

19. Noureen, A. *et al.* Assessment of copper nanoparticles (Cu-NPs) and copper (II) oxide (CuO) induced hemato- and hepatotoxicity in *Cyprinus carpio*. *Nanotechnology* **29**, 144003 (2018).

20. Rotini, A. *et al.* Insights into the CuO nanoparticle ecotoxicity with suitable marine model species. *Ecotoxicol. Environ. Saf.* **147**, 852–860 (2018).

21. Gosens, I. *et al.* Organ burden and pulmonary toxicity of nano-sized copper (II) oxide particles after short-term inhalation exposure. *Nanotoxicology* **10**, 1084–1095 (2016).

22. Costa, P. M. *et al.* Transcriptional profiling reveals gene expression changes associated with inflammation and cell proliferation following short-term inhalation exposure to copper oxide nanoparticles. *J. Appl. Toxicol.* **38**, 385–397 (2018).

23. Anreddy, R. N. R. Copper oxide nanoparticles induces oxidative stress and liver toxicity in rats following oral exposure. *Toxicol. Reports* **5**, 903–904 (2018).

24. Akhtar, M. F. *et al.* Toxicity Appraisal of Untreated Dyeing Industry Wastewater Based on Chemical Characterization and Short Term Bioassays. *Bull. Environ. Contam. Toxicol.* **96**, 502–507 (2016).

25. Hu, X., Cook, S., Wang, P. & Hwang, H. In vitro evaluation of cytotoxicity of engineered metal oxide nanoparticles. *Sci. Total Environ.* **407**, 3070–3072 (2009).

26. Cathe, D. S., Whitaker, J. N., Breitner, E. K. & Comfort, K. K. Exposure to metal oxide nanoparticles in physiological fluid induced synergistic biological effects in a keratinocyte model. *Toxicol. Lett.* **268**, 1–7 (2017).

27. Cohen, D. *et al.* Evaluation of topically applied copper(II) oxide nanoparticle cytotoxicity in human skin organ culture. *Toxicol. Vitr.* **27**, 292–298 (2013).

28. Wang, M. Evaluation of immunoresponses and cytotoxicity from skin exposure to metallic nanoparticles. 4445–4459 (2018). doi:10.2147/IJN.S170745

29. Chang, Y.-N., Zhang, M., Xia, L., Zhang, J. & Xing, G. The Toxic Effects and Mechanisms of CuO and ZnO Nanoparticles. *Materials (Basel).* **5**, 2850–2871 (2012).

30. Applerot, G. *et al.* Understanding the antibacterial mechanism of CuO nanoparticles: Revealing the route of induced oxidative stress. *Small* **8**, 3326–3337 (2012).

31. Ortelli, S. *et al.* Colloidal characterization of CuO nanoparticles in biological and environmental media. *Environ. Sci. Nano* **4**, 1264–1272 (2017).

32. Franz, T. J. Percutaneous Absorption. On the Relevance of in Vitro Data. *J. Invest. Dermatol.* **64**, 190–195 (1975).

33. Fasano, W. J., Manning, L. A. & Green, J. W. Rapid integrity assessment of rat and human epidermal membranes for in vitro dermal regulatory testing: correlation of electrical resistance with tritiated water permeability. *Toxicol. Vitr.* **16**, 731–740 (2002).

34. Davies, D. J., Ward, R. J. & Heylings, J. R. Multi-species assessment of electrical resistance as a skin integrity marker for in vitro percutaneous absorption studies. *Toxicol. Vitr.* **18**, 351–358 (2004).

35. Bronaugh, R. L. & Stewart, R. F. Methods for In Vitro Percutaneous Absorption Studies V: Permeation Through Damaged Skin. *J. Pharm. Sci.* **74**, 1062–1066 (1985).

36. Brown, M. A., Goel, A. & Abbas, Z. Effect of Electrolyte Concentration on the Stern Layer Thickness at a Charged Interface. *Angew. Chemie Int. Ed.* **55**, 3790–3794 (2016).

37. Peng, C. *et al.* Transformation of CuO Nanoparticles in the Aquatic Environment: Influence of pH, Electrolytes and Natural Organic Matter. *Nanomaterials* **7**, 326 (2017).

38. Barry, B. . Novel mechanisms and devices to enable successful transdermal drug delivery. *Eur. J. Pharm. Sci.* **14**, 101–114 (2001).

39. Crosera, M. *et al.* In vitro dermal penetration of nickel nanoparticles. *Chemosphere* **145**, 301–306 (2016).

40. Larese Filon, F. *et al.* In vitro percutaneous absorption of cobalt. *Int. Arch. Occup. Environ. Health* **77**, 85–89 (2004).

41. Araya, M. *et al.* Determination of an Acute No-Observed-Adverse-Effect Level (NOAEL) for Copper in Water. *Regul. Toxicol. Pharmacol.* **34**, 137–145 (2001).

42. Rosen, J., Landriscina, A. & Friedman, A. Nanotechnology-Based Cosmetics for Hair Care. *Cosmetics* **2**, 211–224 (2015).

43. Crosera, M. *et al.* Titanium Dioxide Nanoparticle Penetration into the Skin and Effects on HaCaT Cells. *Int. J. Environ. Res. Public Health* **12**, 9282–9297 (2015).

44. Mauro, M. *et al.* Cobalt Oxide Nanoparticles: Behavior towards Intact and Impaired Human Skin and Keratinocytes Toxicity. *Int. J. Environ. Res. Public Health* **12**, 8263–8280 (2015).

45. Mauro, M. *et al.* In vitro transdermal absorption of Al2O3 nanoparticles. *Toxicol. Vitr.* **59**, 275–280 (2019).

3.3.3 SP-ICP-MS as powerful tool for the evaluation of baby porcine mucosa exposure to silver nanoparticles

Source (under submission paper)

Introduction

Nowadays, silver nanoparticles (Ag NPs) are widely diffuse on the market in different application of common use, like food packaging, containers, toothpaste and teeth brushes, alcohol free mouthwash, nasal sprays, nipples and nursing bottles, technical textile, medical devices, water purification devices etc.[1,2,3]. The large use of Ag NPs in many applications that involve human occupational and consumer scenarios is justified by their known antibacterial, antiviral and antifungal properties to prevent infections. Despite to its ancient use, "Collargol" nano-silver has been used for medical applications and manufactured commercially since 1897, nano-silver found a renewal when its use as a "silver ion releasing" nanotechnology became supported by scientific evidences[4]. Besides the lot of benefits that the use of nano-silver can generate, in terms of resources conservation, disease prevention, many concerns about its potential toxicity for human health and / or environments raised[5,6]. The Environmental Protection Agency (EPA) suggests a value of silver < 5 μg kg^{-1} daily as reference dose (Rfd) for oral exposure and allows a total daily amount of 350 μg of silver for an 70 kg adult[7]. Moreover, silver intoxication (*argyria*) is reported in literature and has been described through oral route, in people who drank it for deliberate uptake[8,9], or through skin route, when wound dressings containing Ag NPs are used on burns for more than 30% of the skin surface[10]. The Agency for Toxic Substances and Disease Registry (ATSDR) describes *argyria* as a "cosmetic problem", since it consists mostly in a not reversible bluish-gray discoloration of the skin[11]. Nevertheless there are isolated reports of more serious neurologic, renal and hepatic complications caused by the ingestion of colloidal silver[12,13].

Definitely, Ag NPs are able to come in contact during their lifetime with human targets and in specific with oral mucosa[14,15], especially in applications in the food and personal care sectors. Oral mucosa traditionally acts as first barrier to xenobiotics in the digestive tract[16,17], but due to its histological structure oral mucosa shows a permeability 20 times higher to water[18] and 4 up to 4,000 times higher to different drugs if compared to skin[19]. Despite the research efforts, transoral absorption and penetration of NPs through mucosa are not completely known

and not yet been fully defined[20]. Moreover, experimental data derive in most cases from animal or human adult donor skin, thus findings are applicable only to predict the adult population transdermal permeation. Focusing on adult mucosa exposed to Ag NPs, Mauro et al. (2015) demonstrated that silver can permeate the oral mucosa barrier and that absorption is substantially due to translocation of Ag^+ ions[21]. This study investigated the permeation of Ag NPs through oral mucosa, using adult porcine mucosa as *in-vitro* model. In fact, the porcine lining mucosa is the most similar to the human one in terms of structure and enzyme activity and is a deeply investigated *in-vitro* model to estimate human buccal absorption and drug penetration[18]. Although NPs penetration through oral mucosa is not fully known for adults, less data are available for permeation / penetration in children as well.

Children are likely exposed to Ag NPs that are already embedded in commercial products used by children - such as pajamas, baby blankets, plush toys – and also in items used around children - such as disinfecting sprays, surface wipes and kitchen scrubbers[22], exposing skin and buccal cavity of children to silver ionic and NPs form. In addition, children's skin and oral mucosa significantly differ from the one of adults and so the available nanotoxicological knowledge cannot predict infant's dermal and oral absorption. Case reports have shown that infant's transdermal exposure can lead to systemic effects, due to the differences in permeability and in the activity of metabolic pathways, that can transform a nontoxic substance for adults into a toxic substance for children, but data on nanotoxicology and biokinetics in childhood are lacking[23,24,25]. Children dermal and oral exposure to NPs are issues that need to be addressed, in order to better define the risk of exposure also in comparison with adults.

For the above reasons, in this work, we performed experiments to investigate the possible penetration / permeation of Ag NPs into / across the children buccal mucosa, using a standard dermatological *in-vitro ex-vivo model* (Franz cell), applied to oral baby porcine mucosa[26,27]. In particular, we coupled for the first time in this application, the Franz cell model with the use of Single Particle – Inductively Coupled Plasma – Mass Spectrometry (SP-ICP-MS) technique, to estimate, directly in biological fluid, the Ag NPs transformation and translocation (fate). SP-ICP-MS is an evolving tool for NPs analysis in environmental and biological fluids, based on ICP-MS technique and able to detect single NPs in medium, providing info such as size distribution (nm), dissolved metal element content ($\mu g\ mL^{-1}$) and particle number concentration (number mL^{-1}) at low concentration range (order of ng mL^{-1})[28–34], without needing any pre-treatment of biological matrix for solubilizing NPs. In this work we tracked Ag NPs in physiological receptor fluid over 240 min of exposure by following the penetration and the

permeation of ions, analyzing both the ionic concentration, as well as the NPs degree of aggregation / agglomeration.

SP-ICP-MS Theory

One of the main challenges in nanotechnology is a more and more rapid, simultaneous characterization of NPs elemental composition, number, size, and size distribution, giving rapid information about exposure scenario of both human and environment[35,36]. For inorganic NPs, the technique best suited to provide the above-mentioned characteristics is ICP-MS operated in so-called single particle mode. The SP-ICP-MS technique is an evolving tool for NPs analysis in environmental and biological fluids. It is based on the ICP-MS technique and implemented with data analysis software, able to detect single NPs in medium, providing simultaneously the NPs size distribution, dissolved metal element content and particle number concentration at low concentration range[37].

Different authors deeply explained the theory of this technique[34,35,38,39]. Basically, the SP-ICP-MS involves a process of counting events corresponding to individual NPs, which requires isolation of the contribution of the NPs from that of the background / dissolved analyte, and avoiding the occurrence of multiple-NPs events[34]. NPs suspension is continuously introduced through conventional nebulization systems used in ICP-MS method and injected in the argon plasma torch, where the droplets are ionized, producing a burst of ions (one ion cloud per particle) as described in Figure 3.3.1 (1-2 steps).

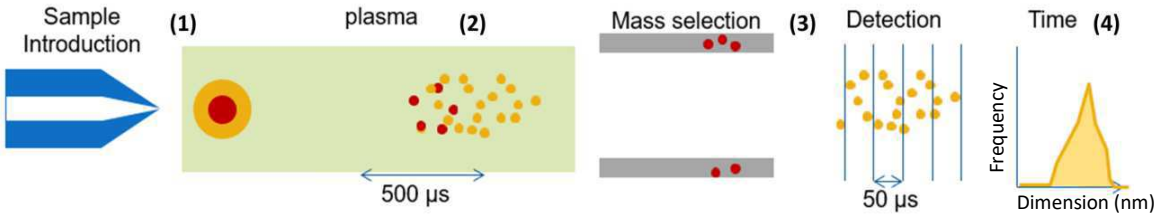

Figure 3.3.1: Scheme of SP-ICP-MS nanosol sample introduction and analysis divided in four steps: (1) introduction, (2) ionization, (3) mass selection and detection, (4) instrument output.

The ions ionized then pass into the quadrupole to be sorted by their mass-to-charge ratios (m/z) as showed in Figure 3.3.1 step 3. Only a single mass is being measured for single particle analysis at time. In SP-ICP-MS, transient data acquisition speed consists of two parameters: dwell time (reading time) and settling time (overhead and processing time)[40]. The challenge is that SP-ICP-MS is able to acquire signals at a dwell time shorter than the NPs transient time, thus avoiding false signals generated from partial particle integration, particle

coincidence and agglomerates / aggregates. The shorter the settling time, the less chance there is to miss a nanoparticle. If, for example, the ion cloud happens to fall within the dwell time window, it will be detected and generate a signal (peak) on the Frequency vs Dimension graph (Figure 3.3.1 step 4), producing a distribution graph. Otherwise, if it passes into the quadrupole or reaches the detector during the settling time, it will not be detected, leading to an inaccurate counting efficiency. Therefore, in SP-ICP-MS analysis the dwell time has to be smaller than or equal to 100 µs to obtain a precise NPs counting and sizing. While when dissolved elements are analyzed, the resulting signal is essentially a steady-state signal as background to the peaks[29,37].

Actually, SP-ICP-MS is still not fully exploited in research and applied in few fields. This is basically due to two motivations: the instrumental need to have well-dispersed NPs systems and the necessity to have simple medium, unable to dirty the inert parts of the instrument[29,34,35,40].

Recently the use of SP-ICP-MS as analytical methods is growing and reached different application fields dealing with complex biological and environmental matrices. SP-ICP-MS was used to analyze NPs content in fresh water and seawater, supporting the evaluation of the NPs impact on environment, through information such as NPs concentration, size modification and dissolution process [28,41,42,43]. The same approach was used in biological media, and the NPs presence in relevant media, such as human blood and commercially available dietary supplements[14,15], was investigated. The scientific community expects to improve the use of this technique also in other fields still unexplored.

Experimental section

Chemicals. All chemicals used were of analytical grade. Sodium chloride, sodium hydrogen phosphate, potassium dihydrogen phosphate, glutaraldehyde (50% v/v), nitric acid (69% v/v), hydrochloric acid (36.5–38% v/v) and hydrogen peroxide (30%) were purchased from Sigma Aldrich (Milan, Italy), while ammonium hydroxide (25%) from J.T. Baker (Milan, Italy). Water reagent grade was produced with a Millipore purification pack system (MilliQ water). The physiological solution used as receptor fluid was prepared by dissolving 2.38g of Na_2HPO_4, 0.19g of KH_2PO_4 and 9g of NaCl into 1L of MilliQ water (final pH = 7.35).

Nanoparticles. Silver NPs suspensions for this study were supplied by NanoAmor Materials Inc. (Houston, TX, USA) and were stabilized with PVP - polyvinylpirrolidone (content of silver: 25% w/w, polymer 75%).

Standards. Ionic Au and Ag standard were used for ionic calibration of ICP-MS, respectively ion mass of 197 and 107 u.m.a. Au 60 nm citrate coated NPs were used as standard

for Single-Particle software calibration material (Appendix 3, Table S3.1). All standards used were purchased from Sigma Aldrich (Milan, Italy).

Donor phases preparation. In order to discriminate between Ag NPs and silver ions permeation, released from the NPs, two different donor phases were prepared just before the experiments. The first donor phase (donor fluid 1), consisting of the Ag NPs suspension, was prepared using 200 mg of PVP coated Ag NPs dispersed in 100 mL of physiological solution and sonicated, at the aim to obtain a concentration of 500 mg L^{-1} (as silver content). While, the second donor phase (donor fluid 2) was prepared by ultrafiltration process, starting from first one and collecting only the ultrafiltered phase, containing the water-soluble silver species of the donor 1. The first donor phase was ultrafiltered in centrifuge at 5000 rpm for 30 min by means of Amicon Ultra-4 centrifugal filters (10 KDa MWCO). Five ultrafiltered aliquots (of 4 mL each) were mixed and used during the permeation experiments as second donor phase. The filtered solution was analyzed by ICP-OES, and the concentration of ions quantified (25 mg L^{-1} - 5% of the donor fluid 1 silver content) and checked also after the end of the experiments, to confirm that remained stable.

Intrinsic properties. Ag NPs dispersed in physiological solution were characterized to evaluate NPs size and morphology with a transmission electron microscope (EM208; Philips, Eindhoven, The Netherlands operating at 200 kV) with a high definition acquisition system based on a side-mounted TEM camera OSIS Morada and an iTEM soft-ware platform (Olympus Soft Imaging Solutions GmbH, Münster, Germany).

System-dependent properties. Dynamic light scattering (d_{DLS}) and Zeta potential (ZP - ζ-pot_{ELS}) measurements on Ag NPs were carried out using a ZetasizerNano ZS (Malvern Instruments Ltd.). Ag NPs suspension was diluted 1:5 in physiological solution and loaded into low size disposable cuvette. Summary statistics were obtained using quadruplicate 3 min analysis (total analysis time = 12 min). Instrument performance was verified using a polymer reference standard known to be 60 nm. While zeta potential was calculated using Henry's equation.

Preparation of oral mucosa. Due to its morphological and enzymatic similarities with the children mucosa, baby porcine oral mucosa was used for the *in-vitro* experiments[18,26,27]. The membranes were obtained immediately after pig's slaughter (porcine age between 4 and 8 months). During the transport to laboratory the tissue was stored at 4°C and then in freezer at −80°C for a period of time up to, but not exceeding, 1 week. On the day of the experiment, the tissue was removed from the freezer and thawed in physiological solution, at RT, for

approximately 30 min before the permeation experiment. It has been shown that this method of storage does not affect the mucous barrier properties, since no change in the permeability has been previously mentioned[44]. Mucous membranes integrity was tested as suggested by Lestari[45].

In-vitro diffusion system. Percutaneous absorption studies were performed using static diffusion cells following the Franz model[46]. In mucosal permeation studies, the receptor compartment has a mean volume of 4.5 mL and was maintained at 37°C by means of circulation of thermostated water in the jacket surrounding the cells throughout the experiment. This temperature value has been chosen in order to reproduce oral physiological conditions. The concentration of the salt in the receiver fluids was approximately the same that can be found in the blood. The solution in each cell was continuously stirred using a Teflon coated magnetic stirrer. Each excised sheet of mucosa was clamped between the donor and the receptor compartment in such a way that the epithelium faced the donor, and the connective tissue region faced the receiver compartment. The mean exposed area of the mucous membranes was 0.95 cm^2. The experiments were performed as follows.

Exp. 1: The first experiment has been performed with the donor fluid 1 containing a suspension of Ag NPs and ions naturally leached from the surface. At time 0, the exposure chambers of 4 Franz diffusion cells were filled with 1 mL of physiological solution and 0.5 mL of Ag NPs suspension (260 µg cm^{-2}). In order to check the provided infinite dose, total concentration in each cell has been confirmed at the end of the experiments by means of ICP-MS analysis. At selected intervals (20, 40, 60, 90, 120, 150, 180, 210, 240 min) 1 mL of the receiving bathing solution was removed and collected for the analysis, and immediately replaced with an equal volume of fresh physiological solution. The experiment was carried out for 240 min, as suggested in other studies[20,21]. At the end of the experiment the mucosa pieces were removed, washed abundantly with MilliQ water, and subsequently stored in the freezer together with mucosal bathing solutions and the donor solutions for the following ICP-OES and ICP-MS / SP-ICP-MS analysis. The experiment was repeated twice for a total of 8 cells.

Exp. 2: The second experiment has been performed with the donor fluid 2, containing Ag^+ ions extracted from the donor phase 1. The exposure chambers of 4 Franz diffusion cells were filled with 1 mL of physiological solution and 0.5 mL of the Ag ultra-filtered solution (13 µg cm^{-2}). The other test conditions were the same of the experiment 1. The experiment was repeated twice for a total of 8 cells.

Four cells were used as blanks following the same procedure described in exp 1 but without the exposure to Ag NPs.

Mucosal digestion. All the mucosal exposed samples were collected and stored individually in freezer at −25°C for the following digestion and analysis. At the time of the analysis, the skin membranes were dried for 2 h at RT, weight, and then acid-digested in a closed microwave system (Multiwave PRO, Anton Paar) using 2.5 mL of HNO_3 (69%) and 0.5 mL of H_2O_2 (30%) for digestion. The obtained solutions diluted to a final volume of 10 mL with MilliQ water for the ICP-OES analysis.

Inductively coupled plasma mass spectroscopy (ICP-MS) and Single Particle application (SP-ICP-MS). Total Ag concentration in the solutions resulting from the mineralization of the mucosa samples were performed by ICP-OES using an Optima 8000 Spectrometer (PerkinElmer, U.S.A.), equipped with an S10 Autosampler. Analysis were conducted using a calibration curve obtained by dilution (range: 0 - 10 mg L^{-1}) of Ag standard solution for ICP-OES analyses. The LOD for Ag at the operative wavelength of 328.068 nm was 0.01 mg L^{-1}. The precision of the measurements expressed as RSD % for the analysis was always less than 5%.

An Inductive Coupled Plasma Mass Spectrometer, ICP-MS Nexion 350X with an ESI autosampler (Perkin Elmer, USA instrument), was used to determinate the total silver concentration in the donator and receiver phases. The analysis was carried out in KED mode using ultra-high purity helium (flow rate of 4.8 mL min^{-1}) to minimize polyatomic interferences. A five-points standard curve, obtained by dilution of Ag standard solution for ICP-MS analyses, was used for ICP-MS and SP-ICP-MS silver ionic calibration measurements (0.5, 1, 5 and 10µgL^{-1}, ion mass 107 u.m.a.).

For SP-ICP-MS analysis all samples were run using the Nano Application Module in Syngisitx™ software (version 2.1). A pump speed -20 rpm for flush, wash and delay, and nebulizer gas flow of 1.12 mL min^{-1} were used for measurements. The sample uptake was 0.34 mL min^{-1} and a dwell time of 50 µs was used with 60 s sampling times. To calculate the transport efficiency (1, 5 and 10 µg L^{-1}) ionic Au standard was used for SP-ICP-MS ionic calibration (ion mass 197 u.m.a.). While Au 60 nm NPs citrate coated suspension were used as standard for NPs size dimension in Single-Particle software calibration material. The 60 nm Au particles were diluted in MilliQ water to 50,000 particles number mL^{-1} for SP-ICP-MS size calibration. NPs concentration and other parameters were provided by the supplier (See Appendix 3, Table S3.1). We calculate a transport efficiency of 4%. The Ag calibration curve for dissolved metal element content was performed using Ag ionic standard (0.5, 1, 5 and 10 µg L^{-1},

ion mass 107 u.m.a.). Calibration curve obtained for Ag dissolution concentration is reported in Figure S3.2, Appendix 3.

Statistical Analysis. Ag concentration data (μg cm^{-3}) in the receptor solution were converted to the Ag amount that penetrated per skin surface unit (μg cm^{-2}). Data analysis was performed with Excel for Windows, release 2007 and Stata Software, version 11.0 (StataCorp LP, College Station, TX, USA). Skin absorption data were reported as mean ± SD. The difference among independent data was assessed by means of the Mann-Whitney test. A p value <0.05 was considered significant.

Results and Discussion

Properties of Ag NPs colloidal dispersion

The particle size distribution of Ag NPs in water and in exposure condition (donor fluid 1) was evaluated. TEM images (Figure 3.3.2) show spherical NPs with a quite narrow distribution of size quantified as 19 ± 5 nm. TEM measurements were compared to DLS size distribution (Figure S3.1, Appendix 3).

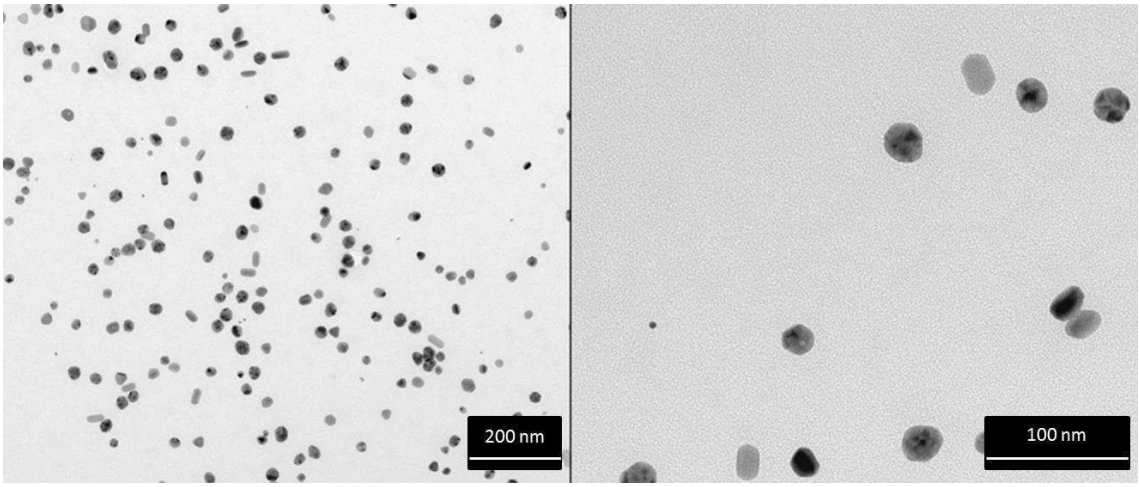

Figure 3.3.2: TEM images of the Ag NPs dispersed in physiological solution, number of measured NPs: 100 (A: bar = 200 nm; B: bar = 100 nm).

The analysis revealed a stable suspension with mean d_{DLS} equal to 57 nm, a polydispersity index (PdI) of 0.280 and a ζ-pot_{ELS} of −11.4 ± 0.2 mV. The apparent mismatch between TEM and DLS sizes was the result of various facts, as elsewhere reported[47]. In principle the DLS technique measure the hydrodynamic size as a result of aggregated units or of particles embedded in a polymeric matrix, as is the case of such PVP coated Ag NPs.

Ag permeation through oral mucosa – in-vitro ex vivo Franz cell model

Passive silver flux permeation and penetration was demonstrated through baby porcine oral mucosa after 240 min to both donor fluids: NPs and ions. In order to track the translocation of Ag NPs and ions in contact with oral mucosa we measured the concentration of silver throughout three different compartments, as schematized in Figure 3.3.3 (donor fluid; mucosa and receptor fluid).

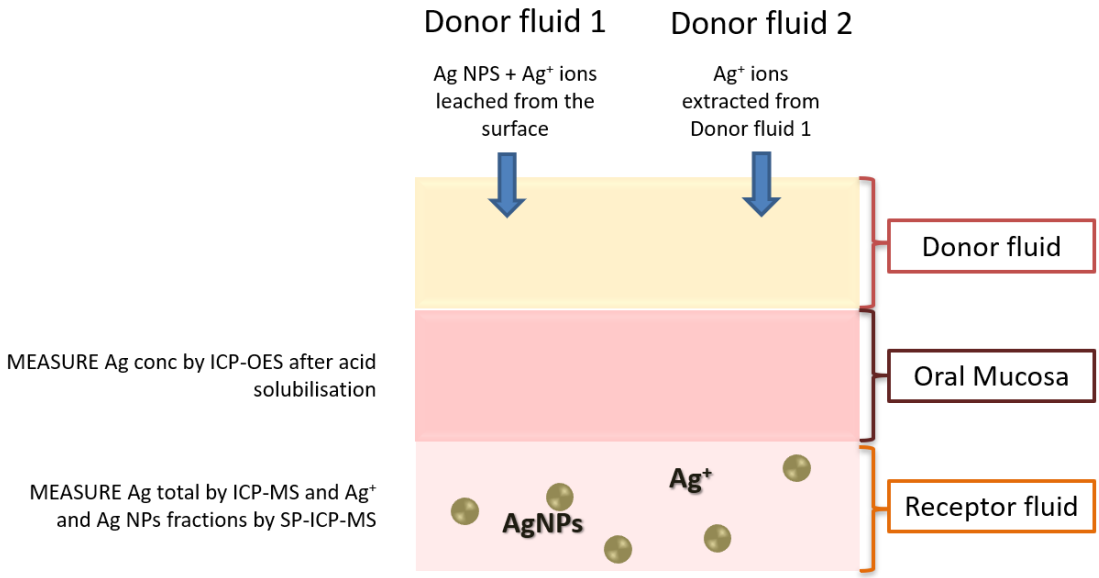

Figure 3.3.3: Scheme of oral model exposed to Ag NPs: different compartments (donor fluid, mucosa and receptor fluid) and translocation routes (penetration and permeation of NPs and ions).

Ag penetration in oral mucosa

The concentration of Ag in donor fluid 1 and 2 was respectively 260 µg cm^{-2} and 13 µg cm^{-2}. We selected different exposure time (20, 40, 60, 90, 120, 150, 180, 210, 240 min) and evaluated the penetration of silver species (NPs and ions) through mucosa. After 240 min we measured the Ag concentration in the oral mucosa, finding a higher Ag concentration for Ag NPs fluid (0.32 µg cm^{-2}) if compared with that of Ag^+ solution (0.08 µg cm^{-2}). This result suggests that in the case of donor fluid 1 passed in the mucosa not only the ionic fraction (same content as in donor fluid 2) but also NPs fraction (Figure 3.3.4).

Comparing our results with the penetration of Ag NPs in adult porcine mucosa, described by Mauro et al. (2015)[21], we found an higher content of penetrated silver (as NPs and ions) in baby tissues, despite the same exposure conditions and concentrations. The most valuable hypothesis was due to differences between young and adult's membrane features.

Skin and oral mucosa thickness is age-dependent[48], as consequence developing-skin / mucosa permeability is higher compared to adult membranes, especially during the first year of life, justifying an higher accumulation of silver in the mucosa[26,27,49].

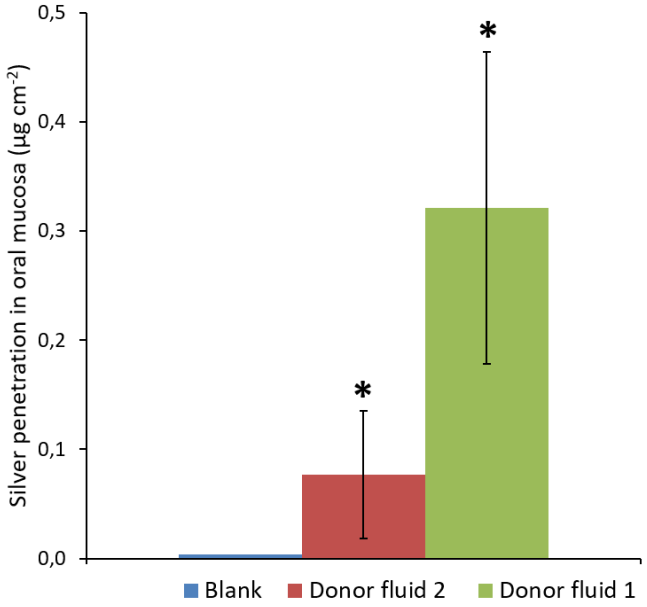

Figure 3.3.4: Silver detected in oral mucosa from two donor fluids after 240 min exposure. (*: values significantly different from the blank, $p < 0.05$)

Ag permeation in receptor fluid

The silver permeation in the receptor fluid are reported in Figure 3.3.5. The permeation of donor fluid 2 resulted almost negligible and comparable with blank. This suggest that Ag^+ ions are more probably stopped and absorbed into oral mucosa, that acts as main barrier, without reaching the receptor fluid. While for donor fluid 1 (Ag NPs + Ag^+), we observed a passage of silver in the receptor fluid with a flux of 4.1 ± 1.7 ng cm^{-2} min^{-1} and a lag time of 159 ± 17 min. This result support the hypothesis that a translocation of NPs through tissue occurs, promoting potentially toxic effects through a Trojan horse mechanism, that would justify the higher cytotoxicity of Ag NPs if compared with the same concentration of Ag ions[50].

In addition these results confirmed an higher permeation values in baby porcine in comparison with adult porcine analyzed by Mauro et al. (2015)[21]. The flux permeation in adult mucosa after 240 minutes of application, in fact showed final values nearby two order lower than with baby porcine (flux measured in hours of exposure: 6.8 ± 4.5 ng cm^{-2} and 5.2 ± 4.3 ng cm^{-2}, donor fluid 1 and 2, respectively), whilst the lag times of 114 ± 42 min and 102 ± 42 min (donor fluid 1 and 2, respectively) was faster that in baby individual.

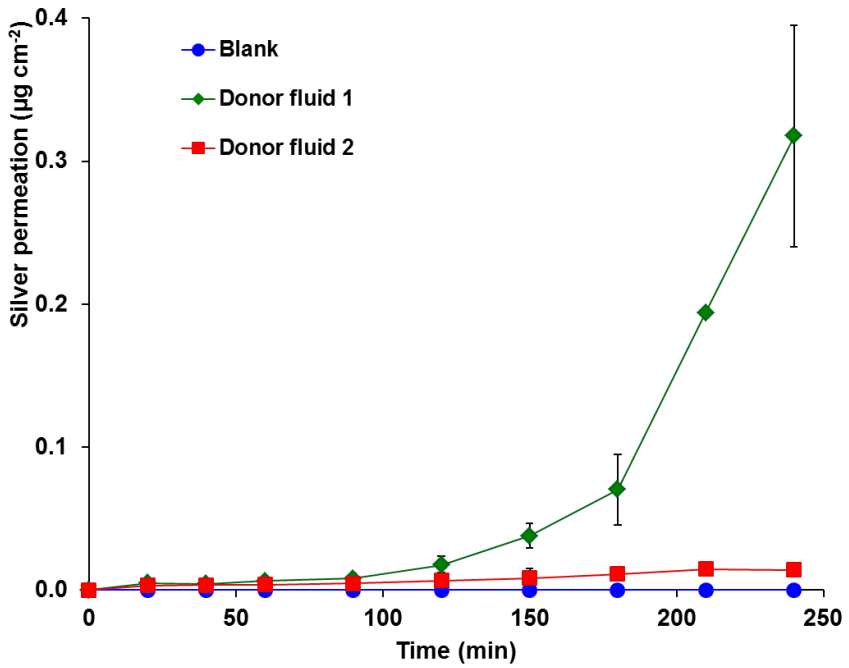

Figure 3.3.5: Silver penetration (means and SD) through oral mucosa in receptor fluid for blank, donor fluid 1 and 2 (*: values are significant different from the blank, $p < 0.05$).

The results of SP-ICP-MS analysis of the receptor fluid, exposed to donor fluid 1 (speciation between Ag NPs and Ag^+ ions), are reported in Table 3.3.1, in Figure 3.3.6 and in Figure S3.3, Appendix 3. As shown in Figure 3.3.5 the permeation of Ag has a time lag of ca. 150 min. So, as reported in Table 3.3.1, the first NPs reaching the receptor fluid (after 150 min of exposure), have a size comparable with TEM images, suggesting a passage through the oral mucosa of NPs in their native dimension.

Increasing the time of exposure, Ag NPs size increased, passing from 19 nm to 31 nm, indicating a slight agglomeration during the permanence of Ag NPs in the receptor fluid (Figure 3.3.7). The differences between most frequent size and mean size (higher for all exposure time), shown in Figure 3.3.7 are associated to the presence of a higher amount of larger NPs in the Gaussian distribution. This would confirm a slight aggregation of NPs, induced in all cases by the saline medium and passage through the oral mucosa, more evident after 240 min of exposure.

Finally, the number of detected Ag NPs, and, as expected, their fraction over the total concentration of Ag (c.a. 75%), don't seem to be affected by time and reach stable values already after 150 min.

Table 3.3.1: SP-ICP-MS measurement of receptor fluid exposed to donor fluid 1.

Time (min)	Most Freq. Size (nm)	Mean Size (nm)	Part. Conc. (number mL^{-1})	Diss. Conc. (µg L^{-1})	Fraction Ag dissolved (%)	Fraction of AgNPs (%)
240	31 ± 8	38 ± 9	177445 ± 87374	1.45 ± 1.25	35 ± 10	65 ± 10
210	24 ± 0	29 ± 1	322290 ± 78447	0.51 ± 0.07	16 ± 1	84 ± 1
180	21 ± 7	26 ± 9	155136 ± 120250	0.39 ± 0.22	23 ± 6	77 ± 6
150	19 ± 7	23 ± 8	215576 ± 120408	0.35 ± 0.29	25 ± 9	75 ± 9

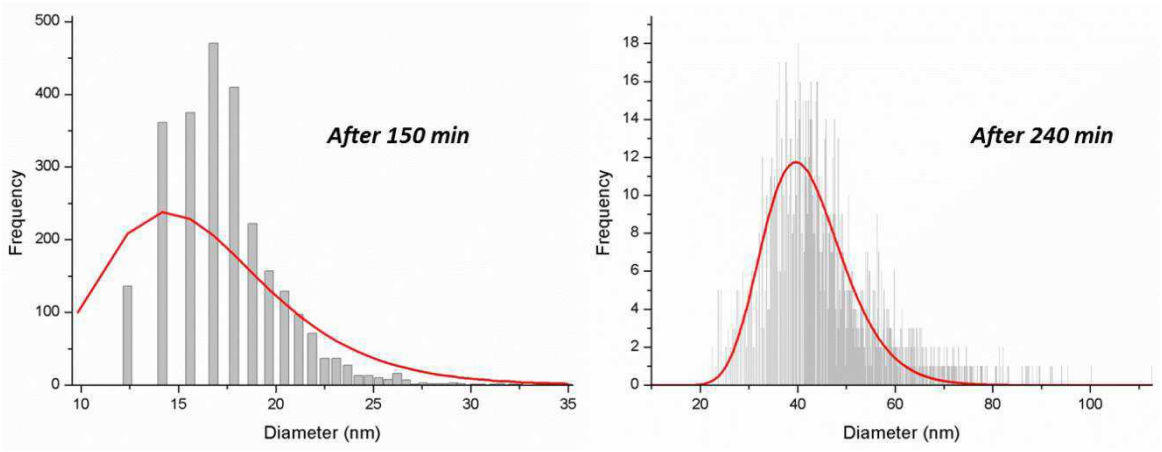

Figure 3.3.6: Size distribution of Ag NPs in receptor fluid after 150 and 240 min of exposition.

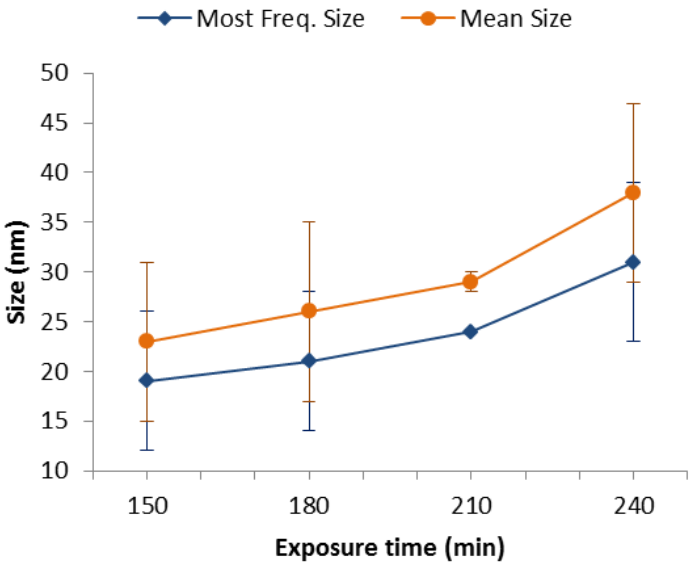

Figure 3.3.7: Size distribution of Ag NPs permeated in the receptor fluid as a function of time (◆ most frequent size and ■ mean size).

Therefore, we found that Ag NPs are able to penetrate the baby porcine oral mucosa, reaching the receptor fluid and being potentially available for translocation processes in the body *in-vivo* compartments. The increase in ions amount, from 5% in donor fluid, to ca.25% in the receptor fluid can be most likely attributed to Ag NPs surface transformation (adsorption of bio-surfactants when crossing mucosa) that could justify the higher amount of ions released that stay in equilibrium with solid surface[51]. Due to similarity between human and pig membranes, as reported in literature[26], it's reasonable to assume that a trans-oral mucosa passage could occur also in children mucosa once in contact, voluntary or accidentally, with silver NPs.

Conclusion

At our knowledge, this work presents one of the first attempts to evaluate Ag NPs permeation and penetration through baby porcine oral mucosa to predict the effect of potential oral absorption of Ag NPs in children. Franz *ex-vivo in-vitro* model was used to investigate the total amount of silver penetrating the oral mucosa and achieving the receptor fluid, during the first 240 min of exposure. The comparison between the two donor fluids, the first containing Ag NPs dispersion and the second only the ionic fraction, collected from the first donor fluid, suggested that only Ag NPs crossed the mucosa, reaching the donor fluid. The SP-ICP-MS analysis of the receptor fluid allowed the speciation between Ag NPs and Ag^+ ions, revealing that the Ag NPs reaching the receptor fluid are quite well dispersed, able to release a higher amount of ions if compared to the donor fluid. Due to the similarity between human and pig oral mucosa, these findings would support a Trojan horse mechanism, driving potential toxic effects induced by human oral mucosa exposure to Ag NPs, especially in baby individuals.

References

1. Hadrup, N. *et al.* Subacute oral toxicity investigation of nanoparticulate and ionic silver in rats. *Arch. Toxicol.* **86**, 543–551 (2012).

2. Kim, Y. S. *et al.* Subchronic oral toxicity of silver nanoparticles. *Part. Fibre Toxicol.* **7**, 20 (2010).

3. Abadi, M. F. D. *et al.* Silver nanoparticles as active ingredient used for alcohol-free mouthwash. *GMS Hyg. Infect. Control* **8**, 1–8 (2013).

4. Schneider, G. Antimicrobial silver nanoparticles – regulatory situation in the European Union. *Mater. Today Proc.* **4**, S200–S207 (2017).

5. Epstein, M. *et al. Scientific Committee on Emerging and Newly Identified Health Risks SCENIHR Opinion on Nanosilver: safety, health and environmental effects and role in antimicrobial resistance*. (2014). doi:10.2772/76851

6. Bouwmeester, H. *et al.* Review of health safety aspects of nanotechnologies in food production. *Regul. Toxicol. Pharmacol.* **53**, 52–62 (2009).

7. Washington, D. C. S. and R. A. D. *Reference Dose for Chronic Oral Exposure of Silver. CASRN 7440-22-4. US Environmental Protection Agency* (1991).

8. Chang, A. L. S., Khosravi, V. & Egbert, B. A case of argyria after colloidal silver ingestion. *J. Cutan. Pathol.* **33**, 809–811 (2006).

9. Johnston, H. J. *et al.* A review of the in vivo and in vitro toxicity of silver and gold particulates: Particle attributes and biological mechanisms responsible for the observed toxicity. *Crit. Rev. Toxicol.* **40**, 328–346 (2010).

10. Trop, M. *et al.* Silver-coated dressing acticoat caused raised liver enzymes and argyria-like symptoms in burn patient. *J. Trauma* **60**, 648–652 (2006).

11. Agency for Toxic Substances and Disease Registry (ATSDR). *Silver CAS # 7440-22-4 ToxFAQs*. (1999).

12. Singh, C. *et al. NM-Series of Representative Manufactured Nanomaterials Characterisation and Test Item Preparation*. (2011). doi:10.2787/55008

13. Stepien, K. M., Morris, R., Brown, S., Taylor, A. & Morgan, L. Unintentional silver intoxication following self-medication: an unusual case of corticobasal degeneration. *Ann. Clin. Biochem.* **46**, 520–522 (2009).

14. León-Silva, S., Fernández-Luqueño, F. & López-Valdez, F. Silver Nanoparticles (AgNP) in the Environment: a Review of Potential Risks on Human and Environmental Health. *Water. Air. Soil Pollut.* **227**, (2016).

15. Lansdown, A. B. G. *Silver in Healthcare: Its Antimicrobial Efficacy and Safety in Use*. *Biofunctional Textiles and the Skin* **33**, (2006).

16. Harris, D. & Robinson, J. R. Drug Delivery via the Mucous Membranes of the Oral Cavity. *J. Pharm. Sci.* **81**, 1–10 (1992).

17. Wertz, P. W. & Squier, C. A. Cellular and molecular basis of barrier function in oral epithelium. *Crit. Rev. Ther. Drug Carrier Syst.* **8**, 237–269 (1991).

18. Lesch, C. A., Squier, C. A., Cruchley, A., Williams, D. M. & Speight, P. The Permeability of Human Oral Mucosa and Skin to Water. *J. Dent. Res.* **68**, 1345–1349 (1989).

19. Fox, C. L. & Modak, S. M. Mechanism of Silver Sulfadiazine Action on Burn Wound Infections.

Antimicrob. Agents Chemother. **5**, 582 LP – 588 (1974).

20. Roblegg, E. *et al.* Evaluation of a physiological in vitro system to study the transport of nanoparticles through the buccal mucosa. *Nanotoxicology* **6**, 399–413 (2012).

21. Mauro, M. *et al.* In vitro permeability of silver nanoparticles through porcine oromucosal membrane. *Colloids Surfaces B Biointerfaces* **132**, 10–16 (2015).

22. Quadros, M. E. *et al.* Release of silver from nanotechnology-based consumer products for children. *Environ. Sci. Technol.* **47**, 8894–8901 (2013).

23. Tang, S. *et al.* Health implications of engineered nanoparticles in infants and children. *World J. Pediatr.* **11**, 197–206 (2015).

24. Fröhlich, E. & Roblegg, E. Oral uptake of nanoparticles: human relevance and the role of in vitro systems. *Arch. Toxicol.* **90**, 2297–2314 (2016).

25. Tulve, N. S. *et al.* Characterization of silver nanoparticles in selected consumer products and its relevance for predicting children's potential exposures. *Int. J. Hyg. Environ. Health* **218**, 345–357 (2015).

26. Adams, D. Penetration of water through human and rabbit oral mucosa in vitro. *Arch. Oral Biol.* **19**, 865-IN11 (1974).

27. Bergman, S., Siegel, I. A. & Ciancio, S. Absorption of Carbon-14 Labeled Lidocaine through the Oral Mucosa. *J. Dent. Res.* **47**, 1184 (1968).

28. Mitrano, D. M. *et al.* Tracking dissolution of silver nanoparticles at environmentally relevant concentrations in laboratory, natural, and processed waters using single particle ICP-MS (spICP-MS). *Environ. Sci. Nano* **1**, 248–259 (2014).

29. Lee, W. W. & Chan, W. T. Calibration of single-particle inductively coupled plasma-mass spectrometry (SP-ICP-MS). *J. Anal. At. Spectrom.* **30**, 1245–1254 (2015).

30. Mitrano, D. M. *et al.* Silver nanoparticle characterization using single particle ICP-MS (SP-ICP-MS) and asymmetrical flow field flow fractionation ICP-MS (AF4-ICP-MS). *J. Anal. At. Spectrom.* **27**, 1131–1142 (2012).

31. Dimitrova, N. *et al.* Public Access NIH Public Access. *PLoS One* **32**, 736–740 (2017).

32. Lee, S. *et al.* Nanoparticle size detection limits by single particle ICP-MS for 40 elements. *Environ. Sci. Technol.* **48**, 10291–10300 (2014).

33. Dan, Y., Shi, H., Stephan, C. & Liang, X. Rapid analysis of titanium dioxide nanoparticles in sunscreens using single particle inductively coupled plasma–mass spectrometry. *Microchem. J.* **122**, 119–126 (2015).

34. Laborda, F., Jiménez-Lamana, J., Bolea, E. & Castillo, J. R. Critical considerations for the determination of nanoparticle number concentrations, size and number size distributions by single particle ICP-MS. *J. Anal. At. Spectrom.* **28**, 1220–1232 (2013).

35. Montaño, M. D., Olesik, J. W., Barber, A. G., Challis, K. & Ranville, J. F. Single Particle ICP-MS: Advances toward routine analysis of nanomaterials. *Anal. Bioanal. Chem.* **408**, 5053–5074 (2016).

36. Murphy, K. E., Liu, J., Montoro, A. R., Johnson, B. M. E. & Winchester, M. R. Characterization of nanoparticle suspensions using single particle inductively coupled plasma mass spectrometry. *NIST Spec. Publ.* 1200–21 (2011). doi:10.6028/NIST.SP.1200-21

37. PerkinElmer, I. Single Particle Inductively Coupled PlasmaMass Spectrometry: Understanding How and Why. 1–5 (2014).

38. Degueldre, C., Favarger, P. Y. & Wold, S. Gold colloid analysis by inductively coupled plasma-mass spectrometry in a single particle mode. *Anal. Chim. Acta* (2006). doi:10.1016/j.aca.2005.09.021

39. Merrifield, R. C., Stephan, C. & Lead, J. R. Single-particle inductively coupled plasma mass spectroscopy analysis of size and number concentration in mixtures of monometallic and bimetallic (core-shell) nanoparticles. *Talanta* **162**, 130–134 (2017).

40. Pace, H. E. *et al.* Determining transport efficiency for the purpose of counting and sizing nanoparticles via single particle inductively coupled plasma mass spectrometry. *Anal. Chem.* **83**, 9361–9369 (2011).

41. Hadioui, M., Wilkinson, K. & Stephan, C. Assessing the Fate of Silver Nanoparticles in Surface Water using Single Particle ICP-MS. *ICP-MS Appl. note* 3–8 (2014).

42. Merrifield, R. C., Stephan, C. & Lead, J. Determining the Concentration Dependent Transformations of Ag Nanoparticles in Complex Media: Using SP-ICP-MS and Au@Ag Core-Shell Nanoparticles as Tracers. *Environ. Sci. Technol.* **51**, 3206–3213 (2017).

43. Donovan, A. R. *et al.* Single particle ICP-MS characterization of titanium dioxide, silver, and gold nanoparticles during drinking water treatment. *Chemosphere* **144**, 148–153 (2016).

44. Nicolazzo, J. A., Reed, B. L. & Finnin, B. C. The Effect of Various In Vitro Conditions on the Permeability Characteristics of the Buccal Mucosa. *J. Pharm. Sci.* **92**, 2399–2410 (2003).

45. Lestari, M. L. A. D., Nicolazzo, J. A. & Finnin, B. C. A Novel Flow through Diffusion Cell for Assessing Drug Transport across the Buccal Mucosa In Vitro. *J. Pharm. Sci.* **98**, 4577–4588 (2009).

46. Franz, T. J. Percutaneous Absorption. On the Relevance of in Vitro Data. *J. Invest. Dermatol.* **64**, 190–195 (1975).

47. Blosi, M., Albonetti, S., Dondi, M., Martelli, C. & Baldi, G. Microwave-assisted polyol synthesis of Cu nanoparticles. *J. Nanoparticle Res.* **13**, 127–138 (2011).

48. Burns, D. A., Breathnach, S. M., Cox, N. & Griffiths, C. E. *Rook's Textbook of Dermatology*. *Rook's Textbook of Dermatology* **1**–**4**, (Blackwell Publishing, 2004).

49. Bearer, C. F. How are children different from adults? *Environ. Health Perspect.* **103**, 7–12 (1995).

50. Park, E.-J., Yi, J., Kim, Y., Choi, K. & Park, K. Silver nanoparticles induce cytotoxicity by a Trojan-horse type mechanism. *Toxicol. Vitr.* **24**, 872–878 (2010).

51. Gardini, D. *et al.* Nanosilver: An innovative paradigm to promote its safe and active use. *NanoImpact* **11**, 128–135 (2018).

4. Fate in environmental model

For what concern environmental scenario, my research was focused on two main exposure media: the fresh water and the marine ecosystems, representing, respectively, lakes / rivers and sea / oceans. NMs behavior within different environmental compartments – associated to release, transportation and transformation processes– is really challenging, due to the wide range of exposure conditions and routes.

One of the main goal in the risk assessment is to define exactly how (form), when (changes in function of time) and where (spreading in the water compartments) NMs are[1]. To reach this goal a complete physiochemical characterization in requested, providing info about the intrinsic properties of NMs and their system-dependent properties once dispersed in the water medium.

For environmental exposure, we selected three case studies and analyzed the intrinsic characteristic of NMs - such as shape, size dimension and superficial charge - and their behaviour in water compartment in absence of microorganism, evaluating dissolution, aggregation and sedimentation processes.

Two metal oxide NPs were selected, titanium dioxide nanoparticles (TiO_2 NPs) and cerium dioxide nanoparticles (CeO_2 NPs), belonging to reactive group (Figure 2.1) and being almost insoluble in environmental conditions. As comparison a partially soluble NMs[2,3], zinc oxide nanoparticles (ZnO NPs) were also investigated.

In agreement with OECD guidelines, Elendt M7 was applied for fresh water compartments, mimicking the life condition for *Daphnia magna* speciem[4,5,6]. Egg Water medium was used for the sea water ecosystem, usually applied in *in-vivo* test on *Zebrafish (Danio rerio)* species.

Both *Daphnia magna* and *Zebrafish* species are *in-vivo* models[5,7–9], used to predict the final adverse outcome of NMs in water compartments and provide risk assessment information as median effective concentrations (EC_{50}) and calculate PNEC values[10].

The experimental testing strategy reported in Figure 4.1.

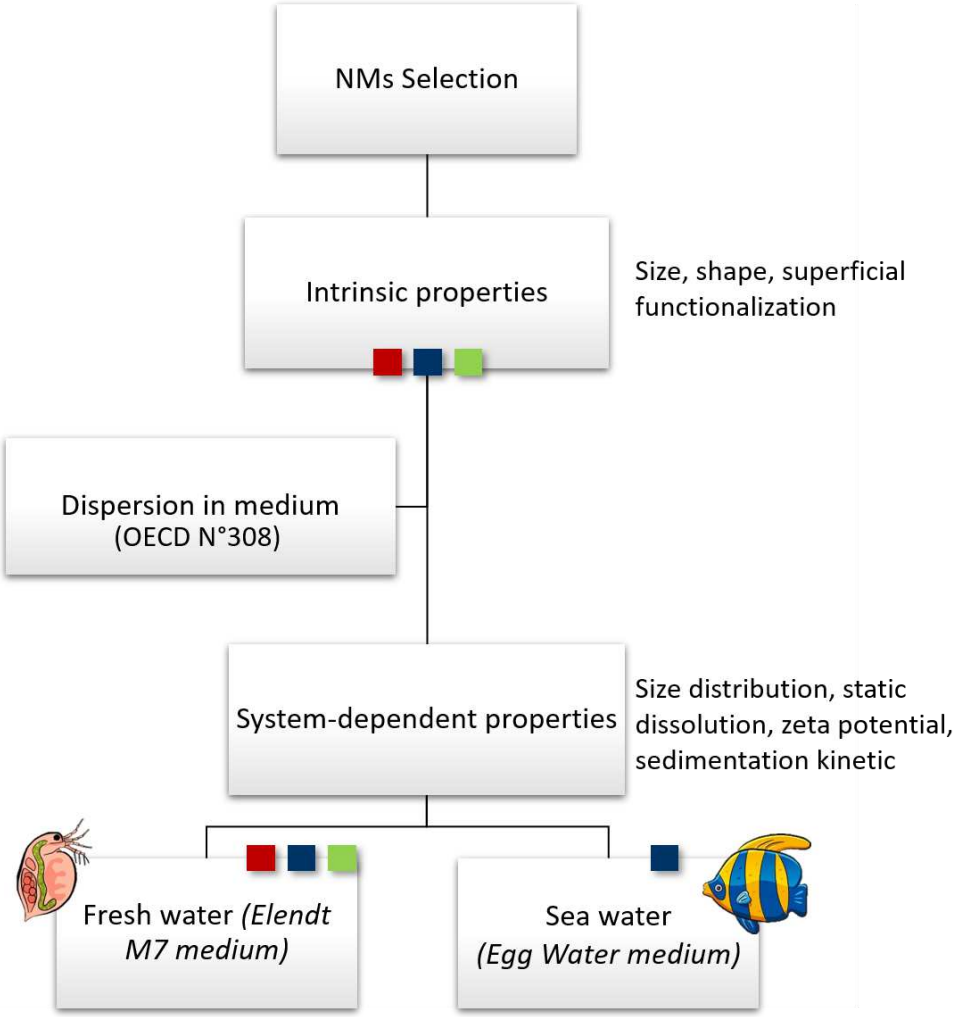

Figure 4.1: Experimental design strategy for the environmental related case studies of (■) ZnO NPs, (■) TiO_2 NPs and (■) CeO_2 NPs.

References

1. Gottschalk, F. & Nowack, B. The release of engineered nanomaterials to the environment. *J. Environ. Monit.* **13**, 1145–1155 (2011).

2. Arts, J. H. E. *et al.* A decision-making framework for the grouping and testing of nanomaterials (DF4nanoGrouping). *Regul. Toxicol. Pharmacol.* **71**, S1–S27 (2015).

3. Arts, J. H. E. *et al.* Case studies putting the decision-making framework for the grouping and testing of nanomaterials (DF4nanoGrouping) into practice. *Regul. Toxicol. Pharmacol.* **76**, 234–261 (2016).

4. Samel, A., Ziegenfuss, M., Goulden, C. E., Banks, S. & Baer, K. N. Culturing and Bioassay Testing ofDaphnia magnaUsing Elendt M4, Elendt M7, and COMBO Media. *Ecotoxicol. Environ. Saf.* **43**, 103–110 (1999).

5. Häder, D.-P. & Erzinger, G. S. OECD Guidelines for tetsing of chemicals - Daphnia magna Reproduction Test. *OECD* 1–21 (1998). doi:10.1016/B978-0-12-811861-0.00011-5

6. OECD. Test No. 308: Aerobic and Anaerobic Transformation in Aquatic Sediment System. *OECD Guidel. Test. Chem.* 19 (2002). doi:10.1787/9789264070523-en

7. OCDE. OCDE Test 202 Acute Immobilization in D. magna. 1–12 (2004).

8. Lin, S., Lin, S., Zhao, Y. & Nel, A. E. Zebrafish: An in vivo model for nano EHS studies. *Small* **9**, 1608–1618 (2013).

9. Agency, E. Environment Agency The direct toxicity assessment of aqueous environmental samples using the juvenile. *Envrironmental Agency* (2007).

10. ChemSafetyPro. Aquatic Toxicity - Environmental Risk Assessment. *www.chemsafetypro.com* (2019).

4.1 Zinc oxide nanoparticles in fresh water compartment

Introduction

Zinc oxide nanoparticles (ZnO NPs) are produced on a large scale and are one of the more produced NPs in the world. They have been applied in different sectors and extensively used in food packaging, cosmetics, agriculture, biomedical and UV-absorbers applications[1–5]. As for others NPs, also ZnO NPs present evidence of some toxicity against specific aquatic organisms, such as juvenile carp (*Cyprinus carpio*) and daphnia (*Daphnia magna*)[6,7], and human compartments (lung and liver cell cultures)[8–10]. ZnO NPs belong to partially soluble group in DF4nanoGrouping, with possible adverse effects associated to the dissolved ions released from NPs. The evaluation of contribution that both NPs and ions can give to toxicity is a crucial step in the assessment and management of the possible NPs adverse effects.

Specifically, in this case study, we select, as exposure medium, fresh water compartment, evaluating, in absence of microorganism, the behavior of two different kind of ZnO NPs. The selection of fresh water compartment, is justified by potential effects that the use of ZnO NPs in agriculture and in food packaging applications can cause. While the two ZnO NPs selected. The two ZnO NPs: NM-110 and NM-111, are reference materials provided by JRC, applied within the EU H2020 PATROLS PATROLS (N° 760813) and present different surface functionalization, being, respectively, uncoated and coated with triethoxycarpryl silane ($C_{14}H_{32}O_3Si$)[11].

Thus, the aim of this work was that to provide physiochemical descriptors for ZnO NPs, able to support the exposure assessment in ecotoxicological relevant media and a further implementation of *in-silico* models for risk characterization. We analysed the size distribution by DLS (d_{DLS}) and surface charge (Zeta Potential - ζ- pot_{ELS}) by ELS analysis. The static dissolution within media was also measured using ultrafiltration (UF) process and ICP-OES analysis to calculate the fraction of $Zn^{2+}_{dissolved}/Zn_{total}$ and so the contributes that NPs and ions can have in the pathway of possible adverse effect.

Experimental part

Materials. ZnO NPs, naked JRCNM62101a (NM-110) and coated JRCNM01101a (NM-111), were provide as nano-powders by JRC in Ispra (Italy)[11] and analyzed within the framework of European Project PATROLS (N°. 760813). Nitric acid (65%) was purchased from Titolchimica

S.p.A. (Italy). Zn standard for ICP-OES measurements was purchased by Sigma-Aldrich, Milan (Italy). All the Elendt M7 medium salts were purchased from Sigma-Aldrich, Milan (Italy); their approximate composition in mg L^{-1} is 0.715 H_3BO_3, 0.090 $MnCl_2*4H_20$, 0.078 LiCl, 0.018 RbCl, 0.040 SrCl2*6H_20, 0.004 NaBr, 0.017 $Na_2MoO_4*2H_2O$, 0.005 $CuCl_2*2H_2O$, 0.015 $ZnCl_2$, 0.012 $CoCl_2*2H_2O$, 0.004 KI, 0.003 Na_2SeO_3, 0.001 NH_4VO_3, 1.250 $Na_2EDTA*2H_20$, 0.498 $FeSO_4*7H20$, 293.800 $CaCl_2*2H_2O$, 123.300 $MgSO_4*7H_20$, 5.800 KCl, 64.800 $NaHCO_3$, 10.000 $Na_2SiO_2*9H_20$, 0.274 $NaNO_3$, 0.143 KH_2PO_4, 0.184 K_2HPO_4.

Preparation of suspensions. Following PATROLS Guidance Document 2 (source: NanoReg dispersion protocol[12,13,14]), we prepared and measured suspensions reported in Scheme 4.1.1. We prepared a concentrated two stocks in MilliQ water plus EDTA (samples 1 and 5, respectively at 2560 and 100 mg L^{-1}). We used EDTA instead of NOM, for improving NPs dispersability, because is more available and it is a component of the medium. We diluted the stock in pure MilliQ at 100 mg L^{-1} (samples 2) or in Elendt M7 medium, exposing them at 22°C for 1h and 72h, mimicking long-term exposure conditions. We evaluated hydrodynamic diameter by DLS, ZP and dissolved fraction (only in medium), calculated as weight rate of $Zn^{2+}_{dissolved}/Zn_{total}$. We repeated the same analysis in the medium after 72h of incubation at 22°C.

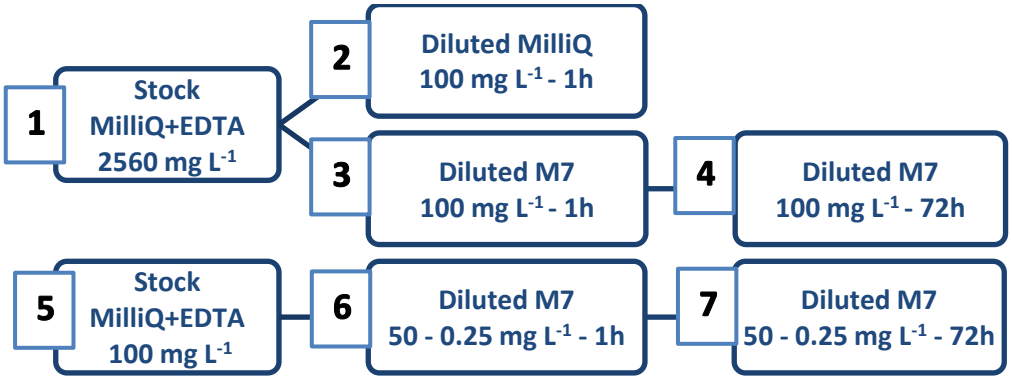

Scheme 4.1.1: Exposure conditions used for investigating system-dependent properties.

Intrinsic properties. Morphological characterization of ZnO NPs, naked and coated, was performed by FE-SEM instrument (Carl Zeiss Sigma NTS Gmbh, Oberkochen, DE), coupled with STEM detector. One drop of the ZnO stock suspensions diluted in MilliQ water (100 mg L^{-1}) was deposited on a film-coated copper grid and then dried in air. Difference between ZnO naked and coated NPs was evaluated using infrared spectrophotometry with attenuated total reflectance Fourier-transform infrared - Attenuated total reflection spectroscopy (FTIR-ATR) analysis (Nicolet iS5 spectrometer - Thermo Fisher Scientific Inc., Waltham, MA, USA), with a resolution of 2 cm^{-1} by accumulation of 64 scans, covering the 4000 to 400 cm^{-1} range and using a diamond ATR accessory model iD7, and thermo-gravimetric technique (TG) (STA 449C,

Netzsch-Gerätebau GmbH, Selb/Bavaria, Germany), using a ramp of 10°C min^{-1} till 800° C in air flux.

System-dependent properties. Hydrodynamic size distribution and ZP measurements of the nano-suspensions were carried out with a DLS / ELS (dynamic light scattering and electrophoretic light scattering Zetasizer Nano instrument ZSP, ZEN5600, Malvern Instruments, UK) both in MilliQ water and in Elendt M7 medium. Titrations of ZP vs pH were also performed with automatic titration, using 1M KOH and 1M HCl to change the pH, so providing indication on the isoelectric point (IEP) that corresponds to the pH value where ZP is neutralized.

Static dissolution measurements were made to assess the release of Zn^{2+} from ZnO NPs. Samples prepared at different exposure conditions were filtered through 10kDa molecular weight cut-off membranes (5000 rpm for 40 min) and the filtrated solution analyzed by ICP-OES (ICP-OES 5100—vertical dual view apparatus - Agilent Technologies, Santa Clara, CA, USA). The analysis was performed in axial viewing mode, and calibration curves were obtained with 0.1, 1.0, 10.0, 100.0 and 200.0 mg L^{-1} standards for Zn element. Nitric acid was added both to standards and to diluted samples (1:10 v/v). The concentration of Zn^{2+} in washing water was directly evaluated by ICP-OES Zn determination. Calibration curve was evaluated and showed a good correlation, coefficient (R^2) above 0.99. Results from ICP-OES were reported as the average of three independent measurements with RSD %.

Results and discussion

Intrinsic properties

As reported in literature, the main difference between these two NPs is the different coating[11]. ZnO NM-110 are naked and preserve their native chemistry at the surface, while ZnO NM-111 are coated by a triethoxycarpryl silane coating ($C_{14}H_{32}O_3Si$), that functionalizes the surface of ZnO NPs. In the framework of risk characterization, the first issue to address is “what NPs are”[15,16], in terms of composition, surface chemistry and morphology.

The morphology of ZnO NM-110 and ZnO NM-111 is reported in Figure 4.1.1. As expected, the FE-SEM images did not show appreciable differences, between coated and uncoated samples. Both the NPs result highly agglomerated and aggregated, presenting a prisma shape of different dimension - from 10 nm to 500 nm - with a large variation in morphology (size and geometry) of nanostructures. The irregular morphology of observed samples is a typical of NPs obtained for mechano-chemical process[2,3], that can more easily

produce surface defects able to induce an higher reactivity (as dissolution and pro-oxidative potential), if compared with wet-chemical processes.

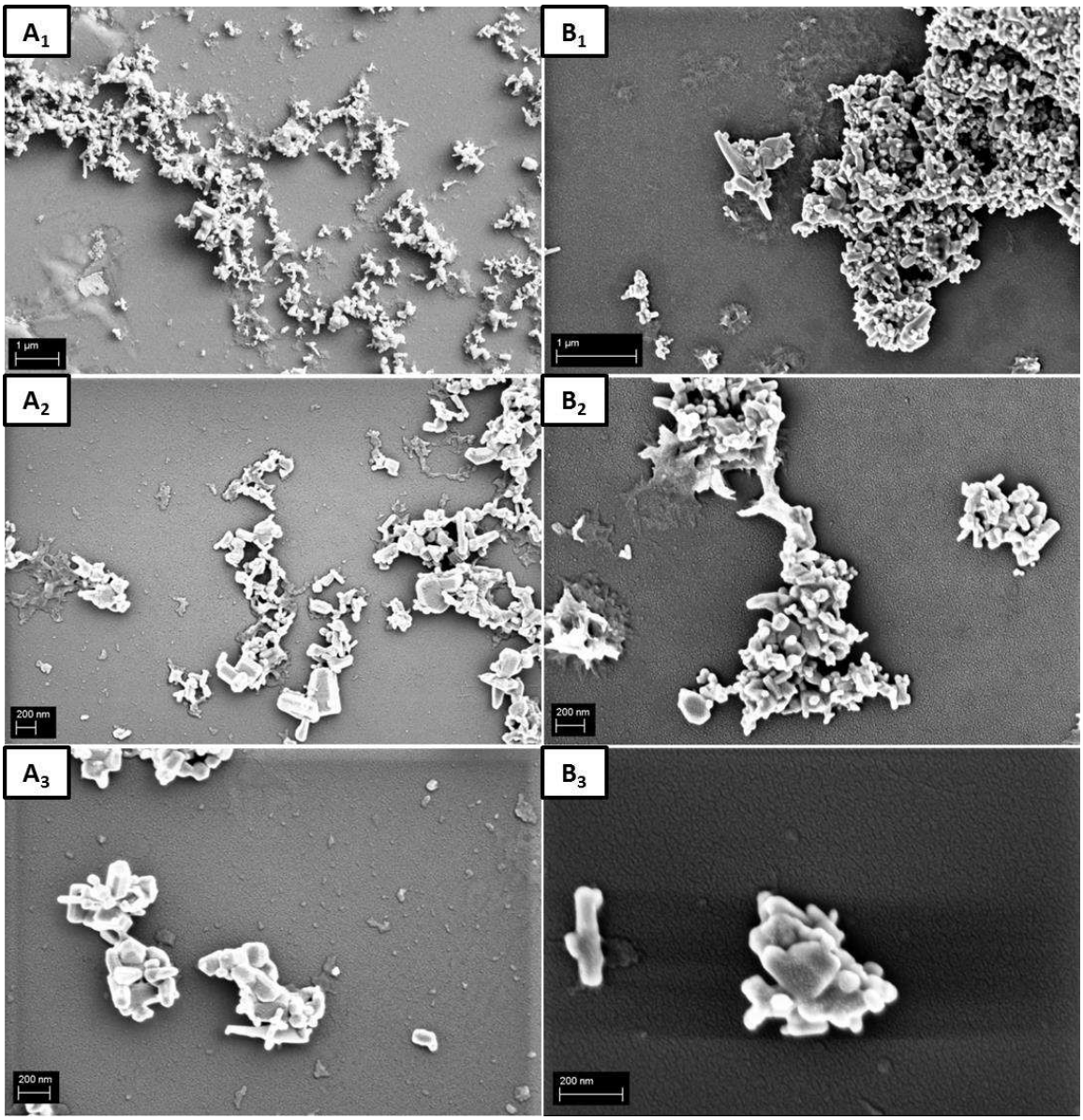

Figure 4.1.1: FE-SEM images of ZnO NM-110 (A, 1 – 2 – 3) and ZnO NM-111 (B, 1 – 2 – 3).

FTIR-ATR analysis spectra reported in Figure 4.1.2 did not show significant differences in the finger print area below 2000 cm^{-1}. The low amount of coating present in NM-111 (ca. 1% referred to dry powder[11]) doesn't seem to modify significantly also the surface chemistry.

The presence of the low amount of coating was confirmed by TG analysis, that showed a weight loss of ca. 0,65% for ZnO NM-111 (Figure 4.1.3).

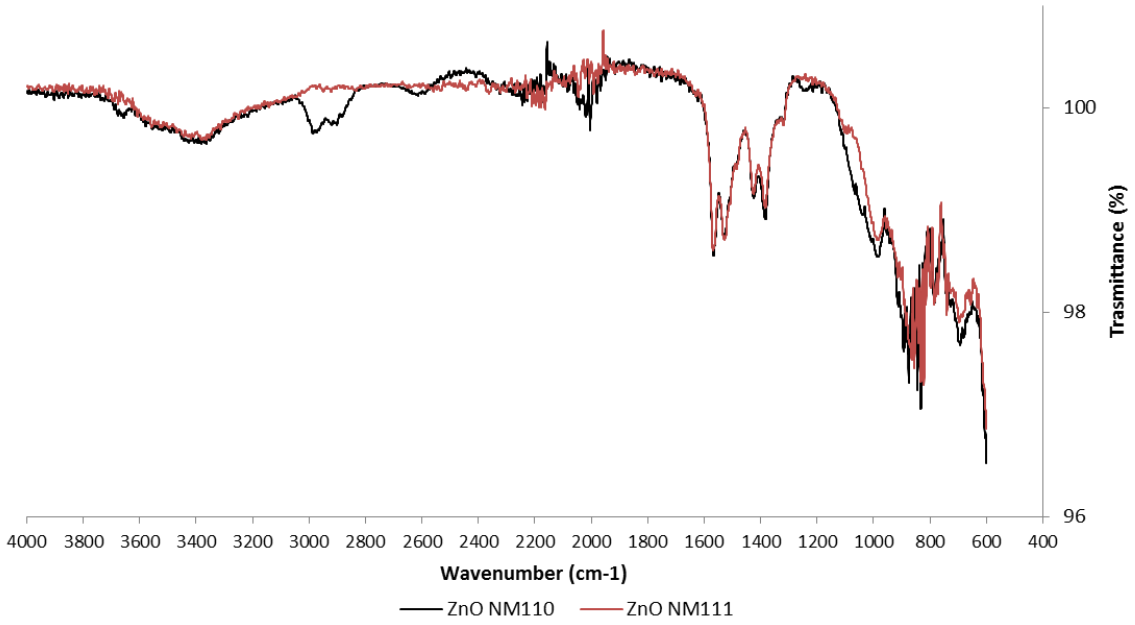

Figure 4.1.2: FTIR-ATR analysis of ZnO NM-110 and NM-111 nano-powders.

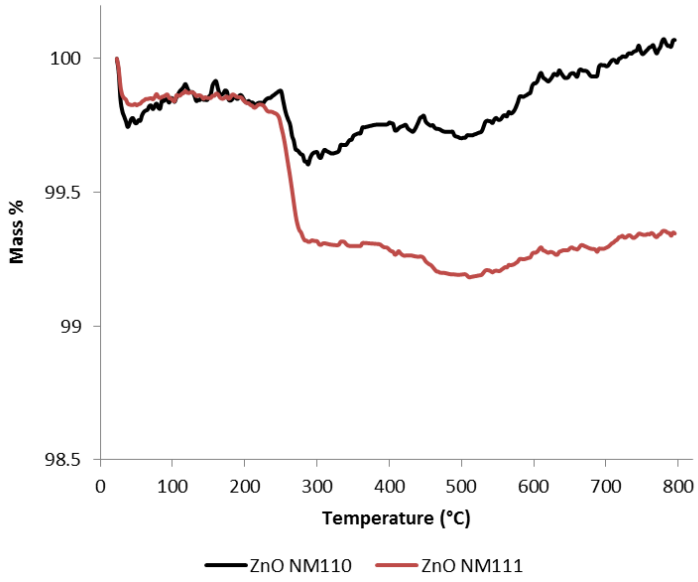

Figure 4.1.3: TG analysis of necked NM-110 and coated NM-111 nano-powders.

System-dependent properties

To define physicochemical identity in support to risk assessment further two questions should be addressed: "where NPs go" and "what NPs do"[15,16]. For this reason, we investigated the colloidal stability (hydrodynamic size distribution and ZP) and dissolution (ionic fraction released), once ZnO NPs enter in relevant media.

Colloidal stability:

In the following tables the DLS size (d_{DLS}) and ZP (ζ-pot_{ELS}) of samples schematized in Scheme 4.1.1, are reported.

Table 4.1.1: DLS and ELS measurements for NM-110.

Sample	pH	d_{DLS} (nm) (rsd %)	PDI (rsd %)	ζ-pot_{ELS} (mV) (rds %)
1	7.1	1896 (33)	0.776 (25)	15.9 (3)
2	7.2	2183 (30)	0.879 (13)	8.6 (7)
3	8.2	3224 (40)	0.612 (14)	-7.1 (3)
4	8.0	3816 (39)	0.582 (32)	-8.0 (8)
5	7.6	299 (6)	0.356 (14)	23.3 (3)
6 (5 mg L^{-1})	8.5	2278 (18)	0.998 (0.1)	-10.0 (2)
7 (5 mg L^{-1})	7.8	2651 (25)	0.966 (6)	-13.3 (1)

The stock (1), prepared following NanoReg protocol[12,13], and samples, diluted from it (2, 3, 4), are very unstable. Their size is bigger than 1500 nm, with high polydispersion and can be observed big aggregates, falling down in few minutes within the experimental vessel. The ZP changes from positive to negative, passing through the Stock dispersion to the samples diluted in Elendt M7, probably due to specific adsorption on NPs surfaces of anionic salts (sulphate, phosphate, etc…). The stock at 100 mg L^{-1} (5) present data closer to those reported in literature[11,17]. So, we suggest to prepare the stock at this concentration in order to obtain a more stable system, suitable for further observation. Nevertheless, at the low concentration of samples diluted in Elendt M7 (6 and 7), DLS data are not reliable, due to the very high attenuation coefficient observed (9).

Table 4.1.2: DLS and ELS measurements for NM-111.

Sample	pH	d_{DLS} (nm) (rsd %)	PDI (rsd %)	ζ-pot_{ELS} (mV) (rds %)
1	7.1	4825 (32)	0.578 (19)	12.2 (6)
2	7.4	4789 (33)	0.826 (19)	4.3 (23)
3	7.9	3780 (36)	0.819 (29)	-10.7 (10)
4	7.7	4013 (58)	0.759 (34)	-17.1 (6)
5	7.5	582 (6)	0.626 (20)	11.6 (3)
6 (5 mg L^{-1})	7.5	1966 (19)	0.684 (15)	-9.1 (9)
7 (5 mg L^{-1})	7.6	5046 (46)	1.000 (0)	-12.5 (4)

Also in the case of coated ZnO NPs, the concentrated stock (1) and samples, diluted from it (2, 3, 4) show a high instability with high degree of agglomeration and size in the micrometric range. The ZP changes from positive to negative, passing in diluted Elendt M7 suspensions for the expected adsorption on the surface of anionic salts (sulphate, phosphate). As observed for naked NPs, DLS and ZP, in line with literature data[11,17], are obtained only for diluted stock in water (5), that show the minimal stability suitable for further observation.

In the Tables below we report DLS diameter and ZP of samples 6 and 7 in a range of concentration from 100 to 0,25 mg L^{-1}, after 1 and 72h of exposure in Elendt M7, mimicking long term exposure conditions.

Table 4.1.2: DLS and ELS measurements for NM-110 in Elendt M7.

Concentration (mg L^{-1})	Incubation time (h)	d_{DLS} (nm) (rsd %)	PDI (rsd %)	ζ-pot_{ELS} (mV) (rsd %)
100	1	3224 (1284)	0.610 (0.090)	-7.1 (0.2)
	72	4105 (1493)	0.580 (0.190)	-7.9 (0.6)
50	1	3333 (394)	0,400 (0,060)	-7.9 (0.5)
	72	3392 (703)	0.400 (0.070)	-7.4 (0.6)
10	1	813 (64)	0.570 (0.070)	-18.2 (0.6)
	72	2052 (324)	0.850 (0.150)	-17.9 (0.1)
5	1	1012 (130)	0.690 (0.100)	-18.0 (0.3)
	72	2477 (391)	0.900 (0.090)	-18.2 (0.4)
2.5	1	1466 (150)	0.770 (0.120)	-19.8 (0.8)
	72	2073 (885)	0.800 (0.140)	-19.4 (0.9)
0.25	1	2614 (319)	0.360 (0.180)	-19.2 (0.4)
	72	2676 (509)	0.690 (0.210)	-17.5 (0.3)

Table 4.1.3: DLS and ELS measurements for NM-111 in Elendt M7.

Concentration (mg L^{-1})	Incubation time (h)	d_{DLS} (nm) (rsd %)	PDI (rsd %)	ζ-pot_{ELS} (mV) (rsd %)
100	1	3780 (1364)	0.820 (0.240)	-10.7 (1.1)
	72	3784 (2275)	0.760 (0.260)	-17.1 (1.0)
50	1	2088 (336)	0.840 (0.180)	-9.5 (0.7)
	72	3624 (1643)	0.980 (0.040)	-12.9 (0.6)
10	1	1576 (173)	0.580 (0.160)	-17.7 (0.6)
	72	2306 (332)	0.730 (0.170)	-17.1 (0.3)
5	1	1732 (571)	0.760 (0.210)	-19.4 (0.4)
	72	816 (78)	0.510 (0.090)	-17.7 (0.5)
2.5	1	825 (103)	0.610 (0.150)	-18.9 (1.1)
	72	591 (50)	0.520 (0.040)	-17.7 (0.5)
0.25	1	2486 (685)	0.520 (0.340)	-19.2 (0.3)
	72	2448 (330)	0.300 (0.210)	-20.2 (0.5)

At all investigated concentration and time of exposure we observe a high agglomeration degree with the formation of micro-aggregates, even at low concentrations, despite ZP values (> -15mV) should provide an electrostatic stabilisation. For NM-110 NPs after 72h of incubation for all concentrations, an increase in size distribution occurs as an increase of PDI index. The NM-110 NPs in Elendt M7 tend to aggregate and precipitate along the water-column in function of time. Although, this colloidal behavior is not confirmed by NM-111 NPs for all concentration, but only above 10 mg L^{-1}. Below 5 mg L^{-1}, this trend is inversed and NM-111 NPs seem to be more dispersed after 72h of exposure, we observed a reduction in size distribution and PDI. For what concern ZP, below 10 mg L^{-1} we have a nearly constant value for both NPs types (ca. -18 mV). The ZP values change from positive to negative, passing through the stock dispersion value (positively charged) to the samples diluted in Elendt M7 (negatively charged), probably due to

specific adsorption on NPs surfaces of anionic salts that are present in Elendt M7, such as phosphate[18,19].

To better understand the pH effect on colloidal stability, we considered samples dispersed in water and Elendt M7 for 1h (samples 2 and 3 of Scheme 4.1.1) and performed ZP titration as a function of pH. We measured and compared the isoelectric point (IEPs), pH where ZP is neutralized[20], of naked (Figure 4.1.5) and coated NPs (Figure 4.1.7), in MilliQ water and Elendt M7, getting information on NPs surface chemistry, that, after exposure, can become more acid (shift of IEP towards lower pH) or more basic (shift of IEP to higher pH). Looking to ZP vs pH curves in water it can be observed the presence of two IEPs marked with red arrows in the Figures 4.1.5 and 4.1.7. This behavior is typical of surfaces that undergone a strong modification induced by pH change, like for instance dissolution phenomena. In the case of ZnO NPs we make the hypothesis that, immediately after immersion, ZnO NPs surface is hydrolysed with the formation of $Zn(OH)_{2(s)}$ layer. As pH decreases (pH<6) [21,22] surface partially solubilises, releasing Zn^{2+} and $Zn(OH)^{+}$ ions, which could re-precipitate giving a new solid phase $ZnOx_{(s)}$, that shows a new IEP at low pH [21,22], together with a reduced hydrodynamic size (Figure 4.1.6).

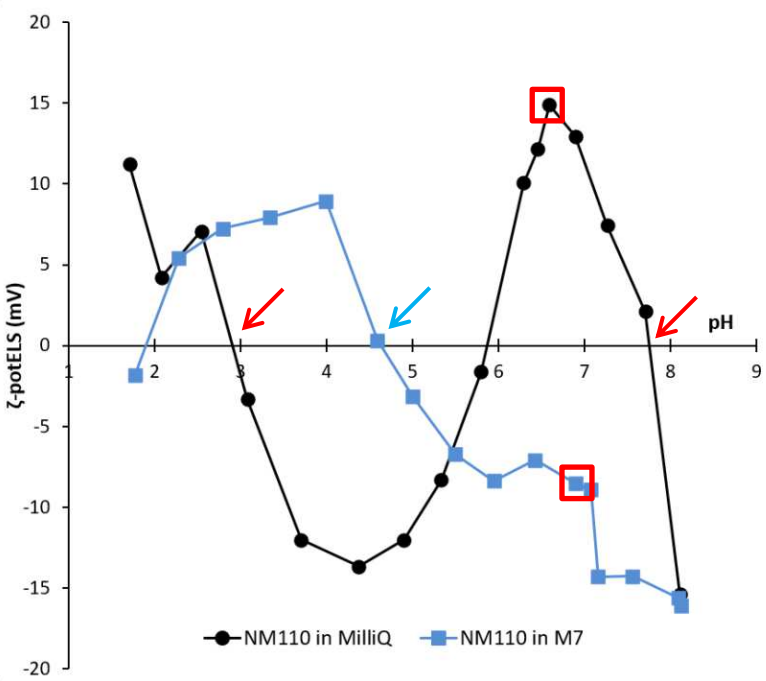

Figure 4.1.5: Zeta Potential (mV) vs pH plot of ZnO NM-110 MilliQ (●) and Elendt M7 (■) media (nanosol; ◘ natural pH, IEPs red arrow for MilliQ (→) and blue arrow for Elendt M7(→)).

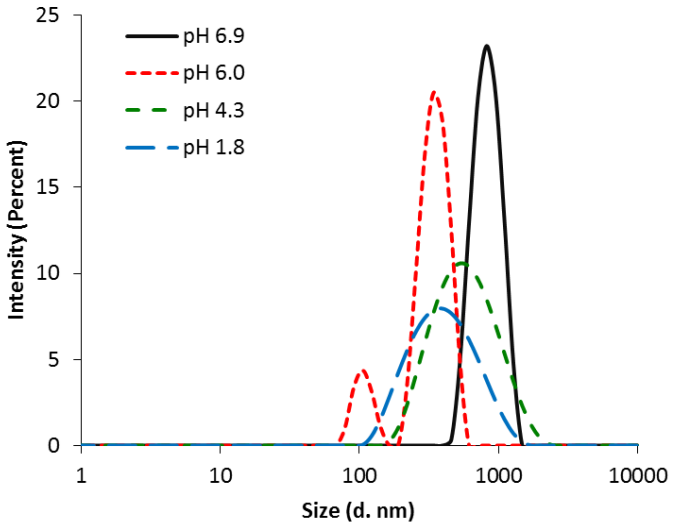

Figure 4.1.6: Size distribution of ZnO NM-110 MilliQ medium at different pH (- 6.9, - 6.0, - 4.3, - 1.8).

The same behaviour was observed also with ZnO NM-111 NPs, where the ZP positive values lies between pH 6.3 and 7.5 in distilled water and shifts in Elendt M7 medium to pH lower than 2.7 for the presence of co-exposed anions (SO_4^{2-}, PO_4^{3-}). The coating presence change the electrophoretic mobility change, shifting and reducing the ZP positive values range and both IEPs.

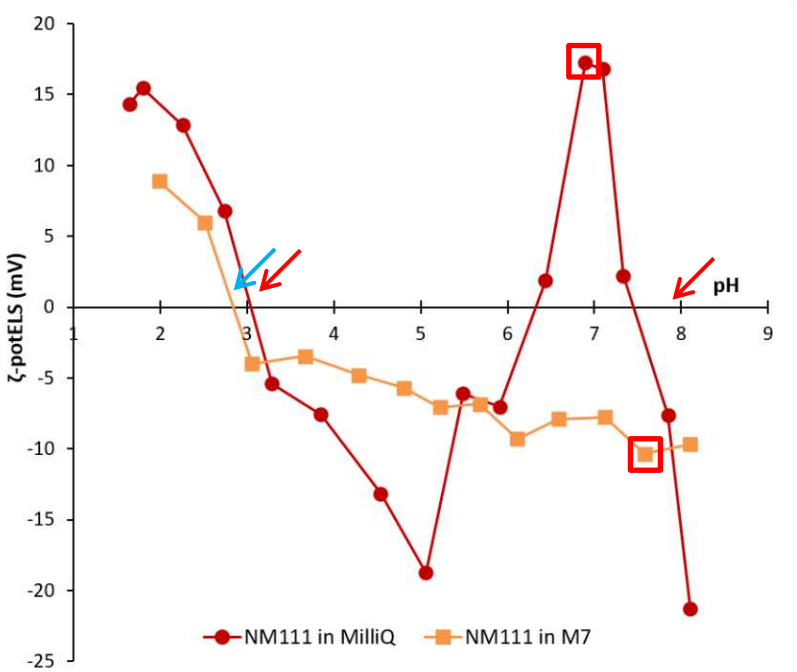

Figure 4.1.7: Zeta Potential (mV) vs pH plot of ZnO NM-111 MilliQ (●) and Elendt M7 (■) media; ◘ natural pH, IEPs red arrow for MilliQ (→) and blue arrow for Elendt M7(→)).

The ELS results show a high instability of water suspensions for both ZnO NPs type. Both NPs present a fluctuation of ZP values between 20 mV and -20 mV once dispersed in water (1<pH<9), presenting a high colloidal instability[23]. Thus, the size dimension observed in DLS analysis (Table 4.1.1 and 4.1.2) confirmed this high instability and agglomeration trend, providing the micro-aggregates formation. Since instability was confirmed in water medium, different behaviour was observed in Elendt M7, where both ZnO NPs present a slightly negative superficial charge. At the pH of 7 in Elendt M7, ZP values are close to -10 mV, so from water to ecotox medium the ZP values change from positive (15 mV) to negative, probably due to medium salts amount.

Static dissolution (quantification of ions released):

A first set of tests were performed to evaluate the dependence of ZnO NPs solubility from pH. The percentage of Zn^{2+}/Zn_{total} in MilliQ water was measured as a function of pH (Figure 4.1.4). At pH below 4.5, no difference occurs between naked and coated NPs, that totally dissolve in acid water. While appreciable difference is observable increasing pH. The presence of triethoxycapryl silane mitigates the release of ions in the pH range 5-7 where a lower concentration of Zn^{2+} was detected, whilst seems having no effect at pH values beyond pH 7, where Zn^{2+} ions releases are negligible. This result is significant because the ZnO NPs naked and coated show a little difference in terms of dissolution only in the central pH region that corresponds to the neutrality of aqueous media used for mimicking environmental exposure scenarios and making ecotox tests.

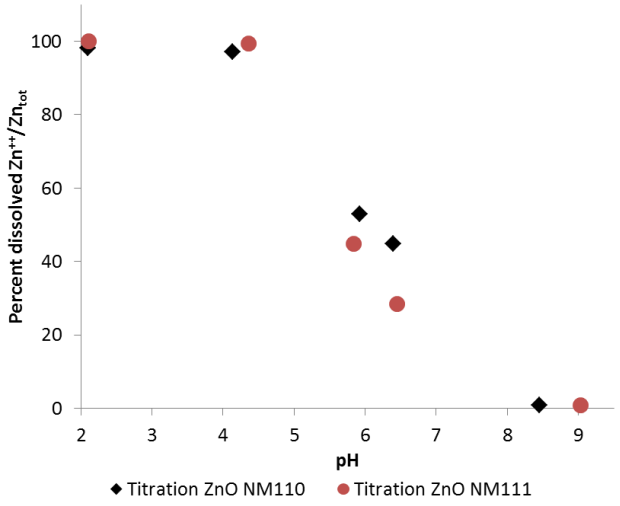

Figure 4.1.4: Dissolution percentage vs pH plot of ZnO NM-110 and NM-111, expressed as percentage of Zn^{2+}/Zn_{total} released in function of pH (nanosol concentration 100 mg L^{-1}).

The contribution of dissolution as a function of starting concentration has been evaluated, measuring the ionic contents of sample 6 and 7 (Scheme 4.1.1) with a concentration range mimicking long exposure conditions in Elendt M7, from 100 to 0,25 mg L^{-1}(Table 4.1.5 and 4.1.6).

What we found is, again, a similar dissolution behavior for both ZnO NPs. Coated ZnO NPs, incubated 1-72h in Elendt M7 medium showed a percentage of free ions of around 10% for 10 mg L^{-1} sample, after 1h of exposure, increasing at around 15% after 72h. The dissolution of uncoated samples seems slightly higher, especially for low sample concentration, even if in both cases the dissolution percentage vs concentration curves reach a plateau and only few units' percentage of ZnO is dissolved, above concentration of 20 mg L^{-1} (Figure 4.1.8 and 4.1.9). It is interesting to observe that, if referring to grouping criteria of DF4nanoGrouping framework[24], NPs fall into Group MG1 (soluble materials) if the concentration of ions is > 100 mg L^{-1}, or in case of samples having a lower initial concentration, if the dissolved percentage mass is > 10%.

So, in the present case, ZnO samples should be assigned to MG1 only at starting concentration below 20 mg L^{-1} for both coated and uncoated samples.

Table 4.1.4: NM-110 dissolution in function of concentration and exposure time, expressed as percentage of Zn^{2+}/Zn_{total}.

Sample conc. (mg L^{-1})	Dissolution 1h (Zn^{2+}/Zn_{total}%)	Dissolution 72h (Zn^{2+}/Zn_{total}%)
0.25	77.4 ± 5.0	83.6 ± 5.0
2.50	30.7 ± 4.3	57.0 ± 3.0
5.00	16.9 ± 3.0	31.0 ± 5.2
10.00	9.6 ± 8.0	17.8 ± 1.0
50.00	3.8 ± 1.0	5.6 ± 3.9
100.00	0.5 ± 0.8	0.7 ± 1.7

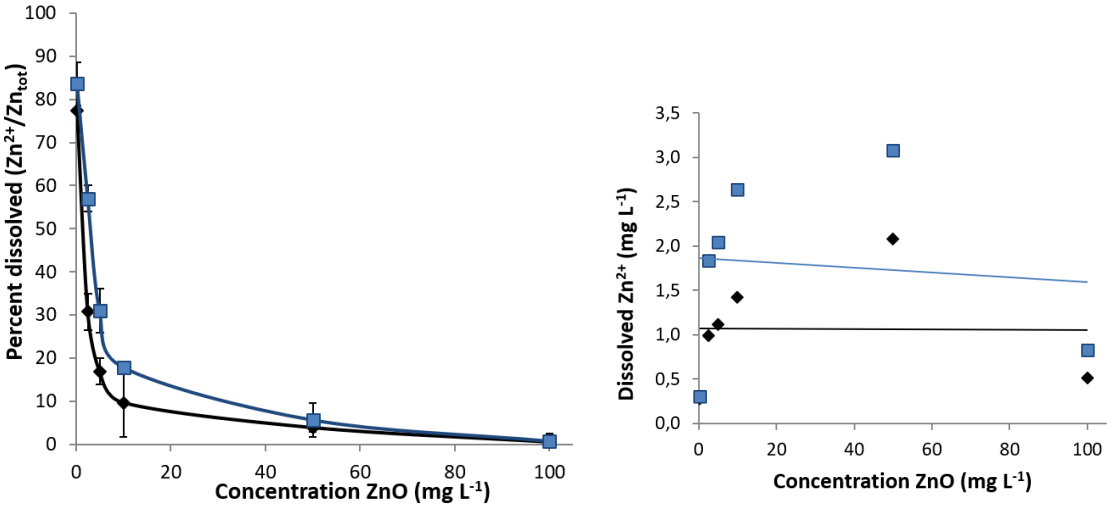

Figure 4.1.8: Dissolution of NM-110 in Elendt M7 expressed as percentage of Zn^{2+} on ZnO $_{total}$ (left) and as concentration of Zn^{2+} released (right) vs ZnO concentration. (respectively referred to ◆ 1h and ■ 72h of exposure)

Table 4.1.5: NM-111 dissolution in function of concentration and exposure time, expressed as percentage of Zn^{2+}/Zn_{total}.

Sample conc. (mg L^{-1})	Dissolution 1h (Zn^{2+}/Zn_{total}%)	Dissolution 72h (Zn^{2+}/Zn_{total}%)
0.25	59.5 ± 5.0	92.0 ± 4.1
2.50	42.3 ± 8.0	61.5 ± 5.0
5.00	25.1 ± 2.3	30.9 ± 3.0
10.00	19.0 ± 2.3	23.4 ± 5.3
50.00	4.6 ± 4.3	4.5 ± 3.5
100.00	1.7 ± 0.7	3.0 ± 1.1

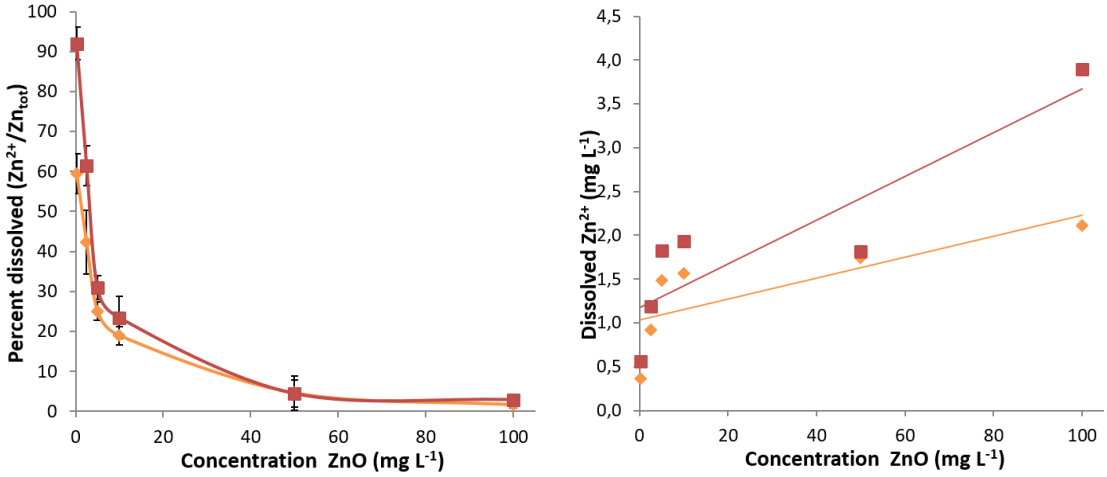

Figure 4.1.9: Dissolution of NM-111 in Elendt M7 expressed as percentage of Zn^{2+} on ZnO $_{total}$ (left) and as concentration of Zn^{2+} released (right) vs ZnO concentration. (respectively referred to ◆ 1h and ■ 72h of exposure)

Conclusion

The characterization of intrinsic and system-dependent properties of two types of ZnO NPs (naked and coated), selected as target materials in the project PATROLS, allowed us to investigate how the presence of coating or of exposure medium, affected hazard and exposure relevant properties such as the hydrodynamic size distribution, zeta potential and static dissolution. What we found is that the coating does not affect colloidal stability, and only slightly prevents dissolution around neutral pH range. In the presence of medium (indifferent ions and specifically adsorbed anions) the ZP reverses its sign and in general decrease with a shift of IEPs at more acid pH. The ZP vs pH curves in water confirm the strong dissolution observed at pH lower than 6, with the likely formation of a new surface for ion re-precipitation. The results are of extreme importance when environmental *in-vivo* or *in-vitro* experiments are carried on, because they provide a real estimation of the amount of material, vs time and speciation, allowing a better estimation of real dose, associated with observed effects.

Acknowledgements

This research received support from the EU H2020 PATROLS (Physiologically Anchored Tools for Realistic nanOmateriaL hazard aSsessment) n° 760813 Project (NMBP-2016-2017).

References

1. Becheri, A., Dürr, M., Lo Nostro, P. & Baglioni, P. Synthesis and characterization of zinc oxide nanoparticles: application to textiles as UV-absorbers. *J. Nanoparticle Res.* **10**, 679–689 (2008).

2. Espitia, P. J. P. *et al.* Zinc Oxide Nanoparticles: Synthesis, Antimicrobial Activity and Food Packaging Applications. *Food Bioprocess Technol.* **5**, 1447–1464 (2012).

3. Sabir, S., Arshad, M. & Chaudhari, S. K. Zinc oxide nanoparticles for revolutionizing agriculture: Synthesis and applications. *Sci. World J.* **2014**, (2014).

4. Kuo, C.-L. *et al.* Synthesis of zinc oxide nanocrystalline powders for cosmetic applications. *Ceram. Int.* **36**, 693–698 (2010).

5. Mirzaei, H. & Darroudi, M. Zinc oxide nanoparticles: Biological synthesis and biomedical applications. *Ceram. Int.* **43**, 907–914 (2017).

6. Hao, L., Chen, L., Hao, J. & Zhong, N. Bioaccumulation and sub-acute toxicity of zinc oxide nanoparticles in juvenile carp (Cyprinus carpio): A comparative study with its bulk counterparts. *Ecotoxicol. Environ. Saf.* **91**, 52–60 (2013).

7. Xiao, Y., Vijver, M. G., Chen, G. & Peijnenburg, W. J. G. M. Toxicity and accumulation of Cu and ZnO nanoparticles in daphnia magna. *Environ. Sci. Technol.* **49**, 4657–4664 (2015).

8. Lin, W. *et al.* Toxicity of nano- and micro-sized ZnO particles in human lung epithelial cells. *J. Nanoparticle Res.* **11**, 25–39 (2009).

9. Akhtar, M. J. *et al.* Zinc oxide nanoparticles selectively induce apoptosis in human cancer cells through reactive oxygen species. *Int. J. Nanomedicine* **7**, 845–857 (2012).

10. Sharma, V., Anderson, D. & Dhawan, A. Zinc oxide nanoparticles induce oxidative DNA damage and ROS-triggered mitochondria mediated apoptosis in human liver cells (HepG2). *Apoptosis* **17**, 852–870 (2012).

11. Singh, C. *et al. NM-Series of Representative Manufactured Nanomaterials Characterisation and Test Item Preparation*. (2011). doi:10.2787/55008

12. Booth, A. & Alstrup Jensen, K. SOP for probe sonicator calibration of delivered acoustic power and de-agglomeration efficiency for ecotoxicological testing. *NANoREG* (2015).

13. Jensen, K. A. The NANOGENOTOX dispersion protocol for NANoREG. *Nrcwe* (2014).

14. OECD. Test No. 308: Aerobic and Anaerobic Transformation in Aquatic Sediment System. *OECD Guidel. Test. Chem.* 19 (2002). doi:10.1787/9789264070523-en

15. ECHA. Appendix R . 6-1 : Recommendations for nanomaterials applicable to the Guidance on QSARs and Grouping. 29 (2017). doi:10.2823/884050

16. Mitrano, D. M., Motellier, S., Clavaguera, S. & Nowack, B. Review of nanomaterial aging and transformations through the life cycle of nano-enhanced products. *Environ. Int.* **77**, 132–147 (2015).

17. OECD. ENV/JM/MONO(2016)2 JOINT MEETING OF THE CHEMICALS COMMITTEE AND THE WORKING PARTY ON CHEMICALS, PESTICIDES AND BIOTECHNOLOGY PHYSICAL-CHEMICAL PARAMETERS: MEASUREMENTS AND METHODS RELEVANT FOR THE REGULATION OF NANOMATERIALS OECD Workshop Report Series on. 36 (2016).

18. Häder, D.-P. & Erzinger, G. S. OECD Guidelines for tetsing of chemicals. 1–21 (1998). doi:10.1016/B978-0-12-811861-0.00011-5

19. Samel, A., Ziegenfuss, M., Goulden, C. E., Banks, S. & Baer, K. N. Culturing and Bioassay Testing ofDaphnia magnaUsing Elendt M4, Elendt M7, and COMBO Media. *Ecotoxicol. Environ. Saf.* **43**, 103–110 (1999).

20. Kallay, N., Kovačević, D. & Žalac, S. Thermodynamics of the solid/liquid interface - its application to adsorption and colloid stability. *Interface Sci. Technol.* **11**, 133–170 (2006).

21. Fatehah, M. O., Aziz, H. A. & Stoll, S. Stability of ZnO Nanoparticles in Solution. Influence of pH, Dissolution, Aggregation and Disaggregation Effects. *J. Colloid Sci. Biotechnol.* **3**, 75–84 (2014).

22. Degen, A. & Kosec, M. Effect of pH and impurities on the surface charge of zinc oxide in aqueous solution. *J. Eur. Ceram. Soc.* **20**, 667–673 (2000).

23. Dahirel, V. & Jardat, M. Effective interactions between charged nanoparticles in water: What is left from the DLVO theory? *Curr. Opin. Colloid Interface Sci.* **15**, 2–7 (2010).

24. Arts, J. H. E. *et al.* A decision-making framework for the grouping and testing of nanomaterials (DF4nanoGrouping). *Regul. Toxicol. Pharmacol.* **71**, S1–S27 (2015).

4.2 Titanium dioxide and Cerium dioxide in aquatic media

Introduction

Environmental safety is one of the serious issues for the scientific community with particular interest in the rapid increase of organic pollutants use / production in agriculture and industries, that can affect both the air than the water compartment. In different case the use of NPs in the treatment of organic pollutants can provide efficient methods for the improvement of new or more efficient water depollution industrial processes[1–3]. In this context two of the most popular NMs investigated for their (photo) catalytic properties are titanium dioxide (TiO_2 NPs) and cerium dioxide (CeO_2 NPs) nanoparticles[4].

Specially, CeO_2 NPs were proposed as a redox mediator and used in electro-analytical techniques and photo-catalyst applications for the degradation of organic compounds. CeO_2 NPs present a good electrochemical activity and are thus applied in various fields such as catalysis, fuel cells and sensors[1,5,6]. As well, TiO_2 NPs is one of the most used materials for photo-electro-catalytic degradation of pollutants, due to its high oxidation efficiency, high photostability and chemical inertness[7–9]. The photocatalytic activity of micro- and nano- TiO_2 has been utilized to improve the degradation efficiencies of various contaminants in both water treatment and air pollution control[10,11]. Therefore, CeO_2 NPs and TiO_2 NPs play a vital role in emerging technologies for environmental applications, such as remediation. The choice was due to the high probability of these two NPs to came in contact with the two compartments, fresh water and sea water. TiO_2 is mainly applied in materials production – as paints, printing ink, plastics, paper, synthetic fibers, rubber, condensers, ceramics and electronic components – in catalysis and photo-catalysis, as antibacterial agents and in food and cosmetics, as sunscreen[2,9,10,12,13]. Thus, TiO_2 NPs could probably get in touch with both fresh and sea water compartments. While CeO_2 is mainly exploited for its interesting redox activity in catalytic applications, such as in catalytic converter or in chemi-sensor[1,5,6,14,15], thus is more probably to have effects on fresh water compartments.

In face of these promising properties and increase use in everyday applications, research community has to take care about any potential risk for human and environment, along all the life-cycle of these NMs, not only in-the use stage but also during production (main release into air) and end of life (many release in waste water). The present attempts to classify (grouping) NMs, put both CeO_2 and TiO_2 NPs in the group of highest concern, classifying them as persistent and reactive materials (group MG4 of the DF4nanoGrouping classification framework[16,17] – Figure 2.1). Addressing environmental safety, we focused on properties that affect the colloidal stability

and so the potential translocation of NPs in liquid environmental compartments. In particular, we optimized a set-up for measuring the concentration at half height of a water column model, to support the estimation of particles that can reach biological target and determine an adverse effect (dose). The ionic component was not considered, because CeO_2 and TiO_2 NPs are practically insoluble [18,19], so we evaluated morphology, the hydrodynamic size in fresh and marine water, Zeta potential variation vs pH.

Experimental part

Materials. Titanium dioxide, JRCNM01005a / NM-105[12], and Cerium dioxide, NM-212[15], were provide as nano-powders by JRC in Ispra (Italy)[20] and analyzed within the framework of European Project PATROLS (N°. 760813). Nitric acid (65%), sulfuric acid (96%), phosphoric acid (85%) and ICP-OES standards were purchased from Sigma-Aldrich (Italy). All the Elendt M7 medium salts were purchased from Sigma-Aldrich (Italy) as well; their approximate composition in mg L^{-1} is 0.715 H_3BO_3, 0.090 $MnCl_2*4H_20$, 0.078 LiCl, 0.018 RbCl, 0.040 SrCl2*$6H_20$, 0.004 NaBr, 0.017 $Na_2MoO_4*2H_2O$, 0.005 $CuCl_2*2H_2O$, 0.015 $ZnCl_2$, 0.012 $CoCl_2*2H_2O$, 0.004 KI, 0.003 Na_2SeO_3, 0.001 NH_4VO_3, 1.250 $Na_2EDTA*2H_20$, 0.498 $FeSO_4*7H20$, 293.800 $CaCl_2*2H_2O$, 123.300 $MgSO_4*7H_20$, 5.800 KCl, 64.800 $NaHCO_3$, 10.000 $Na_2SiO_2*9H_20$, 0.274 $NaNO_3$, 0.143 KH_2PO_4, 0.184 K_2HPO_4. Egg water medium was obtained with dilution of "instant ocean salt" in MilliQ water (60 mg L^{-1})[21], that was purchased from Fisher Scientific (Thermo Fisher Scientific – Canada). The composition of Egg Water presents the follow approximate composition in mg L^{-1}: 18.208 Na^+, 0.630 K^+, 2.167 Mg^{2+}, 0.646 Ca^{2+}, 0.029 Sr^{2+}, 31.665 Cl^-, 1.264 SO_4^{2-}, 0.039 total CO_2, 0.008 total B.

Preparation of suspensions. Following NanoReg dispersion protocol[22,23,24], we prepared 2560 mg L^{-1} stock in MilliQ water. We diluted the stock in Elendt M7 and Egg Water media at the concentration of 100 mg L^{-1}. Then, starting from 100 mg L^{-1} dispersion in medium, we further diluted TiO_2 in Elendt M7 and Egg Water media and CeO_2 in Elendt M7 medium. We exploited a range of concentrations of 0.02 - 10 mg L^{-1} at the aim to mimic real long-term exposure conditions. All the samples are incubated and analyzed in the exposure time range of 1h - 24h in static incubation at 22°C, for Elendt M7 medium, and of 1h - 48h in static incubation at 28°C, for Egg Water medium. All the measurements were triplicate.

Intrinsic properties. Morphological characterization of CeO_2 NPs was performed by TEM instrument (FEI TECNAI F20 microscope operating at 200 keV, equipped with an EDX probe and the STEM accessory). TiO_2 NPs were observed by FE-SEM instrument (Carl Zeiss Sigma NTS Gmbh, Oberkochen, DE), coupled with STEM detector. One drop of the stock suspensions diluted in

MilliQ water (2560 mg L^{-1}) was deposited on a film-coated copper grid and then dried in air. The stock is then diluted to 100 mg L^{-1}, dispersion used to obtain the samples in media.

System-dependent properties. The colloidal behavior was evaluated in MilliQ water, in Elentd M7 medium (CeO_2 and TiO_2) and in Egg water (TiO_2), analyzing the hydrodynamic size distribution by DLS (d_{DLS}) and monitoring Zeta Potential (ZP - ζ-pot_{ELS}) by ELS measurements, using a Zetasizer Nanoseries (Malvern Instruments, Malvern, UK). Each sample was prepared in triplicate. ZP titrations as a function of pH were performed in order to check the pH point where ZP is neutralized (isoelectric point, IEP). The concentration at half height of the water-column was estimated, following the set-up described in Figure 4.2.1. We incubated NPs in water media (15 mL falcon), collecting 3 mL of sample from the center of the water-column (9 mL).

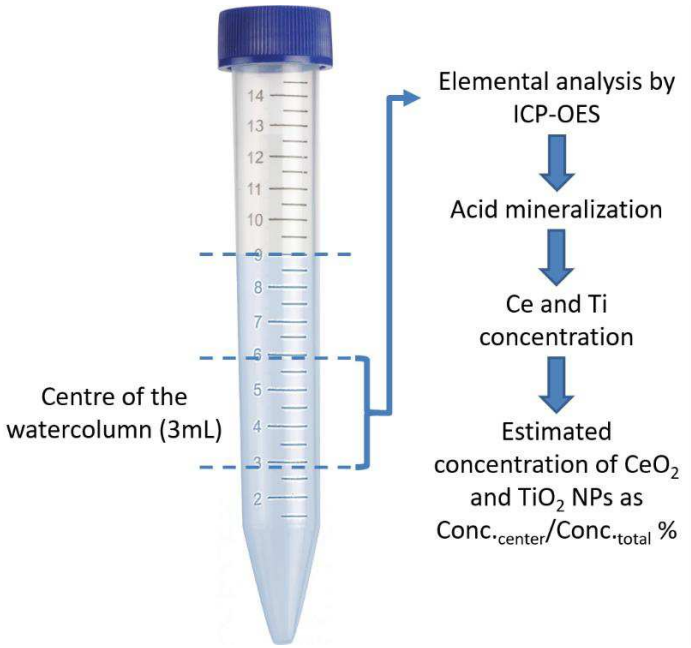

Figure 4.2.1: Experimental set-up for the measurement of the NPs concentration at half height of water column.

The collected 3 mL of sample were then acid digested and analyzed by ICP-OES (ICP-OES 5100 – vertical dual view apparatus, Agilent Technologies, Santa Clara, CA, USA). Acid Digestion procedure was performed adding 0.3 mL of sulfuric acid (H_2SO_4 96%), 0.3 mL of phosphoric acid (H_3PO_4 85%) and 0.3 mL of nitric acid (HNO_3 65%) into 3 mL sample. The resulting samples were ultra-sonicated for 1h in an ultrasonic bath (Bath Temperature = 50°C). The analysis was performed in radial viewing mode, and calibration curves were obtained by diluting a standard of titanium and cerium in Elendt M7 or Egg water (concentrations range 0.1 - 10.0 mg L^{-1}) and reproducing the same matrix of samples by adding acids as in the digestive procedure. Calibration

curve was evaluated and showed correlation coefficient (R^2) above 0.99. Results from ICP-OES were reported as the average of three independent measurements with RSD%.

Results and Discussion

Intrinsic properties

As reported in Figure 4.2.2, TiO_2 NPs show a high tendency to aggregate in the powered state producing micro-aggregates, whilst primary particles show a spherical morphology quite monodispersed, with a size around 20 nm.

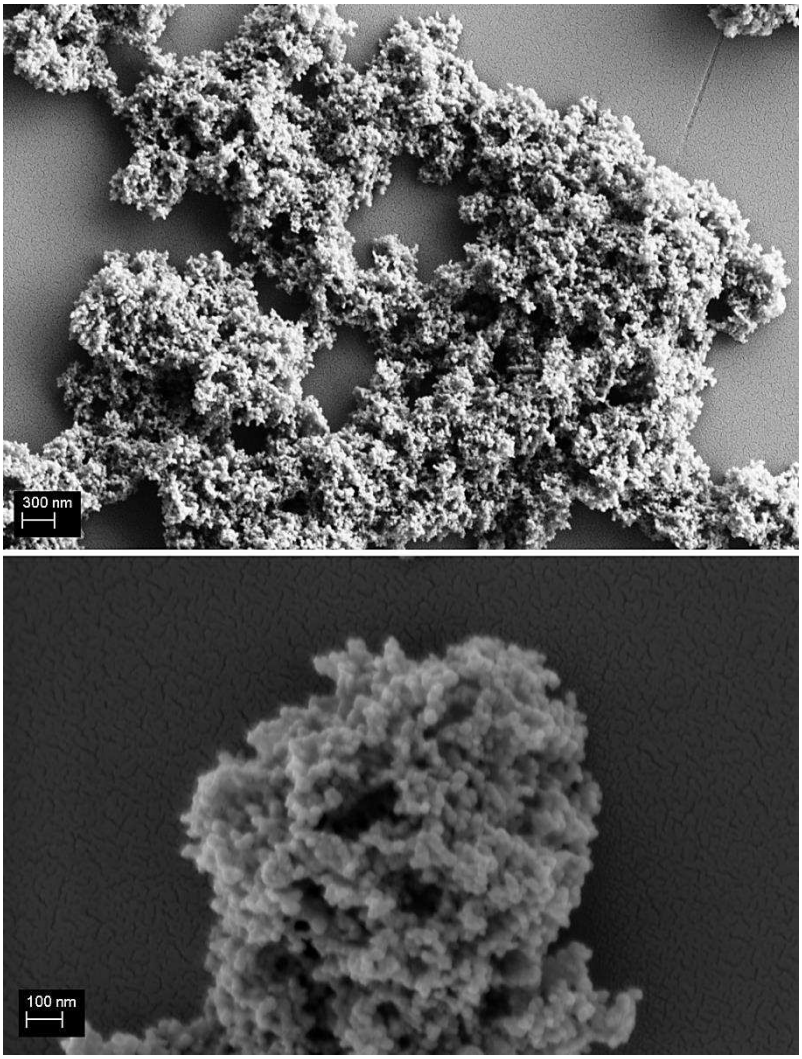

Figure 4.2.2: FE-SEM images of TiO_2 nano-powder.

Different structure is observed for CeO_2, where NPs tend to aggregate, as well, but present a wider size distribution (from ca. 5 nm to 100 nm) with multifaceted shape (Figure 4.2.3). The observed morphologies are coherent with those reported in literature[6,12,15,25].

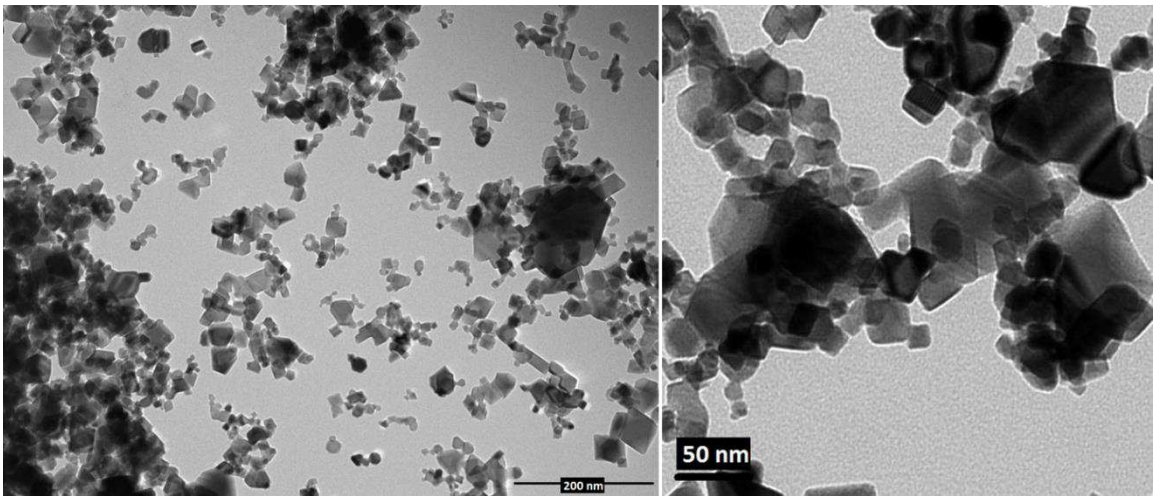

Figure 4.2.3: TEM images of CeO_2 nano-powder.

Hydrodynamic size (d_{DLS}) and ZP of NPs dispersed in water are reported in Table 4.2.1. Both particles show a certain degree of agglomeration, despite to the positive ZP that should guarantee a good electrostatic stabilization, most likely reflecting the presence of not dispersable aggregates in the powder phase.

Table 4.2.1: DLS and ELS measurements for TiO_2 and CeO_2 dispersed in MilliQ water at 256 mgL^{-1}.

Sample name	pH	d_{DLS} (nm) (rds %) *	ζ-pot_{ELS} (mV) (rds %) **
TiO_2	4.5	339 ± 6	34.3 ± 1.8
CeO_2	5.0	211 ± 7	16.8 ± 3.4

** all sample present good reproducibility data, with PDI lower than 0.300.*

System-dependent properties

Starting from intrinsic properties, we proceeded with the characterization of system-dependent properties evaluation, considering fresh and sea water exposure conditions. In particular, we focused on the possible scenario of TiO_2, both in Elendt M7 and Egg water medium, and of CeO_2 in Elendt M7 medium.

TiO_2 in Elendt M7

ZP curve as a function of pH is reported in Figure 4.2.4. TiO_2 NPs present the typical amphiphilic behavior of oxide NPs dispersed in water, positive at acid pH and negative for basic environment, showing, in agreement with literature, the IEP at pH 6.5[12,26,27]. Once dispersed in Elendt M7 medium, TiO_2 NPs show a slight shift of IEP (pH 5.4)[28,29], most likely due to the adsorption of co-exposed anions (SO_4^{2-}, PO_4^{3-}) at the NPs surface. In addition, the ZP values are

flattened and lowered with values between 20 mV and -10 mV, due to the presence of indifferent ions (Cl^-, Br^-, I^-, NO_3^-), that reduce the double layer thickness at the NPs surface.

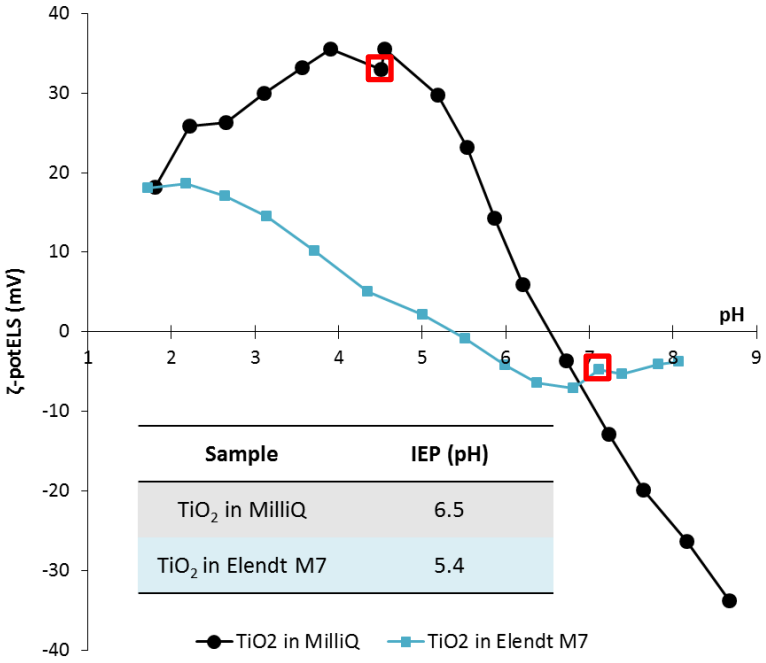

Figure 4.2.4: Zeta Potential (mV) vs pH plot of TiO_2 in MilliQ (●) and in Elendt M7 (■) media (nanosol concentration 100 mg L^{-1} - ☐ natural pH).

The colloidal stability of TiO_2 NPs was further evaluated by measuring the hydrodynamic size (d_{DLS}) and the half water column height concentration of samples dispersed in Elendt M7 medium at low concentration, mimicking exposure conditions of Daphnia magna[28,30,31] (0.02, 0.20, 2.00 and 5.00 mg L^{-1}). As reported in Table 4.2.2, all samples present a strong degree of agglomeration, more evident at low concentrations, the size distribution passing from ca. 800 nm for 5 mg L^{-1} sample to ca. 3000 nm for 0.02 mg L^{-1} sample. No appreciable differences are observable in time and size distribution values remain almost constant from 1h to 24h of exposure. So, the main change occurs in the first hour of exposure. TiO_2 NPs lost the good dispersibility observed in MilliQ stock (Table 4.2.1) and once dispersed in Elendt M7 agglomerated in almost micro-aggregates with high polydispersity (PDI > 0.600).

Table 4.2.2: DLS measurements of TiO_2 in Elendt M7 medium.

Sample concentration (mg L^{-1})	**d_{DLS} distribution (nm) after an exposure time**		
	1h	2h	24h
0.02	2457 ± 832 (PDI: 0.600 ± 0.300)	3268 ± 1230 (PDI: 0.670 ± 0.300)	2495 ± 552 (PDI: 0.720 ± 0.300)

0.2	1701 ± 515 (PDI: 0.740 ± 0.210)	2350 ± 758 (PDI: 0.770 ± 0.250)	2004 ± 633 (PDI: 0.850 ± 0.200)
2.0	906 ± 401 (PDI: 0.700 ± 0.160)	960 ± 597 (PDI: 0.700 ± 0.150)	1267 ± 681 (PDI: 0.760 ± 0.160)
5.0	882 ± 480 (PDI: 0.650 ± 0.190)	628 ± 172 (PDI: 0.590 ± 0.140)	899 ± 237 (PDI: 0.660 ± 0.130)

The presence of salts, even if Elendt M7 is a fresh water medium, can alter the colloidal behavior of the system and decreases the stability of the suspension[32,33]. In Table 4.2.3 and in Figure 4.2.5, we summarized the profile concentration of TiO_2 exposed to Elendt M7 along the water-column, referring to the central part of the water-column (experimental set-up reported in Figure 4.2.1)**.**

Table 4.2.3: Half water column height concentration expressed as TiO_2 Conc. $_{center}$ / Conc. $_{total}$ %, after 1, 24 and 48 hours of exposure in Elendt M7.

	NPs percentage (%)		
Concentration (mg L^{-1})	**% 1h**	**% 24h**	**% 48h**
0.02	75	72	68
0.2	85	75	73
2	89	73	60
5	94	19	8

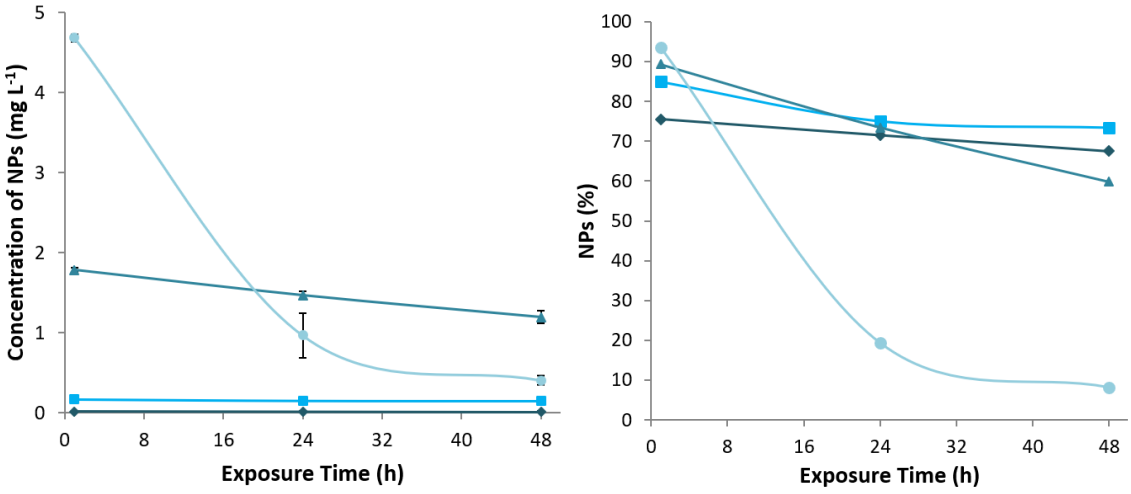

Figure 4.2.5: (left) NPs concentration (mg L^{-1}) and (right) NPs concentration (%) in the central part of water column for (◆) 0.02, (■) 0.2, (▲) 2 and (●) 5 mg L^{-1} samples as a function of time (1, 24 and 48 h).

The results show that in samples more concentrated the progress of agglomeration and precipitation vs time of exposure, occur with higher intensity, most evident for sample at 5mgL^{-1},

where only 10% of initial concentration is found after 48h. Otherwise at low concentration the samples are stable, with only a slightly decrease in concentration after 48h (NPs percentage in the center of ca. 60% / 70%).

TiO_2 in Egg Water

As for Elendt M7, we evaluated the colloidal stability in Egg water medium. In Figure 4.2.6 is reported the ZP vs pH curve measured in Egg water, in comparison with that of Milli Q water. Also in this case, we noticed a slight shift of IEP towards acidic pH, even the natural ZP is higher than that measured in Elendt M7.

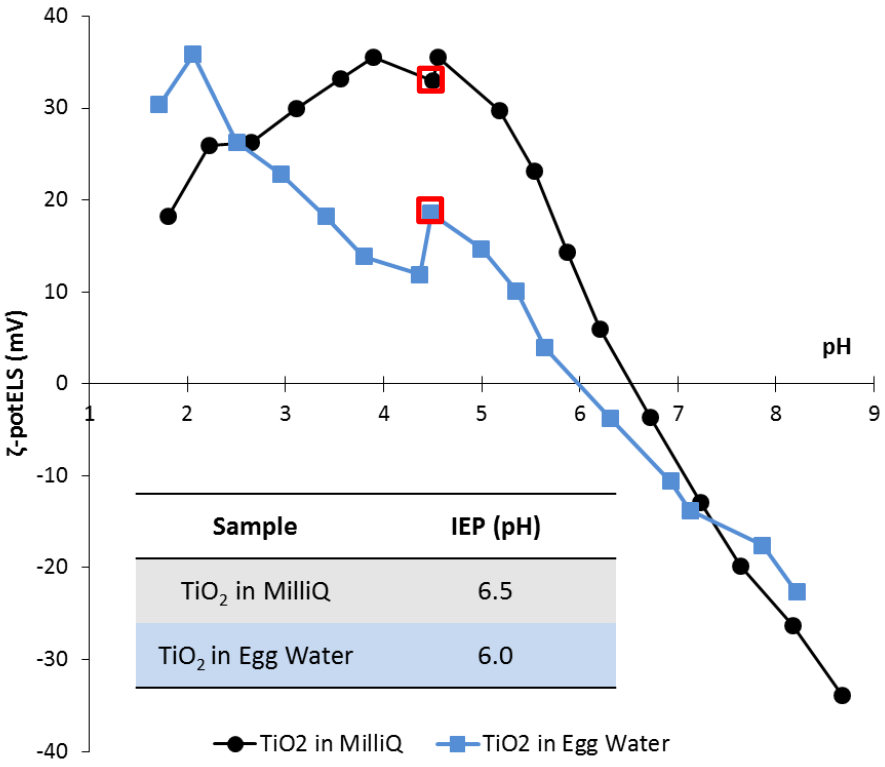

Figure 4.2.6: Zeta Potential (mV) vs pH plot of TiO_2 in MilliQ (●) and in Egg Water (■) media (nanosol concentration 100 mg L^{-1} - ☐ natural pH).

As for Elendt M7, the colloidal stability of TiO_2 NPs was further evaluated by measuring the hydrodynamic size (d_{DLS}) and the half water column height concentration of samples dispersed in Egg water medium at low concentration, mimicking exposure conditions of Zebrafish[31,34,35] (2.0, 5.0 and 10.0 mg L^{-1}). In this case, we selected a higher concentration range to identify the concentration limit, above which the system is strongly affected by the time of exposure. What we found is that at all concentrations, samples present a high instability with a time dependent increase of hydrodynamic diameter from about 800 nm (after 1h) to about 3000 nm (after 24h) for all concentrations tested (Table 4.2.4).

Table 4.2.4: DLS measurements of TiO_2 in Egg Water medium.

Sample concentration (mg L^{-1})	d_{DLS} distribution (nm) after an exposure time		
	1h	2h	24h
2.0	746 ± 299 (PDI: 0.590 ± 0.160)	1171 ± 283 (PDI: 0.410 ±.0.210)	3392 ± 1037 (PDI: 0.960 ± 0.120)
5.0	846 ± 230 (PDI: 0.610 ± 0.170)	1401 ± 221 (PDI: 0.460 ± 0.160)	3275 ± 2378 (PDI: 0.840 ± 0.190)
10.0	750 ± 103 (PDI: 0.520 ± 0.110)	1376 ± 248 (PDI: 0.350 ± 0.190)	3079 ± 1211 (PDI: 0.810 ± 0.230)

In this case, the increase in size distribution is time dependent and doesn't be affected by variation in concentration (from 2 to 10 mg L^{-1}) and the main size dimension changes for all samples from ca. 800 nm after 1h to ca. 3000 nm after 24h of exposure. As in Elendt M7, TiO_2 NPs lost their good dispersibility observed in MilliQ stock (Table 4.2.1) and once dispersed NPs tended to agglomerate in almost micro-aggregates with high polydispersity (PDI ≥ 0.600). These results are confirmed by the profiles of concentration measured at half water column height, where the concentrations drop after 24h (Table 4.2.5 and Figure 4.2.7)

Table 4.2.5: Half water column height concentration expressed as TiO_2 Conc. $_{center}$ / Conc. $_{total}$ %, after 1, 24 and 48 hours of exposure in Egg water.

	NPs in the central column (mg L^{-1}) after:						NPs percentage (%)		
Concentration (mg L^{-1})	**2h**	(rsd)	**4h**	(rsd)	**24h**	(rsd)	**% 2h**	**% 4h**	**% 24h**
2.0	1.79	0.03	1.72	0.04	0.88	0.08	96	92	47
5.0	4.29	0.09	4.23	0.07	1.57	0.17	95	94	35
10.0	8.85	0.09	8.38	0.13	2.66	0.49	99	94	30

Samples in Egg water result stable dispersed in the first 2h, but start to precipitate just after the first four hours of exposure, most likely due to the presence of a higher concentration of salts if compared to the fresh water Elendt M7 medium. After 2h of exposure, the agglomeration and precipitation processes occur and the NPs percentage is drastically reduced in the water-column center, reaching values of ca. 37%. The agglomeration and precipitation phenomena are more evident in the 10 mg L^{-1} sample (30%) and more attenuated in the 2 mg L^{-1} sample (47%), as function of concentration.

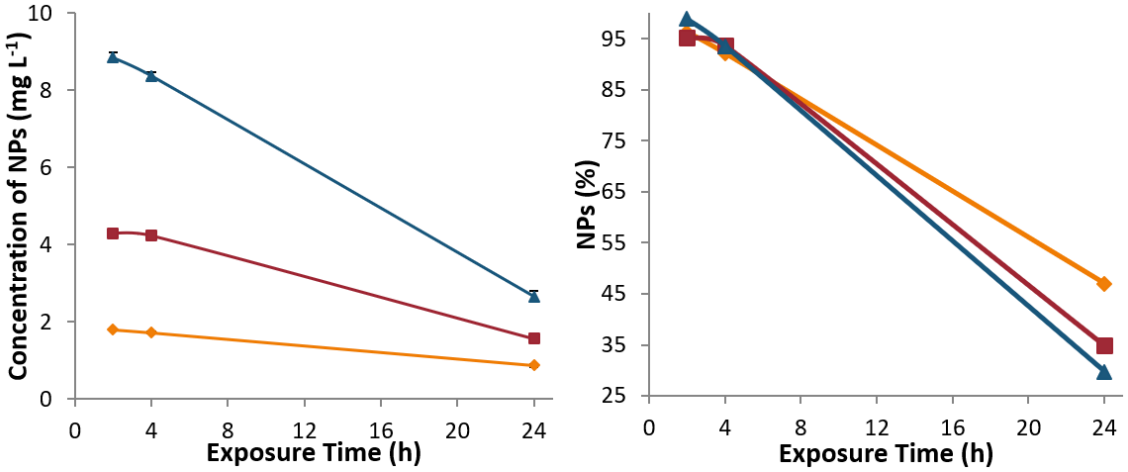

Figure 4.2.7: (left) trend of NPs concentration (mg L^{-1}) and (right) trend of NPs concentration (%) in the central part of watercolumn for (◆) 2, (■) 5 and (▲) 10 mg L^{-1} samples as a function of time (2, 4 and 24 h).

CeO_2 in Elendt M7

As for TiO_2, we evaluated the change in colloidal stability of CeO_2 NPs in MilliQ water and in Elendt M7, to predict their behaviors in environmental medium. The curves of ZP as a function of pH are reported in Figure 4.2.8.

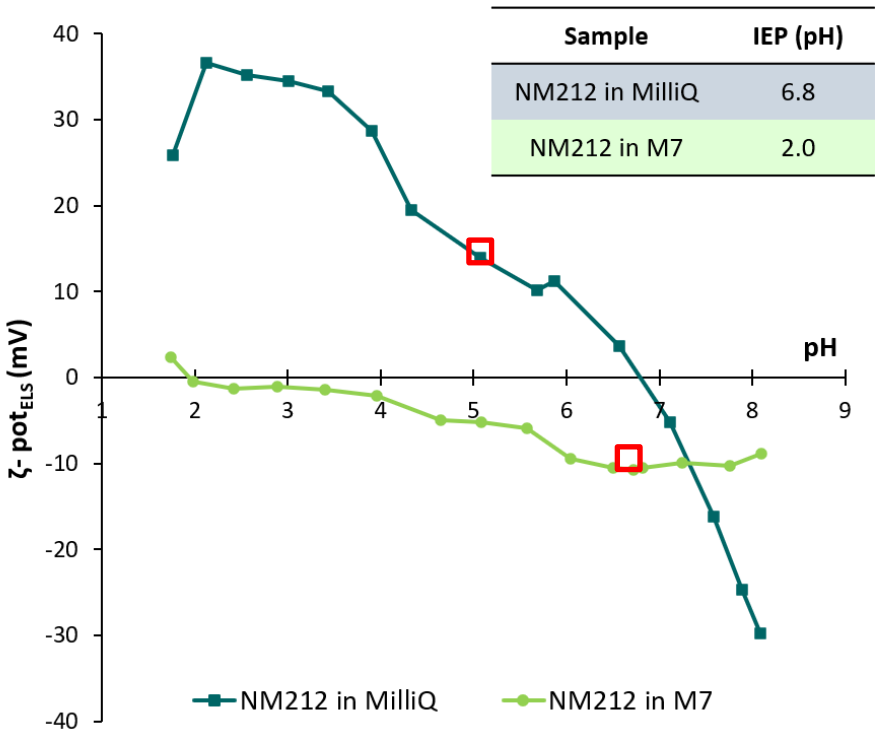

Figure 4.2.8: Zeta Potential (mV) vs pH plot of CeO_2 in MilliQ (■) and in Elendt M7 (●) media (nanosol concentration 100 mg L^{-1} - ☐ natural pH).

In MilliQ water CeO_2 NPs act as TiO_2 NPs, presenting the typical amphiphilic behavior of oxide NPs dispersed in water, positive at acid pH and negative for basic environment, showing, in agreement with literature, the IEP at pH 6.8 [36]. Otherwise, CeO_2 NPs seem strongly affected by the medium, the IEP shifts to pH 2, as the NPs surface was totally covered by co-exposed anions (SO_4^{2-}, PO_4^{3-}). Furthermore, the improved ionic strength of medium, overall decrease the ZP, flattening the curve around values close to 0 mV, promoting the agglomeration confirmed by data of Table 4.2.6.

Also in the case of CeO_2 NPs, to check the colloidal stability, we measured the hydrodynamic d_{DLS} and concentration at half water column height, at the concentration of 0.02, 0.20, 2.00 and 5.00 mg L^{-1} and 1 - 24 h of exposure. Since the first hour we notice the presence of micrometric aggregates that dramatically increase after 24h (Table 4.2.6).

Table 4.2.6: DLS measurements of CeO_2 in Elendt M7 medium.

Sample concentration (mg L^{-1})	**d_{DLS} distribution (nm) after an exposure time**		
	1h	2h	24h
0.2	2778 ± 848 (PDI: 0.570 ± 0.240)	3957 ± 1371 (PDI: 0.630 ± 0.260)	3135 ± 805 (PDI: 0.700 ± 0.260)
2.0	2264 ± 536 (PDI: 0.640 ± 0.260)	2842 ± 902 (PDI: 0.630 ± 0.250)	7401 ± 1099 (PDI: 0.790 ± 0.260)
5.0	1866 ± 412 (PDI: 0.720 ± 0.190)	2343 ± 564 (PDI: 0.400 ± 0.200)	10220 ± 1831 (PDI: 0.910 ± 0.160)

The profile of concentration at half water column height show a trend similar to TiO_2, but as expected more evident, at highest concentration there is an abrupt decrease of NPs detected at half water column height, with time of exposure, as indicating the occurring of sedimentation phenomena (Table 4.2.7 and Figure 4.2.9).

Table 4.2.7: Half water column height concentration expressed as Conc. $_{center}$ / Conc. $_{total}$ %, after 1, 24 and 48 hours of exposure in Elendt M7.

	NPs percentage (%)		
Concentration (mg L^{-1})	**% 1h**	**% 24h**	**% 48h**
0.02	100	100	95
0.2	89	79	59
2	100	50	16
5	93	29	4

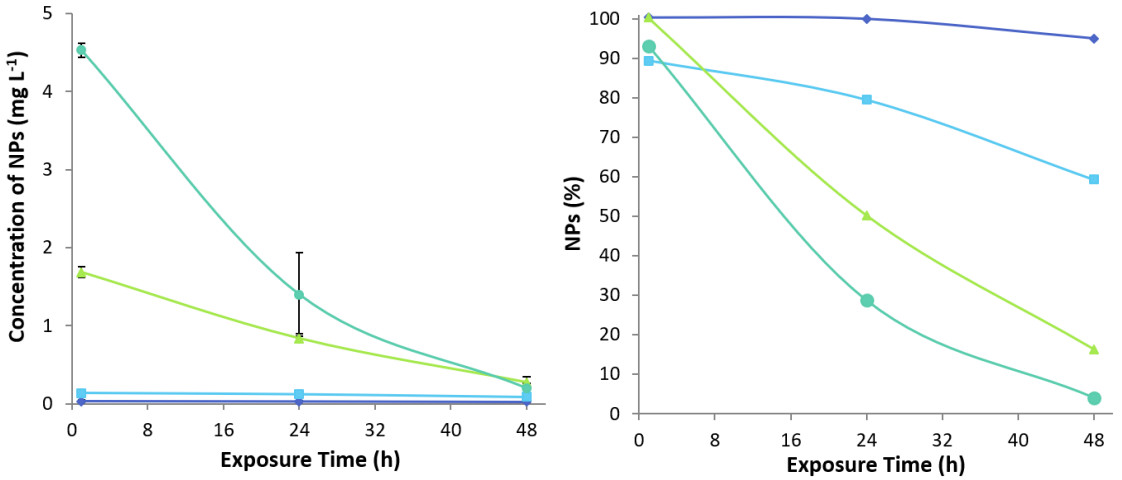

Figure 4.2.9(left) trend of NPs concentration (mg L^{-1}) and (right) trend of NPs concentration (%) in the central part of watercolumn for (◆) 0.02, (■) 0.2, (▲) 2 and (●) 5 mg L^{-1} samples as a function of time (2, 24 and 48 h).

Thus, respect to TiO_2, CeO_2 presents lower limit concentration and therefore tend to precipitate easier. Except for the 0.02 mg L^{-1} sample, that preserves its stability and homogeneous NPs spreading (NPs percentage ≥ 95% in the 1h – 48h exposure range), all the other samples start to precipitate already after the first hour. In 24h the samples present a progressive decrease in NPs concentration, reaching in the case of 5 mg L^{-1} sample some unit percentage (4%) after 48h due to strong precipitation process. Thus, CeO_2 presents a high but progressive tendency to precipitate mostly like driven by concentration and exposure time.

Conclusion

In this study we investigated the colloidal stability of TiO_2 and CeO_2 in fresh and sea water media, mimicking the exposure conditions of *in-vivo* tests performed, respectively, with Daphnia magna and Zebrafish, as part of project PATROLS. Zeta potential titrations as a function of pH allowed us to estimate if transformation on surface acidity occurred (shift of IEP) when NPs are dispersed in environmental media. The hydrodynamic d_{DLS} measured at different concentrations and time of exposure confirmed the high degree of agglomeration of NPs that increases as increases the time of exposure, with exception of TiO_2 in fresh water that seems not affected by the exposure time. A new set-up was optimized and validated with repeated measurements to estimate the concentration of NPs at half water-column height, in order to experimentally evaluate the sedimentation rate as a function of starting concentration and of exposure time. It was found that the sedimentation improves as starting concentration and time of exposure increase. The results are of extreme importance when environmental *in-vivo* or *in-vitro* experiments are carried on, because they provide a real estimation of the amount of material, vs

time and zone of exposure, allowing a better estimation of real dose, associated with observed effects.

Acknowledgements

This research received support from the EU H2020 PATROLS (Physiologically Anchored Tools for Realistic nanOmateriaL hazard aSsessment) n° 760813 Project (NMBP-2016-2017).

References

1. Khan, S. B., Faisal, M., Rahman, M. M. & Jamal, A. Exploration of CeO2 nanoparticles as a chemi-sensor and photo-catalyst for environmental applications. *Sci. Total Environ.* **409**, 2987–2992 (2011).

2. Beeldens, A. An environmental friendly solution for air purification and self-cleaning effect: the application of TIO2 as photocatalyst in concrete. *Proc. Transp. Res. Arena Eur. …* (2006).

3. Daghrir, R., Drogui, P. & Robert, D. Modified TiO2 for environmental photocatalytic applications: A review. *Ind. Eng. Chem. Res.* **52**, 3581–3599 (2013).

4. Ghasemzadeh, G. *et al.* Applications of nanomaterials in water treatment and environmental remediation. *Front. Environ. Sci. Eng.* **8**, 471–482 (2014).

5. Trovarelli, A. Catalytic properties of ceria and CeO2-Containing materials. *Catal. Rev. - Sci. Eng.* **38**, 439–520 (1996).

6. Magudieshwaran, R. *et al.* Green and chemical synthesized CeO2 nanoparticles for photocatalytic indoor air pollutant degradation. *Mater. Lett.* **239**, 40–44 (2019).

7. Kwon, S., Fan, M., Cooper, A. T. & Yang, H. *Photocatalytic applications of micro- and nano-TiO2 in environmental engineering*. *Critical Reviews in Environmental Science and Technology* **38**, (2008).

8. Zhang, Y. *et al.* Photoelectrocatalytic degradation of recalcitrant organic pollutants using TiO2 film electrodes: An overview. *Chemosphere* **88**, 145–154 (2012).

9. Costa, A. L. *et al.* TiO2 based photocatalytic coatings: From nanostructure to functional properties. *Chem. Eng. J.* **225**, 880–886 (2013).

10. Ortelli, S. *et al.* TiO2 based nano-photocatalysis immobilized on cellulose substrates. *J. Photochem. Photobiol. A Chem.* **276**, 58–64 (2014).

11. Ortelli, S. *et al.* Multiple approach to test nano TiO2 photo-activity. *J. Photochem. Photobiol. A Chem.* **292**, 26–33 (2014).

12. Rasmussen, K. *et al. Titanium Dioxide, NM-100, NM-101, NM-102, NM-103, NM-104, NM-105: Characterisation and Physico- Chemical Properties*. (2014). doi:10.2788/79554

13. Haider, A. J., Jameel, Z. N. & Al-Hussaini, I. H. M. Review on: Titanium Dioxide Applications. *Energy Procedia* **157**, 17–29 (2019).

14. Montini, T., Melchionna, M., Monai, M. & Fornasiero, P. Fundamentals and Catalytic Applications

of CeO2-Based Materials. *Chem. Rev.* **116**, 5987–6041 (2016).

15. Singh, C. & Europäische Kommission Gemeinsame Forschungsstelle Institute for Health and Consumer Protection. *Cerium Dioxide NM-211, NM-212, NM-213, characterisation and test item preparation JRC repository: NM-series of representative manufactured nanomaterials*. (2014). doi:10.2788/80203

16. Arts, J. H. E. *et al.* Case studies putting the decision-making framework for the grouping and testing of nanomaterials (DF4nanoGrouping) into practice. *Regul. Toxicol. Pharmacol.* **76**, 234–261 (2016).

17. Arts, J. H. E. *et al.* A decision-making framework for the grouping and testing of nanomaterials (DF4nanoGrouping). *Regul. Toxicol. Pharmacol.* **71**, S1–S27 (2015).

18. Kocbek, P., Teskač, K., Kreft, M. E. & Kristl, J. Toxicological Aspects of Long-Term Treatment of Keratinocytes with ZnO and TiO2 Nanoparticles. *Small* **6**, 1908–1917 (2010).

19. Cornelis, G. *et al.* Solubility and batch retention of CeO2 nanoparticles in soils. *Environ. Sci. Technol.* **45**, 2777–2782 (2011).

20. Singh, C. *et al. NM-Series of Representative Manufactured Nanomaterials Characterisation and Test Item Preparation*. (2011). doi:10.2787/55008

21. Wen, J. & Hu, C. Elemental composition of commercial sea cucumbers (holothurians). *Food Addit. Contam. Part B Surveill.* **3**, 246–252 (2010).

22. Booth, A. & Alstrup Jensen, K. SOP for probe sonicator calibration of delivered acoustic power and de-agglomeration efficiency for ecotoxicological testing. *NANoREG* (2015).

23. Jensen, K. A. The NANOGENOTOX dispersion protocol for NANoREG. *Nrcwe* (2014).

24. OECD. Test No. 308: Aerobic and Anaerobic Transformation in Aquatic Sediment System. *OECD Guidel. Test. Chem.* 19 (2002). doi:10.1787/9789264070523-en

25. Evonik Industries. Technical Information 1243: AEROXIDE, AERODISP and AEROPERL - Titanium dioxide as photocatalyst. (2015).

26. Lolli, A. *et al.* Innovative synthesis of nanostructured composite materials by a spray-freeze drying process: Efficient catalysts and photocatalysts preparation. *Catal. Today* **334**, 193–202 (2019).

27. Holmberg, J. P., Ahlberg, E., Bergenholtz, J., Hassellöv, M. & Abbas, Z. Surface charge and interfacial potential of titanium dioxide nanoparticles: Experimental and theoretical investigations. *J. Colloid Interface Sci.* **407**, 168–176 (2013).

28. Häder, D.-P. & Erzinger, G. S. OECD Guidelines for tetsing of chemicals - Daphnia magna Reproduction Test. *OECD* 1–21 (1998). doi:10.1016/B978-0-12-811861-0.00011-5

29. Samel, A., Ziegenfuss, M., Goulden, C. E., Banks, S. & Baer, K. N. Culturing and Bioassay Testing ofDaphnia magnaUsing Elendt M4, Elendt M7, and COMBO Media. *Ecotoxicol. Environ. Saf.* **43**, 103–110 (1999).

30. Xiao, Y., Vijver, M. G., Chen, G. & Peijnenburg, W. J. G. M. Toxicity and accumulation of Cu and ZnO nanoparticles in daphnia magna. *Environ. Sci. Technol.* **49**, 4657–4664 (2015).

31. Jang, G. H., Park, C.-B., Kang, B. J., Kim, Y. J. & Lee, K. H. Sequential assessment via daphnia and zebrafish for systematic toxicity screening of heterogeneous substances. *Environ. Pollut.* **216**, 292–303 (2016).

32. Tiller, C. L. & O'Melia, C. R. Natural organic matter and colloidal stability: Models and measurements. *Colloids Surfaces A Physicochem. Eng. Asp.* **73**, 89–102 (1993).

33. French, R. A. *et al.* Influence of ionic strength, pH, and cation valence on aggregation kinetics of titanium dioxide nanoparticles. *Environ. Sci. Technol.* **43**, 1354–1359 (2009).

34. Lin, S., Lin, S., Zhao, Y. & Nel, A. E. Zebrafish: An in vivo model for nano EHS studies. *Small* **9**, 1608–1618 (2013).

35. Hua, J., Vijver, M. G., Richardson, M. K., Ahmad, F. & Peijnenburg, W. J. G. M. Particle-specific toxic effects of differently shaped zinc oxide nanoparticles to zebrafish embryos (Danio rerio). *Environ. Toxicol. Chem.* **33**, 2859–2868 (2014).

36. Berg, J. M., Romoser, A., Banerjee, N., Zebda, R. & Sayes, C. M. The relationship between pH and zeta potential of ∼ 30 nm metal oxide nanoparticle suspensions relevant to in vitro toxicological evaluations. *Nanotoxicology* **3**, 276–283 (2009).

5. Conclusions

The risk management decision process needs information on health impact, such as the benchmark (limit) doses that do not cause adverse effects, nevertheless is necessary to refer such information to specific exposed population such as workers / user or biota. The goal of this Ph.D. thesis, was that to support NMs risk assessment, focusing on the characterization and control of physicochemical properties and behaviors, causing potentially hazardous mechanisms against human and environment. Five case studies dealing with both human and environmental exposure scenario were investigated and materials selected to support grouping strategy, respectively soluble MG1 (as ZnO, CuO and Ag NPs), passive MG3 (as SiO_2 NPs) and active MG4 (as TiO_2 and CeO_2 NPs).

The outputs coming from the characterization of intrinsic, system-dependent and *in-vitro* properties aimed to promote the advancement of exposure-dose-response models and provide datasets for the development / validation of *in-silico* models, which represents an appealing alternative to animal testing.

As far as fate in human models are concerned, we believe that data collected will contribute to dosimetry adjustment of dermal and oral mucosa exposure-dose-response studies, in order to derive more relevant reference doses (DNEL, ADI…etc.). In addition, the knowledge of NMs fate across dermal barriers will provide information on human exposure potential and mechanism.

Moreover, fate in environmental model, even less investigated through the thesis, provided physicochemical data that can be used to improve eco-tox dose-response models and derive more accurate reference values (PNEC) for scientific and regulatory purposes.

The main results achieved are summarized in the followings:

Cap. 3.3.1

In this study, we produced two new types of Ir@SiO_2 NPs based textile coatings, displaying very promising self-marking and antibacterial properties. The strong interaction between Ir complexes and silica nanoparticles gives these systems the ability to be easily detected under UV light, both when used as coating for textiles and after release in the environment.

Cap. 3.3.2

At our knowledge, this study provided one of the first-time results on human skin penetration of CuO NPs. Intact epidermis acted as good barrier against both Cu^{2+} ions and CuO NPs dispersion, presenting negligible copper passage through the skin. On the other hand, a higher value of transdermal penetration was observed in damaged skin, where the amount of copper increased in time in the receptor fluid for exposure to both Cu^{2+} ions and CuO NPs.

Cap. 3.3.3

At our knowledge, this work presents one of the first attempts to evaluate Ag NPs permeation and penetration through baby porcine oral mucosa to predict the effect of potential oral absorption of Ag NPs in children. The analysis of the receptor fluid allowed the speciation between Ag NPs and Ag^{+} ions, revealing that only Ag NPs crossed the mucosa, reaching the donor fluid. The Ag NPs reaching the receptor fluid resulted well dispersed, able to release a higher amount of ions if compared to the donor fluid, supporting a Trojan horse mechanism, that can drive potential toxic effects.

Cap. 4.1

The characterization of intrinsic and system-dependent properties of two types of ZnO NPs (naked and coated), selected as target materials in the European research project PATROLS, allowed us to investigate how the presence of coating or of exposure medium, affected hazard and exposure relevant properties such as the hydrodynamic size distribution, zeta potential and static dissolution.

Cap. 4.2

In this study we investigated the colloidal stability of TiO_2 and CeO_2 in fresh and sea water medium, mimicking the exposure conditions of *in-vivo* tests performed, respectively, with Daphnia magna and Zebrafish, as part of European research project PATROLS. Zeta potential titrations as a function of pH allowed us to estimate the surface acidity transformation occurred (shift of IEP) when NPs are dispersed in environmental media. The hydrodynamic diameter measured at different concentrations and time of exposure confirmed the high degree of agglomeration of NPs that increases as increases the time of exposure. A new set-up was optimized and validated with repeated measurements to estimate the concentration of NPs at half water column height, in order to experimentally evaluate the sedimentation rate in a typical *in vivo* model and provide useful information for dosimetry adjustments.

6. Acknowledgements

The research leading to these results has received funding from the Doctoral School in Nanotechnology at University of Trieste, from FRA 2018 projects (linea E) from University of Trieste, and by the European Research Infrastructure NFFA-Europe, funded by the EU's H2020 framework program for research and innovation under grant agreement n. 654360, having benefited from the access provided by Fundacio Institut Catala` de Nanocie`ncia y Nanotecnologia – ICN2 – Barcelona (Spain) and Foundation for Research and Technology Hellas – FORTH - Heraklion (Greece). This work has benefited from the European Project PATROLS "Physiologically Anchored Tools for Realistic nanOmateriaL hazard aSsessment" H2020-NMBP-2016-2017, N°. 760813 and the European Union Seventh Framework Program [FP7/2007–2013] under EC-GA N°. 604305 'SUN'. The materials used as reference materials were provided by JRC of Ispra (Italy).

I would like to thank my supervisor Prof. Francesca Larese Filon and my co-supervisor Doc. Anna Luisa Costa for their energetic support and guide during my PhD, I learned a lot by their love for research. I would like to thank also Prof. Matteo Crosera and Prof. Gianpiero Adami from University of Trieste and Doc. Magda Blosi, Doc. Simona Ortelli, Doc. Carlo Baldisserri, Doc. Felice Simeone and Ms. Lara Faccani for their help in the last three year.

I would like to thank my family for the great support since the begin of this big adventure in science. I would like to thank all the people that I met in these years for science, but that are now more than colleagues: Doc. Cristina Grosu, Doc. Federica Mariani and Doc. Valeria Cotta from the triangle Bologna – Trieste – München, girls we did this Ph.D. challenge. I would like to thank my colleagues and friends from ISTEC: Doc. Linda Bergamini, Doc. Elisabetta Campodoni, Doc. Francesca Carella, Doc. Samuele Dozio, Doc. Magherita Montanari and Doc. Francesca Servadei. Even far away thousands of miles, I would like to my friends oversea Rachel Mann, Elvin Vox, Hannah Lingenhoel (United States), Phoebe Tabada (Philippines), Xiufeng Cao (China) and Jeonghyeon Ahn (South Corea). Last but not least I would like to thank my great friend Doc. Giorgia Console Camprini, you are always the best one, and my boyfriend Doc. Andrea Piazza, thank for your ability to make jokes of my misadventures and stress.

Appendix:

- **Appendix 1. Silica nanoparticles for photo-induced self-marker and antibacterial function**
- **Appendix 2. CuO nanoparticles penetration through intact and damaged human skin**
- **Appendix 3. SP-ICP-MS as powerful tool for evaluation of baby porcine mucosa exposure to silver nanoparticles**

Appendix 1.

Silica nanophases for photo-induced self-marker and antibacterial function

From:

"Methylation of Ir(III)-tetrazolato complexes: an effective route to modulate the emission outputs and to switch to antimicrobial properties". V. Fiorini, I. Zanoni, S. Zacchini, A. L. Costa, A. Hochkoeppler, V. Zanotti, A. M. Ranieri, M. Massi, A. Stefan and S. Stagni, Dalton Transaction, 2017, 46, 12328.[1]

"Encapsulation of cationic iridium(III) tetrazole complexes into a silica matrix: synthesis, characterization and optical properties". I. Zanoni, V. Fiorini, M. Rosado, B. Ballesteros, M. Androulidaki, M. Blosi, S. Ortelli, S. Stagni, M. Dondi and A. L. Costa, New Journal of Chemistry, 2018, 42, 9635-9644.[2]

Figure S1.1: ^{1}H NMR of [F_2IrPTZ-Me]$^{+}$, CD_3CN, 400 MHz.

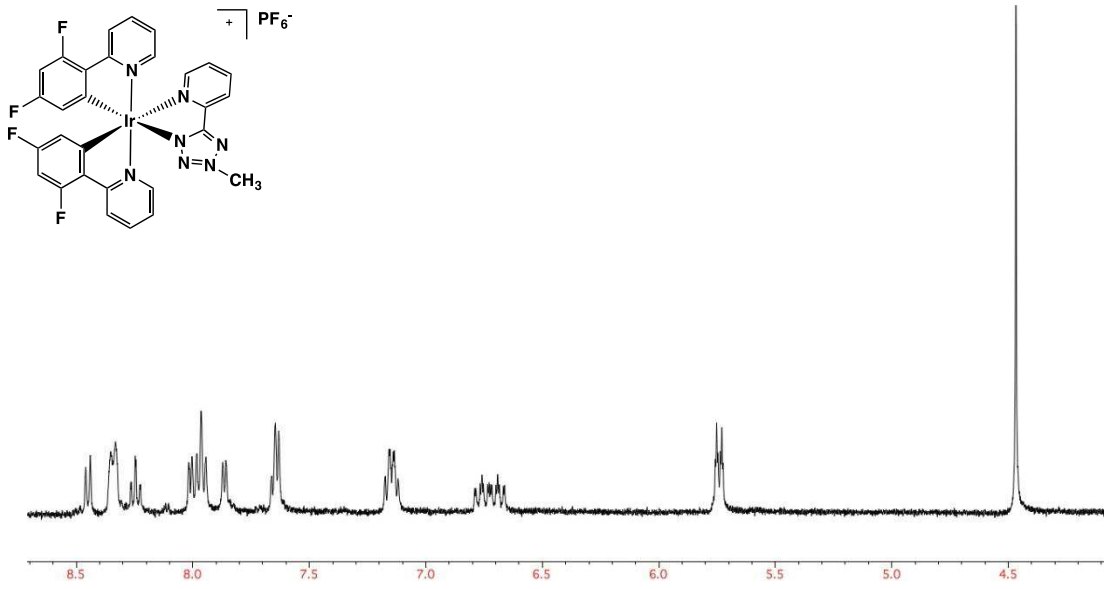

[F_2IrPTZ-Me]$^{+}$ ^{1}H-NMR (CD_3CN, 400 MHz) δ (ppm): 8.46-8.44 (d, 1H, J_{H-H} = 8.00 Hz); 8.36-8.33 (d, 2H, J_{H-H} = 8.80 Hz); 8.26-8.23 (m, 1H); 8.02-7.95 (m, 3H); 7.87-7.86 (d, 1H, J_{H-H} = 5.20 Hz); 7.66-7.63 (m, 2H); 7.17-7.12 (m, 2H); 6.79-6.69 (m, 2H); 5.75-5.73 (m, 2H); 4.47 (s, 3H).

Figure S1.2: ^{1}H NMR of **[IrQTZ-Me]**$^{+}$, CD_3CN, 400 MHz.

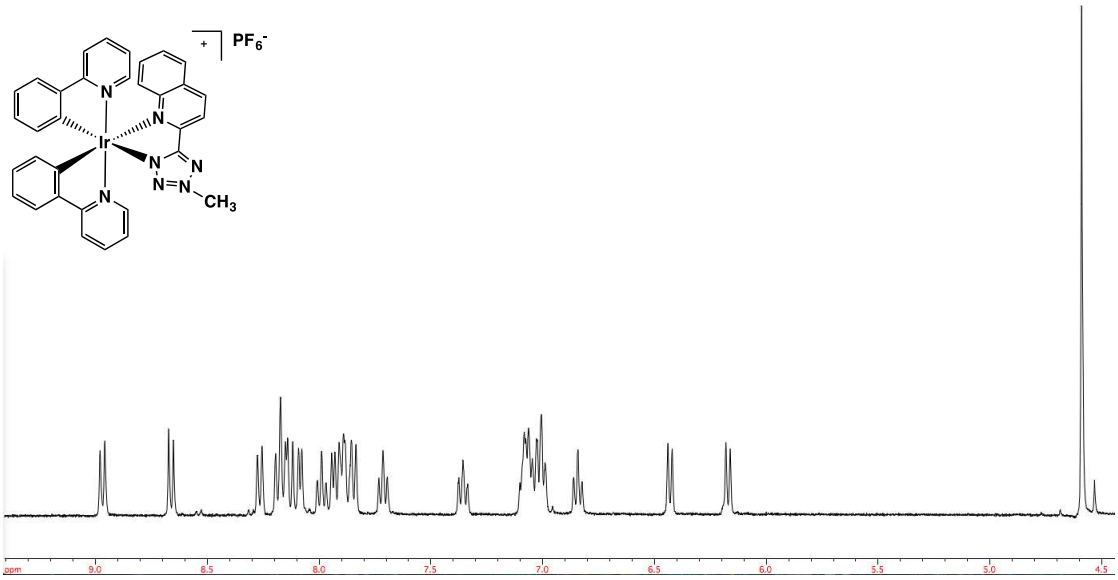

[IrQTZ-Me]$^{+}$ ^{1}H-NMR (Acetone-d^6, 400 MHz) δ (ppm): 8.98 (d, 1H, J_{H-H} = 8.39 Hz), 8.67 (d, 1H, J_{H-H} = 8.39 Hz), 8.27 (d, 1H, J_{H-H} = 7.99 Hz), 8.19 – 8.07 (m, 4H), 8.01 – 7.83 (m, 5H), 7.73 (m, 1H), 7.37 (m, 1H), 7.10 – 6.98 (m, 5H), 6.86 (m, 1H), 6.44 (d, 1H, J_{H-H} = 7.59 Hz), 6.18 (d, 1H, J_{H-H} = 7.59 Hz), 4.59 (s, 3H).

Figure S1.3: ^{13}C NMR of [F_2IrPTZ-Me]$^{+}$, CD_3CN, 400 MHz.

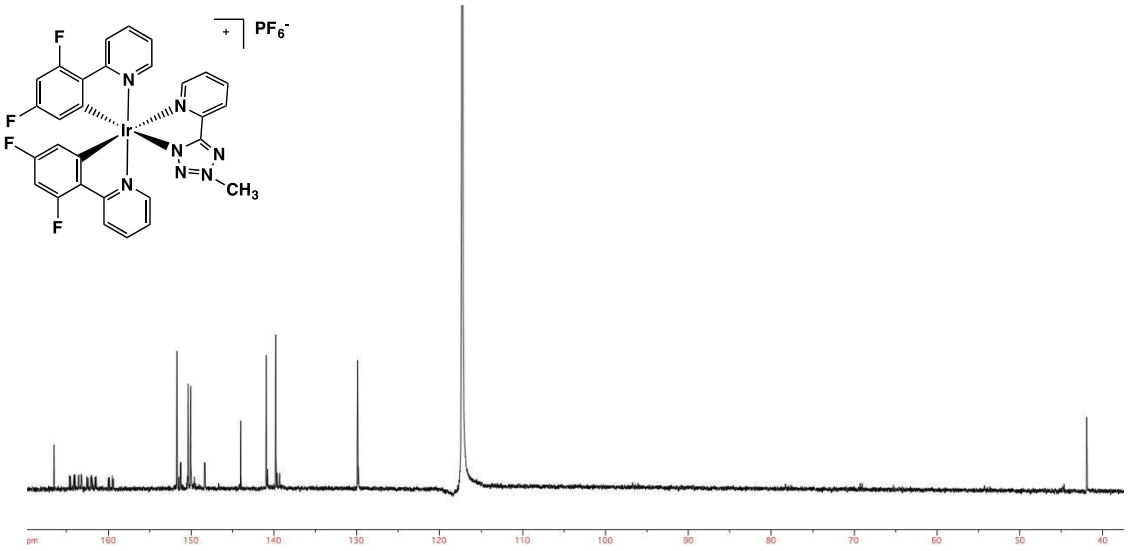

[F_2IrPTZ-Me]$^{+}$ ^{13}C-NMR (CD_3CN, 100 MHz) δ (ppm): 166.54, 164.69, 164.57, 164.13, 164.00, 163.60, 163.53, 163.27, 163.20, 162.59, 162.08, 162.02, 161.95, 161.47, 159.88, 159.50, 151.76, 151.71, 151.47, 151.30, 151.23, 150.43, 150.37, 150.05, 149.97, 149.61, 148.40, 148.32, 144.02, 140.94, 140.80, 140.77, 139.80, 139.62, 139.36, 139.32, 129.93, 129.83, 128.20, 124.84, 124.77, 124.74, 42.08.

Figure S1.4: ^{13}C NMR of **[IrQTZ-Me]$^+$**, CD_3CN, 400 MHz.

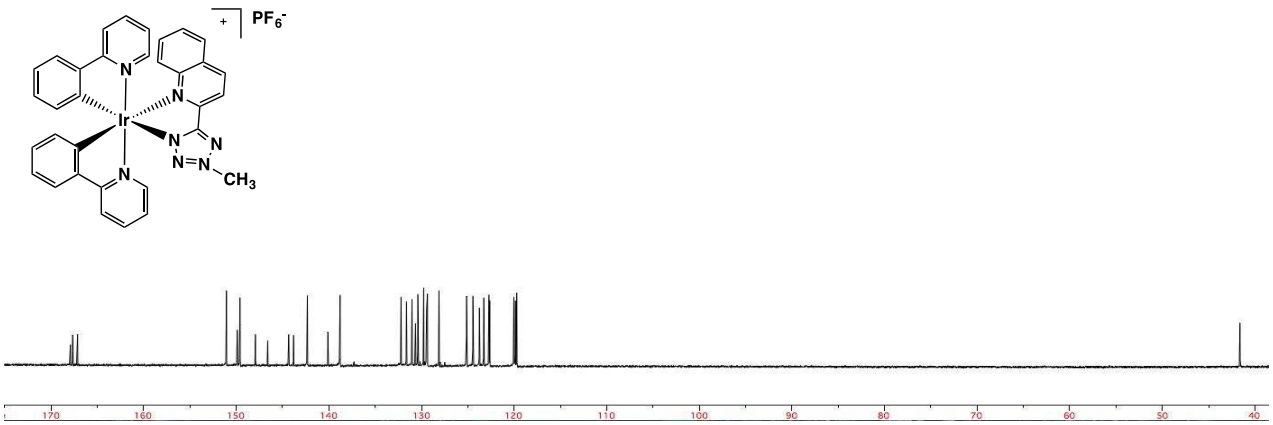

[IrQTZ-Me]$^+$ ^{13}C-NMR (Acetone-d^6, 100 MHz) δ (ppm) = 167.93 (Ct), 167.69, 167.15, 151.08, 149.91, 149.61, 147.95, 146.63, 144.35, 143.83, 142.34, 140.12, 138.84, 138.80, 132.22, 131.63, 131.04, 130.66, 130.40, 129.78, 129.46, 129.37, 128.12, 125.15, 124.46, 123.76, 123.28, 122.73, 122.63, 120.04, 119.87, 119.72, 41.62.

Figure S1.5: ESI-MS spectrum of **[IrQTZ-Me]$^+$** positive ions region) $[M]^+$ = 712 *m/z*, CH_3CN.

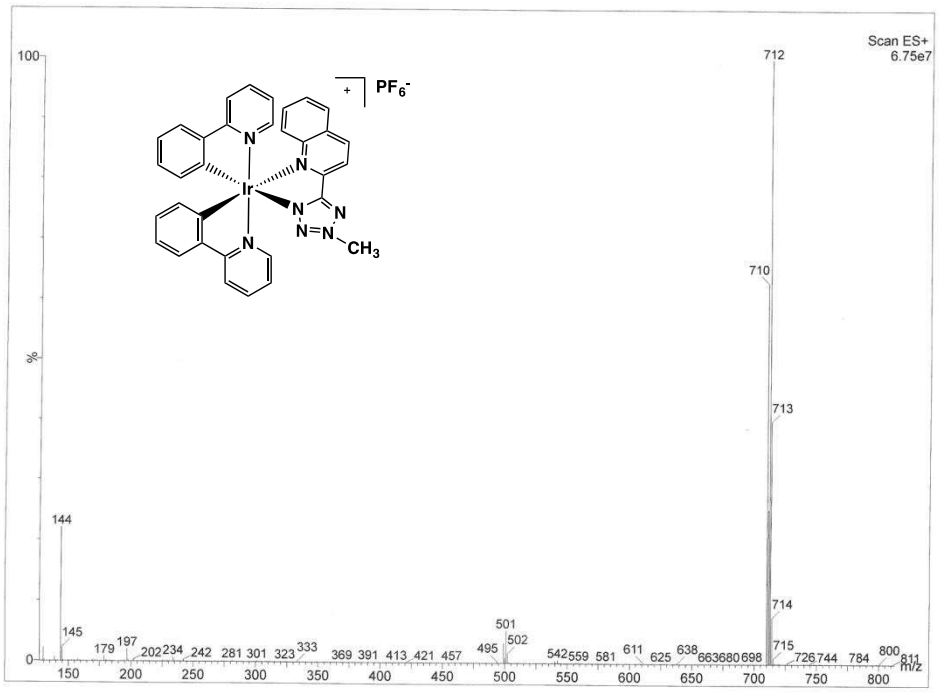

[IrQTZ-Me]$^+$ ESI-MS (*m/z*): $[M^+]$ = 712 m/z $[M^-]$ = 145 m/z (PF_6). Anal. Calcd. For $C_{33}H_{25}F_6IrN_7P$ (856.77) C 46.26, H 2.94, N 11.44. Found: C 40.95, H 2.85, N 9.55.

Figure S1.6: ESI-MS spectrum of **[F_2IrPTZ-Me]$^+$** (positive ions region) $[M]^+$ = 734 *m/z*, CH_3CN.

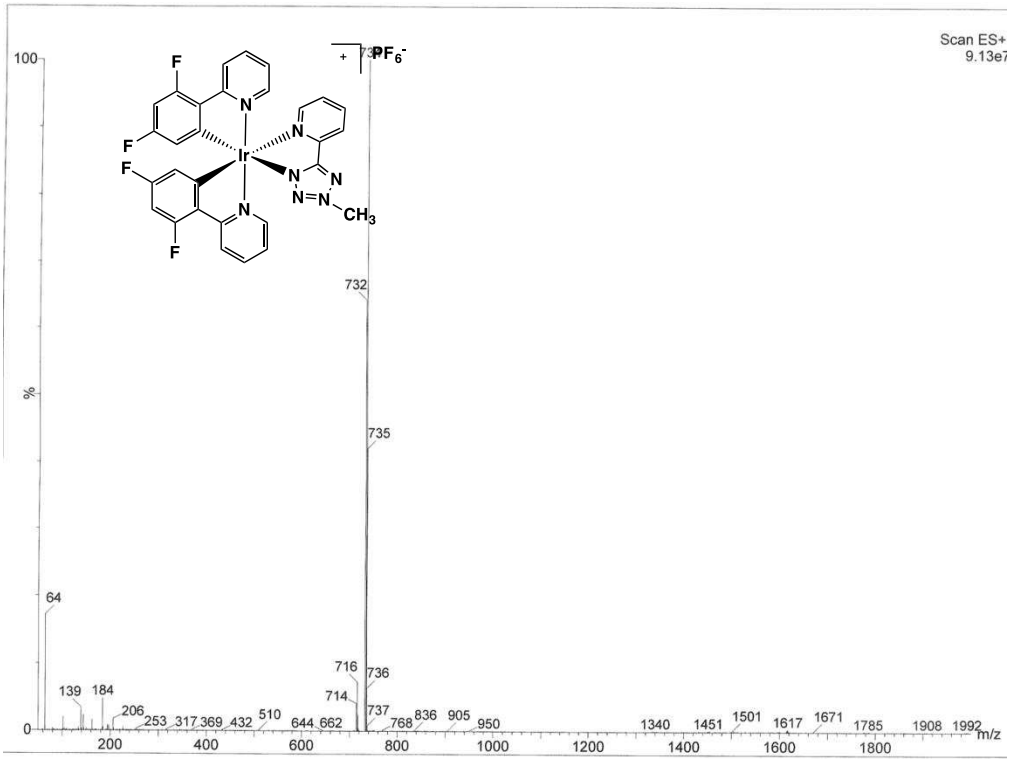

[F_2IrPTZ-Me]$^+$ ESI-MS (*m/z*): $[M]^+$ = 734 m/z $[M]^-$ = 145 m/z (PF_6). Anal. Calcd. For $C_{31}H_{23}Cl_4F_{10}IrN_7P$ (1048.53) C 35.51, H 2.21, N 9.35. Found: C 35.73, H 2.46, N 9.93.

Figure S1.7: Comparison between normalised emission profile of **red Ir@SiO_2** nanosol system (black) and once used as coating on cotton textile (red).

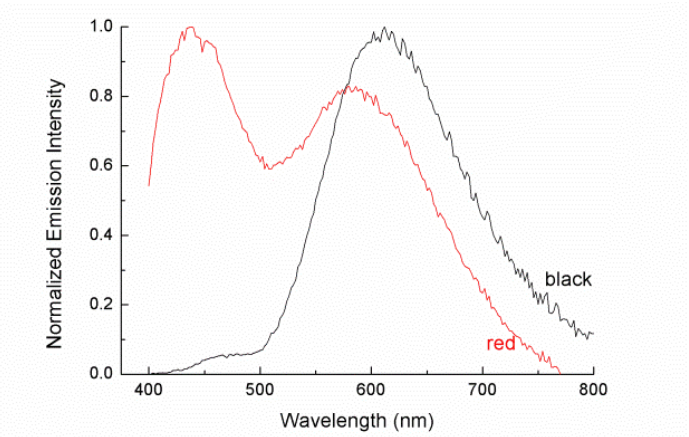

Table S1.1: SiO_2 weight loss% data relative to release test in dynamic condition (test for three layers coated textiles).

		Dynamic release test		
Coating type (3 layers)	**N° washing**	**SiO_2 weight loss%**	**SiO_2 weight total loss%**	**Ir complex weight loss%**
SiO_2	1	0.83 ± 0.12	**1.90 ± 0.45**	/
	2	0.64 ± 0.08		/
	3	0.43 ± 0.03		/
Blue Ir@SiO_2	1	0.76 ± 0.09	**1.97 ± 0.52**	*
	2	0.66 ± 0.07		*
	3	0.55 ± 0.04		*
Red Ir@SiO_2	1	0.74 ± 0.14	**1.65 ± 0.66**	*
	2	0.57 ± 0.47		*
	3	0.46 ± 0.20		*

* values not detectable with ICP-OES analysis (< 0.01 ppm).

Table S1.2: Cumulative SiO_2 weight loss% data relative to release test in static condition for **blue Ir@SiO_2** coating (test for three layers coated textiles).

Contact Time	**SiO_2 weight loss%**	**Ir weight loss%***
1 h	0.14 ± 0.03	-
4 h	0.27 ± 0.07	-
1 d	0.77 ± 0.06	-
3 d	1.19 ± 0.06	-
4 d	1.48 ± 0.02	-
7 d	1.50 ± 0.06	-
10 d	1.52 ± 0.07	-

* values not detectable with ICP-OES analysis (< 0.01 ppm).

Figure S1.8: Image of AATCC 147 tests on red Ir@SiO_2 coated textiles once exposed in dark (I), natural light (II) and natural light + UV (III) conditions.

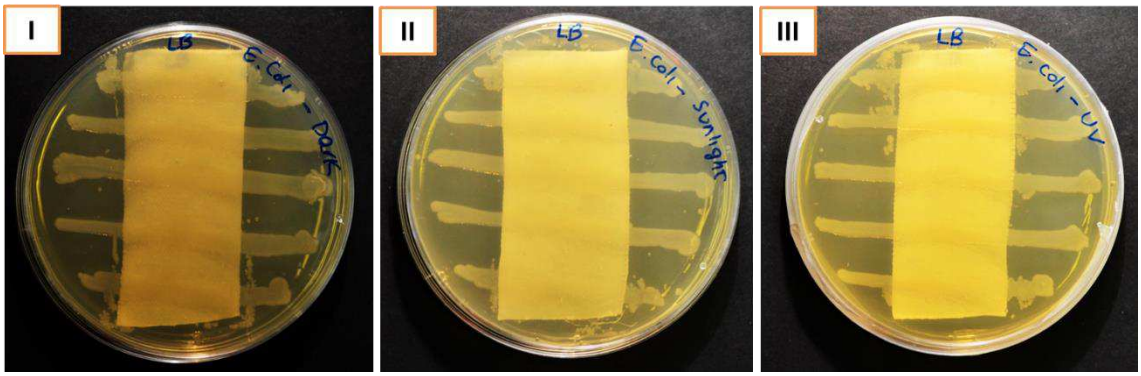

Photophysical characterization. The wavelengths for the emission and excitation spectra were determined using the absorption maxima of the MLCT transition bands (emission spectra) and at the maxima of the emission bands (excitation spectra). Quantum yields (Φ) were determined using the optically dilute method by Crosby and Demas[3] at excitation wavelength obtained from absorption spectra on a wavelength scale [nm] and compared to the reference emitter by the following equation:

$$\phi_s = \phi_r \left[\frac{A_r(\lambda_r)}{A_s(\lambda_s)}\right]\left[\frac{I_r(\lambda_r)}{I_s(\lambda_s)}\right]\left[\frac{n_s^2}{n_r^2}\right]\left[\frac{D_s}{D_r}\right]$$

where A is the absorbance at the excitation wavelength (λ), I is the intensity of the excitation light at the excitation wavelength (λ), n is the refractive index of the solvent, D is the integrated intensity of the luminescence, and Φ is the quantum yield. The subscripts r and s refer to the reference and the sample, respectively. A stock solution with an absorbance > 0.1 was prepared, then two dilutions were obtained with dilution factors of 20 and 10, resulting in absorbance of about 0.02 and 0.08 respectively. The Lambert-Beer law was assumed to remain linear at the concentrations of the solutions. The degassed measurements were obtained after the solutions and bubbled for 10 minutes under Ar atmosphere, using a septa-sealed quartz cell. Air-equilibrated $[Ru(bpy)_3]Cl_2/H_2O$ solution (Φ = 0.028)[4] was used as reference. The quantum yield determinations were performed at identical excitation wavelengths for the sample and the reference, therefore deleting the I(λr)/I(λs) term in the equation. Emission lifetimes (τ) were identified by using the single photon counting technique (TCSPC) with the same Edinburgh FLSP920 spectrometer using pulsed picosecond LED (EPLED 360, FWHM < 800ps) as the excitation source, with repetition rates between 1 kHz and 1 MHz, and the above-mentioned R928P PMT as detector. The goodness of fit was assessed by minimizing the reduced χ2 function

and by visual inspection of the weighted residuals. To record the 77 K luminescence spectra, the samples were put in quartz tubes (2 mm diameter) and inserted in a special quartz Dewar filled with liquid nitrogen. The solvent used in the preparation of the solutions for the photophysical investigations was of spectrometric grade.

References

1. Fiorini, V. *et al.* Methylation of Ir(III)-tetrazolato complexes: an effective route to modulate the emission outputs and to switch to antimicrobial properties. *Dalt. Trans.* **46**, 12328 (2017).

2. Zanoni, I. *et al.* Encapsulation of cationic iridium(III) tetrazole complexes into a silica matrix: synthesis, characterization and optical properties. *New J. Chem.* (2018). doi:10.1039/C8NJ01514G

3. Crosby, G. A. & Demas, J. N. Measurement of photoluminescence quantum yields. Review. *J. Phys. Chem.* **75**, 991–1024 (1971).

4. Nakamaru, K. Synthesis, Luminescence Quantum Yields, and Lifetimes of Trischelated Ruthenium(II) Mixed-ligand Complexes Including 3,3'-Dimethyl-2,2'-bipyridyl. *Bull. Chem. Soc. Jpn.* **55**, 2697–2705 (1982).

Appendix 2.

CuO nanoparticles penetration through intact and damaged human skin

Table S2.1: Hydrodynamic diameters (d_{DLS}) and ζ-potentials (ζ-potELS) of CuO NP dispersed in synthetic sweat (100 mg L^{-1}).

N° batch	*After 1h*			*After 24h*		
	pH	**d_{DLS} (nm)**	**ζ-potELS (mV)**	***pH***	**d_{DLS} (nm)**	**ζ-potELS (mV)**
1	5.8	7385 ± 1619	-7.2 ± 0.6	5.8	8889 ± 1360	-4.4 ± 0.4
2	5.8	3561 ± 1054	-5.5 ± 0.5	5.6	2233 ± 246	-6.3 ±0.2
3	5.7	4567 ± 1209	-7.2 ± 0.2	5.5	3109 ±752	-6.9 ± 0.3

Table S2.2: Measurements of static dissolution ($Cu_{dissolved}/Cu_{total}$ weight ratio %) of CuO NP dispersed in synthetic sweat (100 mg L^{-1}).

N° batch	*After 1h* $Cu_{dissolved}/Cu_{total}$ *weight ratio %*	*After 24h* $Cu_{dissolved}/Cu_{total}$ *weight ratio %*
1	10.9	13.6
2	17.3	21.6
3	20.4	25.6
AVERAGE	**16.2 ± 4.9**	**20.3 ± 6.1**

Table S2.3: Copper skin penetration at 24 h obtained by ICP-OES measurements.

	Epidermis penetration (μg cm^{-2})	**Dermis penetration (μg cm^{-2})**	**Total penetration (μg cm^{-2})**
Intact skin	1.05 ± 0.45	0.40 ± 0.03	1.45 ± 0.42
Damaged skin	2.73 ± 1.90	7.09 ± 5.78	9.82 ± 7.67

Appendix 3.

SP-ICP-MS used as new tool for evaluation of baby porcine mucosa exposure to silver nanoparticles

Figure S3.1: DLS analysis. The curve represents Ag NPs size distribution by intensity. The summary statistics is based upon the intensity of light scattered of 6 different samples derived from nano-silver dispersion.

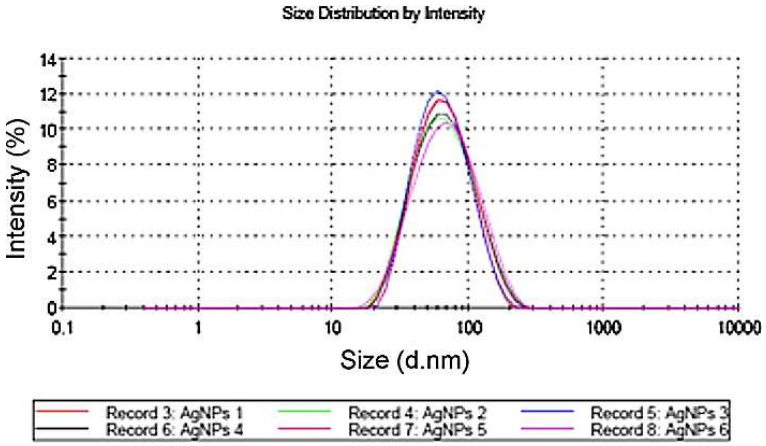

Figure S3.2: Calibration curve for Ag dissolved (u.m.a. 106.905).

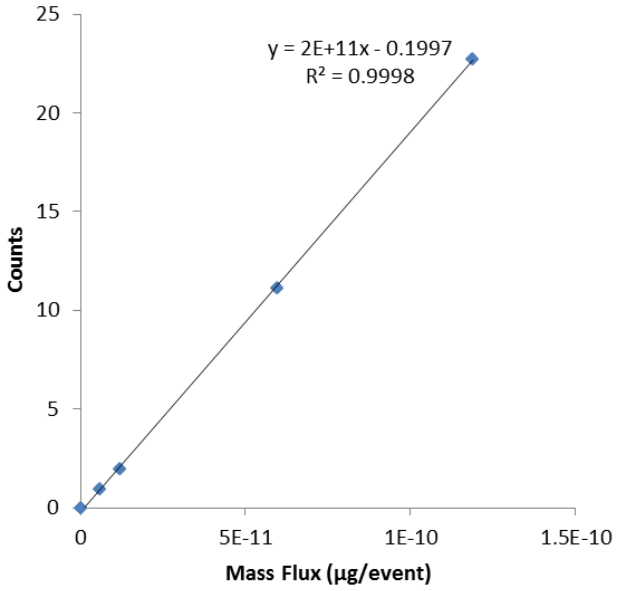

Table S3.1: Product specification of Gold nanoparticles 60 nm citrate coated (Product Number 742015).

Appearance (Form)	Suspension
Polydispersity Index (PDI)	≤ 0.2
Core Size	57 - 63 nm
Mean Hydrodynamic Diameter (d_{DLS})	68 - 76 nm
Concentration (particles number mL^{-1})	1.76 - 2.16 * 10^{10}
Absorption Max	538 - 544 nm
Stabilized suspension	citrate buffer

Figure S3.3: Size distribution of Ag in receptor fluid after 240 min of exposition di Ag ions. Measure within the LOD on instrument. No NPs were detected.